DIRECT NUMERICAL SIMULATION AND ANALYSIS OF SATURATED DEFORMABLE POROUS MEDIA

A Thesis
Presented to
The Academic Faculty

by

Irfan Khan

In Partial Fulfillment
of the Requirements for the Degree
Doctor of Philosophy in the
G.W.Woodruff School of Mechanical Engineering

Georgia Institute of Technology
August 2010

DIRECT NUMERICAL SIMULATION AND ANALYSIS OF SATURATED DEFORMABLE POROUS MEDIA

Approved by:

Professor Cyrus Aidun,
Committee Chair
G.W.Woodruff School of Mechanical Engineering
Georgia Institute of Technology

Professor Cyrus Aidun, Advisor
G.W.Woodruff School of Mechanical Engineering
Georgia Institute of Technology

Professor Ghiassiaan
G.W Woodruff school of Mechanical Engineering
Georgia Institute of Technology

Dr. George Biros
Computational Science and Engineering Division
Georgia Institute of Technology

Professor Suresh Sitaraman
G.W. Woodruff School of Mechanical Engineering
Georgia Institute of Technology

Dr. Thorsten Stoersor
Department of Civil and Environment Engineering
Georgia Institute of Technology

Date Approved: July 5th, 2010

ACKNOWLEDGEMENTS

This accomplishment would not have been possible without the help of so many people, whose support, guidance, feedback and friendship will always be remembered. Firstly, I want to thank Dr. Cyrus K. Aidun for his guidance throughout my Ph.D program. For pushing me to develop the tools and knowledge necessary to carry out independent research work. I also want to thank my committee members for reviewing this work and suggesting new directions in this research.

I want to thank everyone in Dr. Aidun's research group for providing valuable feedback on my research, for commenting on my presentation styles and sharing their knowledge in lattice Boltzmann method. Particularly Jonathan Clausen, whose new ideas on code development and parallelization made the development of such large and complex code possible.

Heartfelt thanks to my parents who have been a source of strength to me. My father who understood my strengths and weaknesses and shared his experiences with me. My mother who always believed in me. Thank you for understanding and doing what is best for me; being there whenever things did not work out and providing me your unconditional support.

Lastly, deepest thanks to my loving wife "Teys". Thank you for listening to me, for reviewing my written work, for staying by my side through some of the most testing times and for all other ways you have helped and motivated me. But most importantly thank you for your boundless love.

TABLE OF CONTENTS

ACKNOWLEDGEMENTS iii

LIST OF TABLES vii

LIST OF FIGURES viii

LIST OF SYMBOLS OR ABBREVIATIONS xiv

SUMMARY xvii

I INTRODUCTION 1

1.1 Deformable Porous Media Models 3

1.1.1 Poroelasticity: Biot's Theory 4

1.1.2 Theory of Porous Media 5

1.1.3 Literature Gap 11

1.1.4 Important parameters 13

II METHODOLOGY 15

2.1 Lattice Boltzmann Method 16

2.2 Finite Element Method 17

2.3 Fluid-Solid Coupling 21

2.4 Contact Modeling 23

2.5 LBM-FEM computations in Parallel 25

2.5.1 Parallelizing LBM 25

2.5.2 Parallelizing FEM 27

2.5.3 Parallelizing coupled LBM-FEM 31

III VALIDATION OF METHOD 35

3.1 Sphere settling in a rectangular channel 35

3.2 Pressure drop across an array of spheres 37

3.3 Cantilever beam deflection 39

3.4 Wave propagation in a beam 41

3.5 Validation of Contact Model 42
3.6 Sample Simulation 43
IV MACROSCOPIC BEHAVIOUR OF MODEL POROUS MEDIA 50
4.1 Behaviour of Simple Cubic Granular Porous Media 50
4.1.1 Permeability of Simple Cubic arrangement 52
4.1.2 Bulk elastic properties of Simple Cubic arrangement 53
4.1.3 Deformation of Simple Cubic Granular Media 55
4.2 Behaviour of Ordered Fibrous Porous Media 61
4.2.1 Permeability of ordered orthogonally crossing fibrous arrangement 62
4.2.2 Bulk elastic properties of ordered orthogonally crossing fibrous arrangement 65
4.2.3 Deformation of Ordered Orthogonally crossing Fibrous Media 68
V MODELING COMPLEX FIBROUS POROUS MEDIA 72
5.1 Wet-Pressing and Felts 72
5.2 Model layered fibrous porous media 79
5.2.1 Literature in permeability of layered fibrous porous media . 80
5.2.2 Permeability study of Model Layered Orthogonal Fibrous media 86
5.2.3 Bulk modulus of model layered orthogonal cylindrical arrangements 90
5.2.4 Developing model geometry for real nonwoven felts 93
5.3 Bulk Modulus (E_b) of Orthogonal Cylindrical Arrangement 97
5.3.1 Homogeneous skewed orthogonal arrangement 98
5.3.2 Non-homogeneous orthogonal arrangement of cylinders . . . 99
5.4 Effect of fiber diameter 101
5.4.1 Homogeneous skewed orthogonal arrangements 103
5.4.2 Nonhomogeneous orthogonal arrangements 105
5.4.3 Behaviour of model nonhomogeneous orthogonal cylindrical structures 108

VI CONSTITUTIVE RELATIONS 110
6.1 Granular Media 111
6.2 Fibrous Media 115
VII CONCLUSIONS AND FUTURE RECOMMENDATIONS 120
7.1 Conclusions 120
7.2 Future Recommendations 124
APPENDIX A PERMEABILITY DEFINITIONS 126
APPENDIX B BULK ELASTIC MODULUS / COMPRESSIBILITY MODULUS 128
REFERENCES 129

LIST OF TABLES

1 Parameters in de Boer et. al. model and their values for the test problem. 10

2 Computational resources that were made use during this research work. 27

3 Values of parameters used for comparing LBM-FEM code with de Boer et al.[25] model, for the case of spheres in SC arrangement. 55

4 Values of parameters used for comparing deformation of cylindrical arrangements with de Boer et al.[25] model 68

5 Comparing Pressing And Drying 73

6 Primary and Secondary variables that influence the process of wet-pressing as given by Busker and Cronin (1984) 76

7 Values of parameters n^S, K^F and E_b for a few skewed orthogonal arrangement of geometries selected. 103

LIST OF FIGURES

1 Response of solid displacement w.r.t time for step loading 10

2 Three dimensional image of a $3 \times 3 \times 3.5$ mm sample of wet-pressing felt. The model geometry of cylinder in orthogonal arrangement. . . . 12

3 Propagation and collision steps in two dimensional lattice Boltzmann scheme. Fluid particles move in discrete velocity directions represented by $\mathbf{e}_i$. 16

4 Approximating a continuous solid domain using finite elements. . . . 18

5 Master tetrahedral element 19

6 Decomposition of a 2D lattice-Boltzmann domain into 4 subdomains for parallel processing. The lattice nodes represented in red are ghost nodes. At each time step distribution from the real nodes of one subdomain are communicated to the ghost nodes of the adjacent subdomain as shown in the the figure. 25

7 Weak scaling results of single phase LBM simulations. 26

8 Mesh partitioning and subsequent PETSc and application ordering of finite element nodes. 28

9 Decomposition of unstructured finite element mesh of a rectangular beam into four subdomains using K-way graph partitioning algorithm provided by PARMETIS 29

10 Strong scaling of the single phase finite element method. Test problem is cantilever beam with 1106730 degrees of freedom. 30

11 Flow chart representation of the algorithm used in the LBM-FEM code to perform coupled calculations in the fluid and solid phases. 32

12 Strong scaling results of the parallel coupled LBM-FEM code. The test problems used for testing speedup are described in chapter 4. . . 34

13 Hindered settling of single solid sphere of radius r in a channel with square cross section of lenght L 36

14 Comparsion of LBM-FEM method with experimental data for hindered settling of spherical particle in a channel with square cross-section. r^* is the effective radius of the sphere, v_w is the hindered settling velocity of the sphere and v_f is the settling velocity in a free stream. 36

15 The geometry used to validate Lattice Boltzmann method to model flow through porous media. The porous media is represented by regular arrangement of spheres. At the inlet (left) a constant velocity U_o is applied and at the outlet (right) stress-free boundary condition is applied. A periodic boundary condition is applied on the rest of the four walls. The pressure drop across the length ΔL is measured. . . . 38

16 Comparison of LBM-FEM method with experimental data for pressure drop in flow through an array of spheres. Ω is friction factor given as $\frac{\Delta P}{\Delta L}\frac{D_p}{\rho {U_0}^2}\frac{\epsilon^3}{(1-\epsilon)}Re$ and Re is Reynolds number given as $\frac{U_0 D_p \rho}{\mu^F(1-\epsilon)}$, where D_p is the diameter of spheres, $\frac{\Delta P}{\Delta L}$ is the pressure drop, U_0 is the average velocity, ϵ is the porosity, ρ and μ^F are the density and viscosity of the fluid respectively. 39

17 Comparison of deflection $\delta(y = 0)$ obtained from a static FE analysis with the analytical deflection given in equation 53. The lines represent the analytical data and the points represent data from FE simulations. The abscissa represents the length along the axis of the cantilever beam. 40

18 Deflection of a Cantilever beam of length l under an applied load P at the beam edge. The color represents the stress variation inside the beam. 40

19 Wave propagation in a rectangular beam. The beam is fixed at the left and is applied a compressive load on the right end. The color represents the stress distribution in the beam 40

20 Comparison of deflection $u(x, t)$ obtained from FE analysis with the analytical deflection given in equation 54. The lines represent the analytical data and the points represent data from FE simulations. The abscissa represents the length along the axis of the cantilever beam. . 41

21 Comparison of the Hertz contact model with the near contact model implemented in LBM-FEM method. α represents the deformation due to the compressive load P and R is the radius of the spheres and cylinders. The solid line represents the analytical model by Hertz and the points represent the LBM-FEM simulation results using coarse mesh ($\times$) and fine mesh ($\boxdot$. 44

22 (a) Model saturated porous media made up of regular arrangement of spheres. Also shown are boundary conditions for the fluid and the loading direction for the solid phase. (b) The configuration of the porous media at steady state. The color represents strain. 45

23 Average normalized displacement w.r.t time. 47

24 Average Pore Pressure w.r.t time ($x = 3R$). 47

25 Two different geometris of two spheres and five spheres used to understand the pressure fluctuations. 48

26 Variation of pressure with time in two geometries. 2 sphere geometry at z=40, 5 sphere geometry at z=120 LBM units. 49

27 10 spheres stacked vertically in a column of fluid, representing a simple cubic arrangement. The dotted line represents the simulation domain. 51

28 Instantaneous compressive bulk modulus E_b as a function of applied load. 54

29 The average displacement of the top surface nodes of simple cubic arrangement of spheres with 10, 20 and 32 spheres using LBM-FEM direct numerical simulations with $l_{fea} = 4$. The displacement response is compared to the analytical model proposed by de Boer et al.[25] . . 57

30 The average displacement of the top surface nodes of the model porous media geometries using simple cubic arrangement of spheres. The model geometries of 10, 20 and 32 spheres have been meshed using $l_{fea} = 2$. The displacement response is compared to the analytical model proposed by de Boer et al.[25] 58

31 Comparison of the velocity response of the model porous geometries made up of spheres with the analytical model. 59

32 Comparison of displacement along the z-axis from LBM-FEM simulations of SC arrangement and the de Boer et al. model at $\frac{t\nu}{R^2} = 24$. $z = 0$, represents the top surface and z is positive downwards 60

33 Setup and dimensions of model porous media geometry made up of cylindrical arrangements. Dotted lines shows the simulation domain. . 61

34 Setup and dimensions of the geometry used to determine permeability of the ordered orthogonally placed cylindrical arrangements. The color contours represents pressure variation at steady state. 63

35 Variation of pressure drop $(\frac{1}{\mu}\frac{dP}{dx})$ with average flow velocity V_{avg}. The slope of the line gives the permeability (κ^F). The velocity and pressure gradient values are in Lattice Boltzmann units. 63

36 Ordered orthogonally aligned axis, arrangement of two layers of cylinders. Due to symmetry, the dotted region can be taken as a unit cell which has the same elastic characteristics as the entire arrangement. . 65

37 Comparison between LBM-FEM simulations of saturated porous media compression with de Boer et al.[25] model. Deformational response of top surface nodes of 8, 16 and 32 cylinders geometries are shown. . . 69

38 Comparison of velocity response between LBM-FEM simulations of saturated porous media compression with de Boer et al.[25] model. Velocity response of top surface nodes of 8, 16 and 32 cylinder geometries are shown. 70

39 Comparison of displacement along the z-axis from LBM-FEM simulations of SC arrangement and the de Boer et al. model at $\frac{t\nu}{R^2} = 20$. $z = 0$ represents the top surface and z is positive downwards. 71

40 Water removal during wet pressing 72

41 Relative cost of water removal in forming, pressing and drying 73

42 Cost of drying with varying ingoing solid percentage 74

43 The four phase process of wet-pressing as proposed by Nilsson and Larson (1964) [60]. 75

44 Three dimensional image of a $3 \times 3 \times 3.5$ mm sample of wet-pressing felt. The image was generated using the X-ray microtomography images of the real felt sample and then using image processing to concatenate the images and reconstructing the solid model. 78

45 The fibrous microstructures considered in [69] from isometric and side views. a) 3D isotropic b) layered with random in-plane fiber orientation, c) highly oriented layered; d) disordered unidirectional e) disordered orthogonal media. 82

46 Permeability values from the numerical simulations of Tahir and Tafreshi [69]. The results are compared with the empirical model of Davis [22] and the analytical model of Speilman and Goren [67]. 84

47 The non-woven fibrous structure and the reconstructed 3D model developed by [40]based on DVI imaging, segmentation, voxel generation and complete 3D reconstruction. 85

48 The two different cylindrical arrangements considered to represent a more complex fibrous geometry like non-wovens, in the aspect of permeability behaviour. 87

49 Comparison of permeability of the skewed orthogonal and ordered orthogonal arrangement of cylinders. The empirical model of Davis [22] and the analytical model of Speilman and Goren [67] are provided for reference. Also included in the plot are the numerical simulation results of Jaganathan et al[40] for permeability in real non-woven structures. 89

50 Images of fibrous porous media obtained during various compression stages by 3D imaging and subsequent processing by Jaganathan et. al. 92

51 Geometry used to perform compression simulations of skewed orthogonal arrangement of cylinders. 92

52 Comparison of variation of n^S and T_{zz} in skewed orthogonal arrangement with Van Wyke's model. Also shown are results provided by Jaganathan et. al. of the variation of n^S with T_{zz} in real fibrous porous media. 94

53 The three regions in a wet-pressing felt. Protective layer consists of very fine fibers at the top of felt for good finishing of paper. The batt layer consist of fiber of intermediate diameter to prevent fine fibers from entering the base layer. The base layer provides strength and rigidity to the felt and consists of fibers with largest diameter. 97

54 Skewed orthogonal arrangement of cylinder and the two types of deformation occuring when external load is applied. 98

55 Non-homogeneous fibrous porous media constructed through the use of different diameter cylinders along the height of the porous media. . 100

56 Variation in bulk elastic modulus in compressive direction (along the height)for a sample geometry. 102

57 Deformation response of three skewed orthogonal arrangement of cylinders for the same applied compressive load. 104

58 Two different orthogonal arrangements of cylinders where the cylinder diameter varies along the the height of the structure. 105

59 Variation in the bulk modulus in nonhomogeneous ordered orthogonal arrangement of cylinders "nh1" and "nh2". 106

60 Loading and boundary conditions imposed on the model cylindrical structure for a deformational analysis. 107

61 Displacement response of the nonhomogeneous orthogonal cylindrical arrangements of "nh1" and "nh2". 108

62 10 spheres stacked vertically in a column of fluid, representing a simple cubic arrangement. The dotted line represents the simulation domain. 112

63 Average displacement of the top surface of spheres in simple cubic arrangement. The behaviour of displacement is the result of application of stepped loading condition. 113

64 Geometry and domain setup for performing flow calculations to determine permeability. 113

65 Variation of permeability with porosity during the compression of model porous media made up of spheres. The data is compared to the Kozeny-Carmen relationship. 115

66 A periodic structure of skewed orthogonal arrangement of cylinders used to in the simulation of compression to understand the behaviour of permeability with compression in fibrous porous media. 117

67 Undeformed and deformed configuration of a periodic structure representing the skewed orthogonal arrangement of cylinders. These geometries have been subsequently used to determine permeability using numerical flow analysis. 118

68 Comparison of experimental data by Koivu et al [48] for the variation of permeability with compression in a wet pressing felt with models by Hapel [35] and Davis [22]. 119

69 Darcian flow inside a saturated porous media. 127

LIST OF SYMBOLS OR ABBREVIATIONS

$\mathbf{T}$	Media stress tensor.
$\mathbf{T}^F$	Fluid stress tensor.
$\mathbf{T}_E^F$	Fluid extra stress tensor.
$\mathbf{T}^S$	Solid stress tensor.
$\mathbf{T}_E^S$	Solid extra stress tensor.
p	Hydrostatic pore pressure in fluid.
n^i	Volume fraction of ith phase.
ρ^{iR}	Real or effective density of ith phase.
ρ^i	Bulk density of ith phase.
$\mathbf{X}^i$	Position vector of ith phase in material coordinates.
$\mathbf{x}^i$	Position vector of ith phase in spatial coordinates.
$\mathbf{u}^i$	Displacement vector of ith phase.
$\dot{\mathbf{x}}, \mathbf{v}^i$	Velocity vector of ith phase.
$\mathbf{a}^i$	Acceleration vector of ith phase.
$\mathbf{F}^i$	Deformation gradient tensor of ith phase.
$\mathbf{E}^i$	Strain tensor of ith phase.
$\mathbf{w}^i$	Relative velocity vector between fluid and solid phase.
$\hat{\mathbf{p}}^i$	Interaction force vector for ith phase.
$\mathbf{b}^i$	Body force vector of ith phase.
μ^S, λ^S	Lame's constants .
ν^S	Poisson's Ratio.
μ^F	Fluid dynamic viscosity.
$\mathbf{K}^F$	Conventional (Darcy) permeability tensor.
K^F	Conventional (Darcy) coefficient of permeability .
κ^F	Intrinsic permeability coefficient.

γ^{FR}	Effective specific weight of the fluid.
ρ^*	Ratio of solid to fluid densities.
n^*	Ratio of solid to fluid volume fraction.
K^*	Non-dimensional coefficient of permeability.
D_p	Diameter of particle (spheres or cylinders).
Re	Reynolds number.
Ca	Capillary number.
LBM	Lattice Boltzmann method.
Δt^{LBM}	LBM time step.
Δx^{LBM}	Unit grid size of LBM.
f_k	LBM distribution function.
f_k^{eq}	LBM equilibrium distribution function.
τ	Single relaxation time constant for LBM.
k_B	Boltzmann constant.
$\mathbf{e}_k$	Discrete velocity directions in LBM.
c_s	Pseudo speed of sound in LBM.
FEM	Finite element method.
$[K]$	Stiffness matrix in FEM.
$[C]$	Damping matrix in FEM.
$[M]$	Mass matrix in FEM.
$\left[\hat{K}\right]$	Modified stiffness matrix in FEM.
ξ_i	Lagrangian shape functions in FEM.
$\hat{\boldsymbol{f}}$	Surface load vector in FEM.
γ	Newmark's Integration constant.
β	Newmark's Integration constant.
δt	Time step size in FEM.
g_c	Contact cut-off distance.

g_l	Gap between interacting surfaces along a link.
λ	Local Surface curvature.
A_c	Multiplier to the exponential contact force.
σ_c	Contact constant.
$\boldsymbol{v}_a$	Approach velocity of interacting surfaces.
$\boldsymbol{v}_b$	Velocity of boundary at the link.
$\boldsymbol{p}_k$	Fluid structure interaction force vector along the kth link direction.
$\boldsymbol{f}_k$	Contact force vector along the kth link direction.
l_{fea}	Ratio of fea mesh edge length to lbm mesh edge length.
$\mathcal{S}_n$	Speedup on n processors.
$\mathcal{E}_n$	Efficiency on n processors.
T_x	Wall time to run on x processors.
T_{xn}	Wall time to run on xn processors.
$U\%$	Degree of consolidation.
m_v	Coefficient of volume compressibility.
T_v	Terzaghi's time factor.
E_b	Instantaneous elastic modulus of a solid structure.
E_{avg}	Time averaged elastic modulus of a solid structure.
E	Young's Modulus .
I	Moment of Inertia .
α	Displacement due to contact of two spherical surfaces .
a	The radius of surface formed due to contact .

SUMMARY

Applications of fluid infiltrated deformable porous media range from soil consolidation, filtration and absorbancy products, fabric and textiles to human tissue and bone modeling. Understanding the behaviour of these media under externally applied load is critical to the design and development of products related to these media.

In deformable porous media, the geometrical complexity of the solid structure coupled with the need for a unified treatment of all the interacting phases makes a micromechanical approach of the problem intractable. Thus, the existing techniques, such as "Biot's theory" or the "Theory of Porous Media" are based on homogenization techniques, in the sense that they assume the solid and all the fluid phases as a smeared media. These kind of approaches, inspite of their mathematical rigour, are not suitable for micromechanical investigations such as the effect of microstructure on the deformational behaviour or the constitutive relations in the media during deformation. In order to perform such investigations an approach based on direct numerical simulations, capable of leveraging the ever increasing computational power would be ideally suited.

In this research work, a numerical scheme based on the hybrid lattice-Boltzmann finite-element method is developed to carry out the direct numerical simulations of deformable porous media. The method has been parallelized to make use of distributed computing. The efficiency and inherent parallel nature of the lattice Boltzmann method coupled with the robustness of finite element method implemented in a parallel framework provided by the highly scalable toolkit of PETSc lend as a powerful tool to not only takle the problem of deformable porous media but also to

undertake any problem involving complex interaction of fluid and solid phases in the linear elastic limit within the small to medium time and spatial scales.

The method has been used to understand the deformational characteristics of model porous media made up of spheres and cylinders. The deformational response of the model porous media constructed in this fashion is compared to existing analytical solution. For the comparison, the bulk properties of the macroscopic porous media are obtained through the single phase properties of the constituent phases. The deformational behaviour is seen to match with the analytical solution closely. Thus it is found that macroscopic behaviour of a generic porous media can be recovered with the use of model porous media constructed with simplified geometries.

This finding motivated research in using model porous geometries to represent the more complex real porous geometries in order to perform investigations of deformation on the latter. An attempt has been made to apply this technique to the complex geometries of "felt", (a fibrous mat used in paper industries) to recover its deformational behaviour. These investigations lead to new understanding on the effect of fiber diameter on the bulk properties of a fibrous media and subsequently on the deformational behaviour of the media. Additionaly this approach offers tremendous decrease in the computational load and meshing time, while providing capturing the relevent behavioural characteristics of the media without any approximations.

Further the method has been used to investigate the constitutive relationships in deformable porous media that are effected by the microstructure of the solid phase. Particularly the relationship between permeability and porosity during the deformation of the media is investigated. Results show the need of geometry specific investigations.

CHAPTER I

INTRODUCTION

A majority of solids we encounter regularly are made up of a homogeneous or non-homogeneous solid phase with interstitial spaces called pores which are filled with fluid. In some, the pores are clearly visible (sponge, soil) while in others not so clearly (human tissue, wood, brick). These kinds of solids can generally be categorized as porous media. Within porous media the solids are again classified based on their ability to deform under the application of an external force as rigid porous media (brick, concrete etc.) and deformable porous media (soil, sponge, human tissue etc.). There are a broad range of problems involving deformable saturated porous media. The problems range from understanding geotechnical questions like the consolidation problem in solid mechanics to improving the efficiency of de-watering in the process of wet-pressing in paper industry by developing better felt designs. The problems can be extended to include impact absorbing polymeric foams used in automobile industry and bio-materials like bones, cartilage and tissue. Consequently, it is no coincidence that such porous media have been studied extensively.

However, the analysis of fluid infiltrated deformable porous media present the challenge of not being uniquely classified into the well defined fields of "solid mechanics" or "fluid mechanics". Rather, it is a tightly coupled multiphasic problem, where a unified treatment of all the phases are required to track the dynamics accurately. Typically, such a unified analysis requires different frames of reference for solid (Lagrangian) and fluid (Eularian) phases. Additionally, the complex geometrical structure of the solid skeleton makes any analytical approach based on a micro-mechanical

treatment, intractable. Thus, most of the work in this field has been based on homogenization or mixture theory such as the Biot's theory of poroelasticity and the theory of porous media (TPM). Such techniques are based on a macro-mechanical approach where the porous media and its constituents are assumed as a smeared media. In these methods, the balance equations are applied on individual phases and in order to obtain closure assumptions need to be made regarding the interaction phenomena and also the constitutive relations. Thus these techniques do not allow for the investigation of effect of microstructure on the various properties of the porous media or the constitutive relationships between critical properties of the media.

However there are a number of problems which require understanding of the effect of microstructure on the deformational behavior and where the constitutive relations are unknown. In such cases, a micro-mechanical approach that takes into account the micro-structure of the solid skeleton and its effect on the interaction between the various phases would be well suited. A numerical approach based on direct numerical simulations is one such micro-mechanical approach that would be ideally suited for such investigations.

The goal of this research work is to develop a numerical tool that would allow micro-mechanical investigations in deformable porous media using direct numerical simulations. A hybrid lattice-Boltzmann finite element method has been used to solve the coupled fluid-solid interaction problem. The method has been parallelized to make use of distributed computing, which is essential for solving coupled fluid-structure interaction problems in complex geometries like porous media.

This powerful numerical too has been used to carry out investigations in model porous media made of spheres and cylinders. The results provide new understanding on using simplified geometries made up of spheres or cylinders to recover the behavior of more complex real geometries. Further investigations are conducted on understanding the constitutive relationships such as that between permeability and

porosity during the deformation of the media.

1.1 Deformable Porous Media Models

Karl Von Terzaghi is credited for being the first to study the problem of compression of deformable porous media. He proposed the principle of effective stress[1925], according to which, the total applied stress (T) on a porous media is distributed between the fluid pressure (T^F) and the structural stress (T^S), given as

$$T = T^F + T^S, \tag{1}$$

here the structural stress T^S alone is responsible for the deformation of the solid phase.

Terzaghi used a phenomenological argument to solve the problem of one-dimensional consolidation in a saturated porous media. The governing equation for the one-dimensional compression process is given as

$$\frac{\partial p}{\partial t} = \frac{K^F}{\rho g m_v} \frac{\partial^2 p}{\partial z^2}, \tag{2}$$

where $p = p(z,t)$ is the pore pressure of fluid, K^F is the permeability with dimensions LT^{-1}, ρ is the density of the fluid and g is the acceleration due to gravity. m_v is the *coefficient of volume compressibility*. It represents the compression of media per unit of original thickness, due to unit increase of pressure and is to be determined experimentally. Terzaghi defined the term $\frac{K^F}{\rho g m_v}$ as c_v called the coefficient of consolidation.

Terzaghi solved the above diffusion equation and provided the solution in the form

$$U\% = f(T_v), \tag{3}$$

where $U\%$ is the ratio of current compression S to the final compression S_∞ called the degree of consolidation and T_v is a pure number given as $\frac{c_v}{H^2}t$ where H is the height of the consolidation region. He called this number time factor. He proposed

that since the soil constants and the thickness of the layer enter into equation 3 only in the combination represent, the term can be considered as a similarity parameters that defines the deformational behavior of the soil.

1.1.1 Poroelasticity: Biot's Theory

The pioneering work of Boit [9, 10, 12, 11] provided significant contributions to the field of saturated deformable porous media. Biot based his theory on the description of porous media by Terzaghi as a solid structure infiltrated with freely moving fluid. This formed the basis of the theory of poroelasticity also called Biot's Theory (BT).

Biot [9], made the assumption of a homogeneous media, subjected to small strain with linear constitutive relationship for its media. Further he assumed a reversible process where the fluid flow can be described by Darcy's law. The governing equations were provided using the solid displacement vector u_i and the fluid pressure p as the independent variables. Biot proposed that the physical properties of an isotripic porous media like soil can be described completely by four parameters given as E_b the bulk elastic modulus, ν^S the Poisson ratio, $1/H$ measures the compressibility of porous media for a change in the fluid pressure, while $1/R$ is the measure of the change in fluid content for a given change in fluid pressure.

In addition Biot also proposed some derived variables. For instance, if G is the shear modulus, α is a coefficient defined as

$$\alpha = \frac{2(1+\nu)}{3(1-2\nu)}\frac{G}{H}, \tag{4}$$

which measures the ratio of the water volume squeezed out to the volume change of the soil if the later is compressed while allowing the water to escape ($p = 0$). The coefficient $\frac{1}{Q}$ defined as

$$\frac{1}{Q} = \frac{1}{R} - \frac{\alpha}{H}, \tag{5}$$

is a measure of the amount of water which can be forced into the porous media under pressure while the volume of porous media is kept constant. The coefficient a called

the *final compressibility* is defined as

$$a = \frac{(1-2\nu)}{2G\,(1-\nu)}. \tag{6}$$

Finally, the *consolidation constant* c is defined as

$$\frac{1}{c} = \alpha^2 \frac{a}{K^F} + \frac{1}{QK^F}, \tag{7}$$

where k is the permeability of the isotropic porous media. The consolidation constant has dimensions of T^{-1} thus provides some understanding of the deformability of a saturated porous media under external loading.

In subsequent work [10], Biot used a more general and direct approach to extend the theory to anisotropic porous media. Another significant contribution [12, 11] was the development of "Theory of Propagation of Waves". In this work, Biot proposed the presence of two dilational waves and a rotational wave in a homogeneous, linear elastic porous media.

1.1.2 Theory of Porous Media

The theory of porous media (TPM) [16, 32] is based on the mixture theory extended by the concept of volume fractions. Within the framework of TPM the fluid-saturated porous media is assumed to be a binary mixture of two immiscible constituents ϕ^i with particles X^i $(i = F, S)$ denoting the fluid and solid phases respectively, each of which is regarded as a continuum following its own motion. Thus, at any time t, each spatial position $\mathbf{x}$ is simultaneously occupied by particles X^i of both constituents ϕ^i. $\mathbf{X}^i$ denotes the reference positions of phase ϕ^i. Each constituent is assigned its own motion function $\xi_\mathbf{i}$

$$\mathbf{x}_i = \xi_i(\mathbf{X}_i, t). \tag{8}$$

The volume fraction of each phase is given by

$$n^i = n^i(\mathbf{x}, t). \tag{9}$$

ρ^{iR} is defined as the real or effective density and ρ^i is defined as the bulk density, given as

$$\rho^i = n^i \rho^{iR}. \tag{10}$$

For the case of fluid-saturated porous media which can be represented as a binary mixture we have

$$n^S + n^F = 1. \tag{11}$$

The solid motion can be described in a Lagrangian setting by introducing the displacement vector of the solid phase, as

$$\mathbf{u}^S = \mathbf{x}_i - \mathbf{X}_i. \tag{12}$$

The pore fluid is described relatively to the deforming skeleton by the so called seepage velocity

$$\mathbf{w}^F = \dot{\mathbf{x}}^F - \dot{\mathbf{x}}^S. \tag{13}$$

From equations 8 and 12, the solid deformation gradient tensor is defined as

$$\mathbf{F}^S = \frac{\partial \mathbf{x}^S}{\partial \mathbf{X}^S} = \mathbf{I} + \frac{\partial \mathbf{u}^S}{\partial \mathbf{X}^S}. \tag{14}$$

de Boer et. al. [24] and Ehlers [30] have provided the conservation and balance equations for such a system of binary mixtures. The conversation of mass is given as

$$\frac{\partial \rho^i}{\partial t} + \nabla_{\mathbf{i}} \cdot (\rho^i \dot{\mathbf{x}}^{\mathbf{i}}) = 0, \tag{15}$$

where $\nabla_{\mathbf{i}} \cdot$ represents the divergence with respect to reference configuration $\mathbf{X}^i$ and $\dot{\mathbf{x}}^{\mathbf{i}}$ represents the velocity of ϕ^i. The balance of momentum is given as

$$\nabla_{\mathbf{i}} \cdot \mathbf{T}^{\mathbf{i}} + \rho^i (\mathbf{b}^{\mathbf{i}} - \ddot{\mathbf{x}}^{\mathbf{i}}) + \hat{\mathbf{p}}^{\mathbf{i}} = 0, \tag{16}$$

where $\mathbf{T}^{\mathbf{i}}$ represents the Cauchy stresses, $\mathbf{b}^{\mathbf{i}}$ is the body force and $\ddot{\mathbf{x}}^{\mathbf{i}}$ is the acceleration of ϕ^i. $\hat{\mathbf{p}}^{\mathbf{i}}$ is the momentum supply term and for a bi-phasic fluid saturated porous media we have

$$\hat{\mathbf{p}}^S + \hat{\mathbf{p}}^F = 0 \tag{17}$$

Here we assume an isothermal model, thus we do not take into consideration the energy equation.

The new findings in the constitutive theory of porous media [15, 14] led to consistent structure of constitutive equations with the requirements of thermodynamics and experimental observations. TPM makes use of the thermodynamical restrictions resulting from the assumption of a second grade material [74] and the application of entropy inequality. Following the incompressibility constraint, $\rho^{iR} = constant$, the stress tensors and the interaction force can be additively decomposed. Here it is assumed that the constitutive relations for the liquid or gas partial constituents are governed by weighted (by the volume fraction of fluid) pore-fluid pressure, whereas the constitutive equations for Cauchy's stress tensor of the partial porous solid constituents consists of two parts, namely the weighted (by volume fraction of solid phase) pore-fluid pressure and of "effective stresses" determined by the motion of the partial solid phase. Thus, the stresses are given as

$$\mathbf{T}^S = -n^S p\mathbf{I} + \mathbf{T}^S_E, \tag{18}$$

$$\mathbf{T}^F = -n^F p\mathbf{I}, \tag{19}$$

where $\mathbf{I}$ is the identity tensor p is the pore-pressure of fluid. The interaction force $\hat{\mathbf{p}}^i = \hat{\mathbf{p}}^F = -\hat{\mathbf{p}}^S$ given as

$$\hat{\mathbf{p}}^F = p\nabla n^F + \hat{\mathbf{p}}^F_E, \tag{20}$$

consists of two parts, the weighted pore-fluid pressure and an "effective" interaction force. Where it is assumed that the extra stress term $\mathbf{T}^F_E$ associated with the fluid stress tensor can be neglected as the fluid frictional force $div\mathbf{T}^F_E$ is negligible compared to the extra momentum production term $\hat{\mathbf{p}}^{\mathbf{F}}_{\mathbf{E}}$.

Further constitutive relations are required for the solid extra stress tensor $\mathbf{T}^S_E$ and the interaction force term $\hat{\mathbf{p}}^F_E$ in order to close the model. [30] proposes the "effective" interaction force term to be proportional to the relative velocity of both

phases, assuming the mixture is close to equilibrium state. Thus,

$$\hat{\mathbf{p}}_E^F = -\mathbf{S}_v \mathbf{w}^F, \tag{21}$$

where $\mathbf{S}_v$ is a positive response constant and in the case of isotropic permeability is given as

$$\mathbf{S}_v = \frac{(n^F)^2 \gamma^{FR}}{K^F}, \tag{22}$$

where γ^{FR} is the effective specific weight of the pore fluid and K^F is the conventional (Darcy) coefficient of permeability. Thus this model is applicable for creeping flow where Darcy's law is applicable. In fact substitution of equations 21 and 22 in the fluid momentum balance relation 16 results in the recovery of Darcy's equation.

For the solid extra stress tensor $\mathbf{T}_E^S$ a number of different constitutive relationships have been proposed based on the properties of the solid skeleton of the porous media.

To model linear elastic deformation of the extra stress tensor is given as

$$\mathbf{T}_E^S = 2\mu^S \mathbf{E}^S + \lambda^S (\mathbf{E}^S \cdot \mathbf{I})\mathbf{I}, \tag{23}$$

where μ^S, λ^S are the Lame's constants and $\mathbf{E}^S$ is the elastic strain tensor given as

$$\mathbf{E}^S = \frac{1}{2}\left(\mathbf{F}^T\mathbf{F} - \mathbf{I}\right). \tag{24}$$

de Boer et. al[25] used the above relation to solve the governing equation in time for a one-dimensional semi-infinite saturated deformable porous media under an compressive load (described in section 1.1.2.1). Thus proposed the behavior of wave-propagation in a saturated porous media.

Ehlers [30] proposed constitutive relations for an elasto-plastic solid skeleton. Proceeding from the assumption of a second-grade material (Wang [74]), elasto-plasticity is taken into account by means of a multiplicative decomposition of the first and second solid deformation gradient tensors.

deBoer and Bluhm [23] developed constitutive relations for modeling compressibility of the constituents of the porous media. They deduced that the effective stress in the solid phase are influenced by the reduced pore liquid pressure.

[31] developed a new finite elasticity law on the basis of hyperelastic strain energy function to model finite deformation in an incompressible liquid saturated deformable porous media.

Further work by [33, 32] lead to the development of constitutive relations for a linear elasto-plastic and visco-elastic solid skeleton.

In other developments, the governing equations have been transformed towards a weak form and the resulting model equations have been solved using finite element method (Diabels & Ehlers [26], Ehlers & Markert [32]). With the use of finite elements analysis of saturated porous media has been extended to arbitrary geometries.

1.1.2.1 Response of one-dimensional semi-infinite deformable porous media

de Boer et. al [25] solved the above equations in one-dimension for the problem of wave propagation in a semi-infinite fluid-saturated porous media. They assumed the strains to be in infinitesimally small resulting in the neglect of any variation in volume fractions. The resulting response of displacement $u(x,t)$ is given as

$$u(z,t) = -\frac{1}{\sqrt{a}(\lambda^S + 2\mu^S)} \int_0^t \left[f(t-\tau) e^{-\frac{b}{2a}\tau} I_0\left(\frac{b\sqrt{\tau^2 - az^2}}{2a}\right) U\left(\tau - \sqrt{a}z\right) \right] d\tau \quad (25)$$

where $f(t)$ is the applied time varying stress load, $I_0(z)$ is the modified Bessel's function of order zero, $U(t)$ is a unit Heaviside function, λ^S and μ^S are the Lame's constants and a, b are given as

$$a = \frac{(n^S)^2 \rho^F + (n^F)^2 \rho^S}{(\lambda^S + 2\mu^S)(n^F)^2}, b = \frac{S_v}{(\lambda^S + 2\mu^S)(n^F)^2}. \quad (26)$$

where

K^F is the conventional saturated permeability with dimensions LT^{-1} and γ^{FR} is the real or effective specific weight of the fluid.

Figure1 shows the response of displacement of the top surface of the semi-infinite medium with time for the values of parameters shown in table 1

Table 1: Parameters in de Boer et. al. model and their values for the test problem.

n^F	0.33
n^S	0.67
ρ^{FR}	1000 kg/m^3
ρ^{SR}	2000 kg/m^3
λ^S	5.5833 MN/m^2
μ^S	8.3750 MN/m^2
K^F	0.01 m/s
γ^{FR}	10.0 KN/m^2
$f(t)$	3.0 KN/m^2

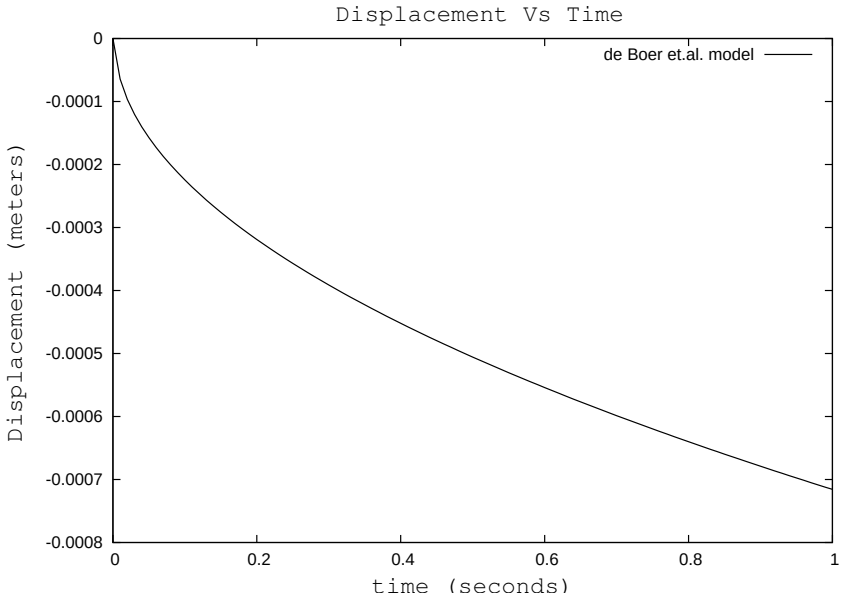

Figure 1: Response of solid displacement w.r.t time for step loading

Subsequently, Diebels and Ehlers [26] have used the analytical solution given by equation 25 to validate their non-linear finite element model based on the TPM to simulate binary saturated porous media. More recently Hu et.al [37] used the analytical solution to validate their binary porous media model based on differential quadrature method for spatial discretization and second-order backward difference scheme for time discretization.

1.1.3 Literature Gap

As seen from the above literature TPM, based on the theory of mixtures and extended by the concept of volume fractions, has made rapid and significant strides over the last two decades. Unlike Biot's theory, TPM is based on rigorous thermodynamical principles and thus finds applications in a more generic class of problems related to deformable porous media. The developments in this field have incorporated saturated and unsaturated; incompressible and compressible; isotropic and anisotropic porous media and have also included solid skeletons that are linear elastic, elasto-plastic, visco-elastic and visco-elasto-plastic materials. Further, recently the field has been advances to the area of ionic porous media [38].

Thus it is clear that the understanding in the area of deformable porous media has been vastly improved due to the developments and applications of TPM. As a result, TPM would be the prefered tool to investigate the behavior of homogeneous deformable porous media.

However, being based on mixture theory the method is not suitable for investigating non-homogeneous deformable porous media, where the varying spatial and temporal properties of the porous structure due to varying microstructure of the porous media, cannot be accounted using the principles of TPM. Furthermore, TPM is also not well suited to investigate the constitutive relations, since these are derived based on thermodynamical constraints. Of particular interest are the variation of

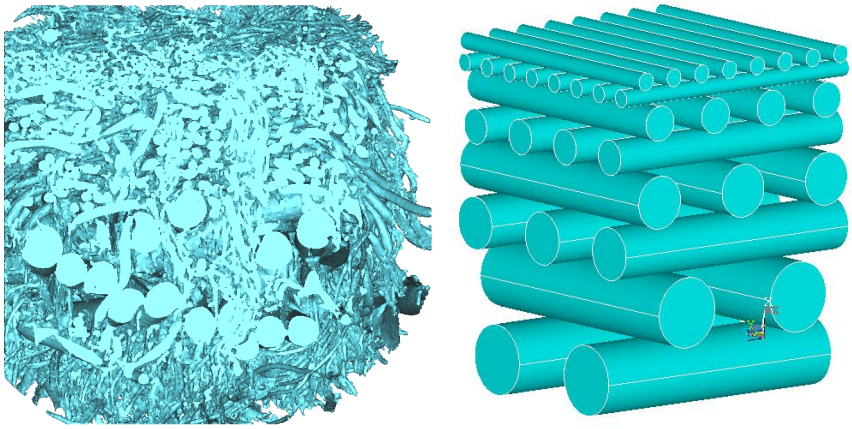

(a) 3D Felt (b) Model Geometry

Figure 2: Three dimensional image of a $3 \times 3 \times 3.5$ mm sample of wet-pressing felt. The model geometry of cylinder in orthogonal arrangement.

permeability with porosity and the variation of solid skelon properties with porosity during a deformation process.

Fibrous porous media such as wovens and non-wovens find applications in a number of different industrial products including absorbency products, filtration products and packaging products. The requirements on some of these fibrous porous media necessitate non-homogeneity in their structure. For instance in paper industry, a fibrous porous mat called "felt" is used to transport paper through the various wet-pressing stages (section 5.1). Figure shows a solid model of a $3 \times 3 \times 3.5mm$ sample of a wet-pressing felt. The manufacturing process of such felts consists of "laying" out layers of fibers with varying fiber diameter and then using a process called "pinning" to push fibers from one layer into another and obtain rigidity in the struture. Due to this kind of manufacturing process the felts can be termed as layered fibrous porous media.

The figure 2a shows that there is a large variation in the fiber diameter and possibly the porosity in the felt structure. Understanding the effect of such non-homogeneity on the deformational behaviour of felt is critical to the development of felts that improve the de-watering efficiency. For instance, existing research shows that high

compressibility and low water retention are two desirable characteristics of felts for improved water removal. However, there is not much literature on the effect of various properties of felt such as fiber diameter, fiber arrangement, non-homogeneity of fiber diameter and porosity on the deformational behaviour of felts.

Direct numerical simulation would be an ideal tool to understand the effect of the above mentioned parameters of a fibrous porous media on its deformational behaviour. However performing direct numerical simulation of compression of a saturated fibrous media with geometry as shown in figure 2a presents numerous challenges, which fall outside the capabilities of the developed high-fidility LBM-FEM technique. Firstly, meshing the shown geometry for a finite element analysis is a non-trivial task. Secondly, the number of degrees of freedom generated in such a mesh, if successfully completed would be of the order of $10^8 - 10^9$ which would require petascale computing. Moreover, even if such an analysis is performed, the results only give information of the selected $3 \times 3 \times 3.5mm$ sample of a wet-pressing felt. Many more of such simulations have to be performed to obtain a generalized result.

Another approach to this problem would to develop model geometries made of spheres or cylinders in regular arrangement that can accurately represent the macroscopic behaviour of such complex geometries as a felt, shown in figure 2. The present research work addresses this issue. Chapter 5 discusses the use and development of model geometry to represent real layered fibrous porous media.

1.1.4 Important parameters

The volume fraction of each of the component phases n^i is an important parameter in the problem of compression of deformable porous media. In this work, we only look at saturated deformable porous media, thus the solid volume fraction (n^S) and the fluid volume fraction (n^F) are related as

$$n^S + n^F = 1. \tag{27}$$

Thus, information of n^S can lead to n^F and vice versa. Throughout the dissertation these two parameters are used interchangably.

The parameter which gives a measure of the fluid conductivity through the porous media is the permeability. In literature there are two variants of permeabilities used. The conventional permeability, also called Darcy permeability given by K^F and the intrinsic permeability given by κ^F. Appendix A gives a detailed description of both the permeability and their relationship.

The parameter that gives a measure of the rigidity of the porous structure is the bulk elastic modulus E_b. Note that in future we use E_b to refer to the bulk elastic modulus for compression of the porous media. A nondimensional parameter E^* can be used instead and is given as $E^* = E_b/E$.

The strain number given as $\varepsilon^* = \frac{T_{zz}}{E_b}$, where T_{zz} is the compressive stress load, gives an estimate of the strain in the porous media or the extent of compression.

Finally the parameters Reynolds number (Re) and capillary number (Ca) provide the relative effects of inertial to viscous forces and viscous to deformation forces respectively. These parameters are given as

$$Re = \frac{U^F_{avg} D_p}{\nu^F}, \quad Ca = \frac{\dot{\varepsilon}\mu^F}{E_{avg}}, \tag{28}$$

where U^F_{avg} is the average flow velocity in the porous media and ν^F is the fluid kinematic viscosity, $\dot{\varepsilon}$ is the strain rate and E_{avg} is the average bulk modulus of the media.

CHAPTER II

METHODOLOGY

Problems in which fluid and solid interact dynamically, require the simultaneous solution of both the tightly coupled phases. Schemes for direct numerical simulations that undertake the task of solving such problems have to overcome a number of related challenges. Solution of both the phases simultaneously, accurate transfer for force and displacement information between the phases and resolving instability that arise due to time stepping routines are some of them. In the case of saturated porous media the complexity of the solid structure is an additional challenge that needs to be resolved usually through high spatial and temporal resolution. These challenges make traditional methods computationally expensive and impractical.

For modeling fluid flow, the Lattice-Boltzmann method (LBM) has evolved as an attractive alternative. The accuracy of Lattice-Boltzmann method has been shown to be comparable to traditional numerical methods like Finite-Volume, Finite-Difference and Finite-Element [Noble et al [61]; Bernsdorf et al [5], Breuer [17]]. Further, for solving flows in complex geometries like porous media, the Lattice-Boltzmann method has proved to be more efficient than traditional methods [Bernsdorf et al [4]]. The recently published review paper by Aidun and Clausen [1] provides an excellent review of the use of LBM for complex flows and its capabilities. One of the strengths of LBM is the local nature of the calculations, which makes the method amenable to distributed computing. Clausen et. al [21] have shown the excellent scaling of the LBM for petascale computing. This feature of LBM is very important for this research work, as the size of the computational domain turns out to be too large to be solved efficiently using serial computing. In this work, the BGK Lattice-Boltzmann method

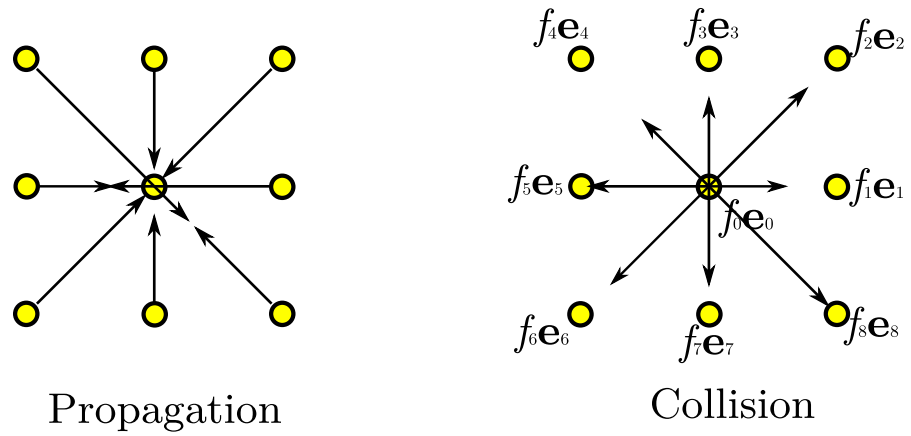

Figure 3: Propagation and collision steps in two dimensional lattice Boltzmann scheme. Fluid particles move in discrete velocity directions represented by $\mathbf{e}_i$.

with single-relaxation, as implemented in Aidun et al[2] has been used.

In this study, as a first approximation, a linear elastic model has been used for simulating the deformation of the solid structure. The Finite Element method with 4-node linear quadrilateral elements has been used to discretized the geometry and form the weak system. The reason for using Finite Element method for modeling the deformation of the solid phase is its robustness and accuracy. Further there has been progress in the development of efficient parallel iterative schemes [Saad [65]] that make the solution of solid phase easy. Also with the improvements in meshing algorithm, it is now trivial to mesh a complex geometry such as a porous media.

In the following, the Lattice-Boltzmann method and Finite-Element technique are outlined with information on parallelizing the code and running on large clusters.

2.1 Lattice Boltzmann Method

The lattice-Boltzmann method (LBM) is based on a specialized discretization of the continuous Boltzmann equation. As such, it is a kinetic model that models the fluid phase at a mesoscopic level. The LBM starts with an initial lattice as shown in figure 3, where each lattice node is characterized by a particle distribution function $f_k(\boldsymbol{x}^e, t)$. The distribution function gives the probability of finding a particle at position $\boldsymbol{x}$,

time t and moving in the discrete direction k. The evolution of $f_k(\boldsymbol{x}, t)$ with time is governed by the lattice-Boltzmann equation given as

$$f_k(\boldsymbol{x}^e + \boldsymbol{e}_k, t+1) = f_k(\boldsymbol{x}^e, t) + \frac{1}{\tau}[f_k^{eq}(\boldsymbol{x}^e, t) - f_k(\boldsymbol{x}^e, t)]. \tag{29}$$

Here $f_k^{eq}(\boldsymbol{x}^e, t)$ is the equilibrium distribution function at $(\boldsymbol{x}^e, t)$, τ is the single relaxation time constant and $\boldsymbol{e}_k$ is the discrete velocity vector. The fluid density ρ and the macroscopic fluid velocity $\boldsymbol{u}(\boldsymbol{x}^e, t)$ are obtained from the first two moments, given by

$$\rho(\boldsymbol{x}^e, t) = \sum_k f_k(\boldsymbol{x}^e, t) \quad \text{and} \quad \rho(\boldsymbol{x}^e, t)\boldsymbol{u}(\boldsymbol{x}^e, t) = \sum_k f_k(\boldsymbol{x}^e, t)\boldsymbol{e}_k. \tag{30}$$

The most common lattice model for two–dimensional case is D2Q9 model which uses nine discrete velocity directions, while the model for three–dimensional case is D3Q19, which uses cubic lattice with nineteen discrete velocity directions [2] for the fluid particles moving along the horizontal, vertical and diagonal links. The equilibrium distribution function is defined as

$$f_k^{eq} = w_k \rho \left[1 + 3\boldsymbol{e}_k \cdot \boldsymbol{u} + \frac{9}{2}(\boldsymbol{e}_k \cdot \boldsymbol{u})^2 - \frac{3}{2}|\boldsymbol{u}|^2\right], \tag{31}$$

with $w_0 = 4/9$ for fluid particles at rest, $w_{1-4} = 1/9$ for fluid particles moving in non-diagonal directions, and $w_{5-8} = 1/36$ for diagonal directions in two-dimensional D2Q9 model; and $w_0 = 1/3$, $w_{1-6} = 1/18$ (non-diagonal directions), and $w_{7-18} = 1/36$ (diagonal directions) in three-dimensional D3Q19 model. For the present model, the pseudo speed of sound is $c_s = \sqrt{1/3}$ and the kinematic viscosity is $\nu = (2\tau - 1)/6$. In the longer time scale, the LBM is effectively solving the Navier–Stokes equations.

2.2 Finite Element Method

The deformation of the porous structure has been approximated using a linear elastic model. Within the elastic limit the Cauchy's equation governs the transient behavior of deformation inside the solid structure. The Cauchy's equation is given as

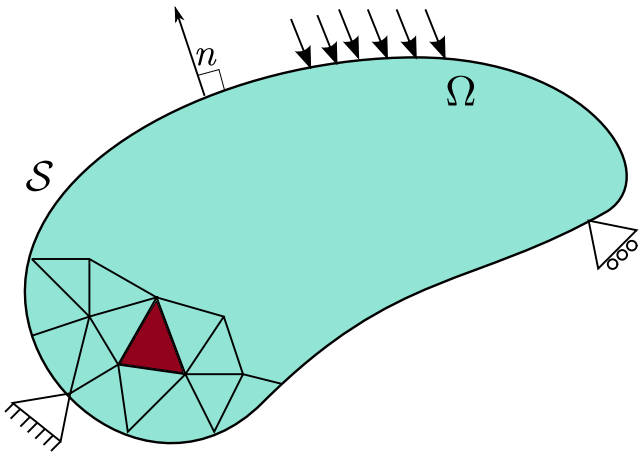

Figure 4: Approximating a continuous solid domain using finite elements.

$$\boldsymbol{\nabla} \cdot \boldsymbol{T} + \rho \boldsymbol{g} = \rho \ddot{\boldsymbol{u}} \tag{32}$$

where $\boldsymbol{T}$ is the Cauchy's stress tensor, $\rho \boldsymbol{g}$ is the body force and $\ddot{\boldsymbol{u}}$ is the resulting acceleration. The weak form of the equation using Principle of Virtual displacement is given as

$$\int_V \left[\boldsymbol{E} : \boldsymbol{T} + \rho \ddot{\boldsymbol{u}} \cdot \delta \boldsymbol{u} \right] \, \mathrm{d}V = \int_V \rho \boldsymbol{g} \cdot \delta \boldsymbol{u} \, \mathrm{d}V + \int_S \hat{\boldsymbol{f}} \cdot \delta \boldsymbol{u} \, \mathrm{d}S \tag{33}$$

where V and S represents the volume and the boundary of the domain. $\delta \boldsymbol{u}$ represents the virtual displacement, $\boldsymbol{T}$ and $\boldsymbol{E}$ represent the stress and strain tensors respectively and $\rho \boldsymbol{g}$ and $\hat{\boldsymbol{f}}$ represent the body and surfaces forces respectively.

The geometry has been discretized using four-node tetrahedral elements as shown in figure 5. Within each element deformation $\boldsymbol{u}$ is approximated using Lagrangian shape functions as

$$\boldsymbol{u}\left(x, y, z\right) = \sum_{i=1}^{n} \bar{\boldsymbol{u}}_{\boldsymbol{i}} \psi_i \left(x, y, z\right) \tag{34}$$

where n represents the nodes per element, $\bar{\boldsymbol{u}}_{\boldsymbol{i}}$ is the value of $\boldsymbol{u}$ at node i and ψ_i are the Lagrangian shape functions for a tetrahedral element given as

Figure 5: Master tetrahedral element

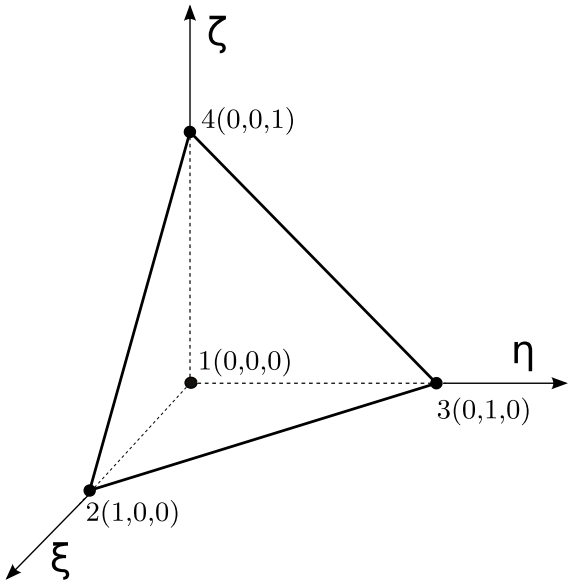

$$\psi_i(\xi,\eta,\zeta)\begin{cases}\psi_1 = 1-\xi-\eta-\zeta,\\ \psi_2 = \xi,\\ \psi_3 = \eta,\\ \psi_4 = \zeta,\end{cases} \tag{35}$$

The constitutive relations between stress and strain, the compatibility relations of linear elasticity and the equations for the approximation of $\boldsymbol{u}$ are substituted in the weak form given by equation 33. Subsequently the boundary conditions and the condition of continuity of solution are applied to obtained system of equations. The resulting system is given as

$$[M]\{\ddot{u}\} + [C]\{\dot{u}\} + [K]\{u\} = \{f\} \tag{36}$$

where $[M]$ is the mass matrix, $[C]$ is the damping matrix, $[K]$ is the stiffness matrix, $\{f\}$ is the force vector and $\{u\}$ is the displacement vector.

To integrate the second order system of equations in time, the Newmark's scheme is adopted. The deformation and its derivatives for time $t+1$ are approximated using

their values at time t as follows

$$\{u\}_{t+1} = \{u\}_t + \Delta t \{\dot{u}\}_t + \frac{\Delta t^2}{2}\left[(1-2\beta)\{\ddot{u}\}_t + 2\beta\{\ddot{u}\}_{t+1}\right] \tag{37}$$

$$\{\dot{u}\}_{t+1} = \{\dot{u}\}_t + \Delta t\left[(1-\gamma)\{\ddot{u}\}_t + \gamma\{\ddot{u}\}_{t+1}\right] \tag{38}$$

where Δt is the timestep and γ, β are Newmark's integration constants that determine the stability and accuracy of the scheme. We choose γ=0.5 and β=0.25 resulting in a constant-average acceleration method that is unconditionally stable.

Substituting equations 37 and 38 into the system of equations given by equation 36 and evaluating the deformation at time $t+1$, we obtain

$$\left[\hat{K}\right]\{u\}_{t+1} = \left\{\hat{f}\right\}_{t+1} \tag{39}$$

where $\left[\hat{K}\right]$ is given as

$$\left[\hat{K}\right] = [K] + \frac{\gamma}{\beta\Delta t}[C] + \frac{1}{\beta\Delta t^2}[M] \tag{40}$$

and $\left\{\hat{f}\right\}_{t+1}$ is given as

$$\begin{aligned}\left\{\hat{f}\right\}_{t+1} = \{f\}_{t+1} + [C]\left\{\frac{\gamma}{\beta\Delta t}\{u\}_t + \left(\frac{\gamma}{\beta}-1\right)\{\dot{u}\}_t + \left(\frac{\gamma}{2\beta}-1\right)\Delta t\{\ddot{u}\}_t\right\} \\ + [M]\left\{\frac{1}{\beta\Delta t^2}\{u\}_t + \frac{1}{\beta\Delta t}\{\dot{u}\}_t + \left(\frac{1}{2\beta}-1\right)\{\ddot{u}\}_t\right\}\end{aligned} \tag{41}$$

Note that equation 39 is an implicit equation in the sense that the deformation $\{u\}_{t+1}$ at time $t+1$ is dependent on the force vector $\{f\}_{t+1}$ at time $t+1$. The stiffness matrix $\left[\hat{K}\right]$ is invariant in time. Iterative solvers are used to solve the system.

In the above equation the force vector $\{f\}_{t+1}$ consists of two components. One component is the applied external load on the geometry $\{f\}^{ext}_{t+1}$ which can be easily evaluated for time $t+1$ based on the applied loading condition. The other component

of the force is the interaction force from the fluid $\{f\}_t^{int}$ which is evaluated for time t. The stiffness matrix $\left[\hat{K}\right]$ is invariant in time. Iterative solvers are used to solve the system.

It should be noted that unlike other previous implementations of the coupled LBM-FEM (MacMeccan et. al [56], Sui et. al. [68]) techniques, here the complex nature of the porous geometry requires a different approach. In the previous implementations, FEM was used to model the deformation of individual particles in shear flow of suspensions. The relatively simple geometry of particles allowed for an approach where the effective stiffness matrix $\left[\hat{K}\right]$ could be constructed and inverted once at the start of the simulation. In subsequent timesteps, the matrix-vector product of the inverted stiffness matrix $\left[\hat{K}\right]^{-1}$ and the updated force vector $\left\{\hat{f}\right\}_{t+1}$ results in the displacement vector $\{u\}_{t+1}$. This computation is performed for each particle in the domain.

In the case of a porous media the geometry is more complex as shown in figure 22. Inverting and storing the effective stiffness matrix $\left[\hat{K}\right]$ is not feasible. Instead the developments in parallel iterative scheme should be used to solve the system of equations given in 39. Thus an approach where the geometry could be divided into smaller subdomains, followed by using parallel vector and matrix data structures to assemble the equations and using parallel iterative schemes to solve them would ideally suit this problem.

2.3 Fluid-Solid Coupling

The "link-bounce-back" boundary condition for momentum transfer between the fluid and solid phase in LBM framework has been validated and well established (Ladd [51], Aidun et al. [2], Ding & Aidun [27]). Here the "link-bounce-back" boundary condition applied along the boundary links as implemented in Macmeccan et al.[56] is used. The boundary links cross the surface of the solid boundary and have one end

in the fluid and the other in the solid region. The bounce back boundary conditions assumes the boundary to lie at the mid-point of a boundary link, hence boundary of the solid is captured in a discrete manner.

A ray-tracing algorithm (Moller and Trumbore [59]) is used to project rays from the lattice nodes along the lattice link directions onto the surface traiangles of the solid to determine intersection. The algorithm provides a fast way to identify links crossing the boundary surface.

The momentum transfered from the fluid to the solid along a single boundary link is given as

$$\delta \boldsymbol{p}_k = 2\boldsymbol{e}_k \left[f_k \left(\boldsymbol{x}, t_+ \right) + \rho \frac{w_k}{3} \boldsymbol{v_b} \cdot \boldsymbol{e}_k \right], \tag{42}$$

where $f_k \left(\boldsymbol{x}, t_+ \right)$ is the fluid distribution at $\boldsymbol{x}$ after the collision operation represented by t_+. $\boldsymbol{v_b}$ is the velocity of the boundary at the link, $\boldsymbol{e}_k$ is the direction along the boundary link. A simple linear interpolation scheme is used to transfer the momentum to the finite element nodes. The momentum $\delta \boldsymbol{p}_k$ is weighted according to the its distance from the point of intersection with the finite element surface to the finite element node as

$$W_j = \frac{d_j}{\sum_{j=1}^{3} d_j}, \tag{43}$$

where d_j is the distance from the point of intersection of the link with the finite element surface to the j^{th} finite element nodes.

The fluid distribution in the nodes connected by the boundary link is updated as

$$f_{k'} \left(\boldsymbol{x}, t+1 \right) = f_k \left(\boldsymbol{x}, t_+ \right) + \rho \frac{w_k}{3} \boldsymbol{v_b} \cdot \boldsymbol{e}_k, \tag{44}$$

where k' represents the direction opposite to k.

The presence of two different grids, i.e the lattice-Boltzmann grid for the fluid phase and the finite element grid of the solid phase introduces a parameter l_{fea} that

is defined as the ratio of average finite element edge length to the lattice Boltzmann grid spacing $\boldsymbol{e}_k$ (MecMaccan et al.[56]. Due to the linear interpolation of momemtum onto the finite element nodes, the length scale l_{fea} cannot be less than 1.0. In this work, $l_{fea} > 2$.

2.4 Contact Modeling

As the porous media deforms the pores shrink and various surfaces in the solid come in contact. In such a case it is necessary to model the contact mechanics that occur at the pore scale. The model should be able to capture the contact physics with sufficient accuracy and at the same time should be computationally light enough to solve the numerous contacts that occur during the deformation of a soft porous media. The traditional methods in solid mechanics to model contact such as the penalty method have high computational requirements due to the need to model the contact surfaces using different elements. In the case of porous media due to the enormous number of contacts occurring during deformation, such a method would make the computations unfeasible.

Ding and Aidun [27] developed a near contact model to simulate the interaction of smooth spherical particles based on lubrication forces for approaching spheres. MacMeccan et al [56] extended the model to simulate contact between finite element surfaces. They used short ranged link-wise force, the magnitude and direction of which depends on the gap between the contacting surfaces. An exponentially increasing repulsive force (Buxton et al [19]) is also added to the lubrication force to keep the particle surfaces from overlapping. In this work the near contact model as implemented by MacMeccan et al. [56] is used with modifications for use on porous geometries.

The magnitude and direction of the link-wise force is given as

$$\delta \boldsymbol{f}_k = \begin{cases} 0 & \text{if } g > g_c \ , \\ \frac{3q}{2c_k^2\lambda}\nu\rho\left(\frac{1}{g^2} - \frac{1}{c_k^2}\right)\boldsymbol{v_a}\cdot\boldsymbol{e_k} & g_c < g < c_k \ , \\ \frac{3q}{2c_k^2\lambda}\nu\rho\left(\frac{1}{g^2} - \frac{1}{c_k^2}\right)\boldsymbol{v_a}\cdot\boldsymbol{e_k} + A_c exp\left(\frac{-g+g_c}{\sigma_c}\right) & 0 < g < g_c \ , \end{cases} \tag{45}$$

where $\boldsymbol{v_a}$ is the approach velocity of the interacting surfaces, g is the link-wise gap between surfaces, g_c is the contant cutoff distance, λ is the local surface curvature and q is chosen to be 0.6 (Ding & Aidun [27]). The parameters g_c and σ_c are dependent on the surface roughness of the geometry and are chosen apriori. A_c is chosen such that the repulsive contact force scales appropriately with the applied stresses (σ) i.e. $A_c = \frac{\sigma}{a_o}$ where a_o is the contact area that varies with the applied stress. Based on the applied loading σ and a_o can be determined before hand.

The curvature λ is calculated as

$$\lambda = \frac{1}{N}\sum_{i=1}^{N}\left|\frac{d\boldsymbol{T_s}}{d\boldsymbol{s}}\right|, \tag{46}$$

where $\boldsymbol{T_s}$ is the tangent vector to the surface in direction of $\boldsymbol{s}$, and $\boldsymbol{s}$ is a vector connecting finite-element surface centroids. The summation is performed over all neighboring surfaces, with $N = 3$ for triangles.

The interaction force calculated in equation 45 is added to the surface nodes of the interacting surfaces along with the fluid force given in equation 42. Thus the total force acting on a link connecting approaching surfaces is

$$\boldsymbol{f}_k = \delta\boldsymbol{p}_k + \delta\boldsymbol{f}_k. \tag{47}$$

The force $\boldsymbol{f}_k$ is transfered to the surfaces nodes as mentioned earlier. Subsequently the force vector for time $t + 1$ is updated and solved.

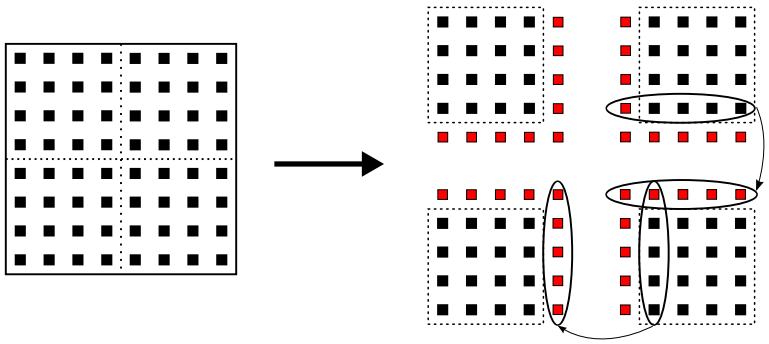

Figure 6: Decomposition of a 2D lattice-Boltzmann domain into 4 subdomains for parallel processing. The lattice nodes represented in red are ghost nodes. At each time step distribution from the real nodes of one subdomain are communicated to the ghost nodes of the adjacent subdomain as shown in the the figure.

2.5 LBM-FEM computations in Parallel

Direct numerical simulations demand high computational resources. In modeling saturated porous media, the fluid and solid phases are tightly coupled and need to be solved simultaneously. In addition the complex geoemtery of the porous media require high spatial and temporal resolution. This necessitates using distributed computing to obtain results in a realistic time frame.

The parallel algorithm used in this work uses separate ranks to perform fluid and solid calculations. The ranks used for fluid calculations are called "fluid ranks" and those used for solid calculations are called "solid ranks". The method and data structures used for parallelizing and communicating information within and across fluid and solid ranks are described below.

2.5.1 Parallelizing LBM

According to the Lattice-Boltzmann equation 29, the distribution $f_k(\boldsymbol{x}, t+1)$ at lattice node $\boldsymbol{x}$ and time $t+1$ is solely dependent on the distribution function at lattice $\boldsymbol{x} + \boldsymbol{e}_k$ and at time t. Such local nature of algorithm benefits from a data-parallelism approach.

Data-Parallelism is achieved by dividing the domain among the available ranks.

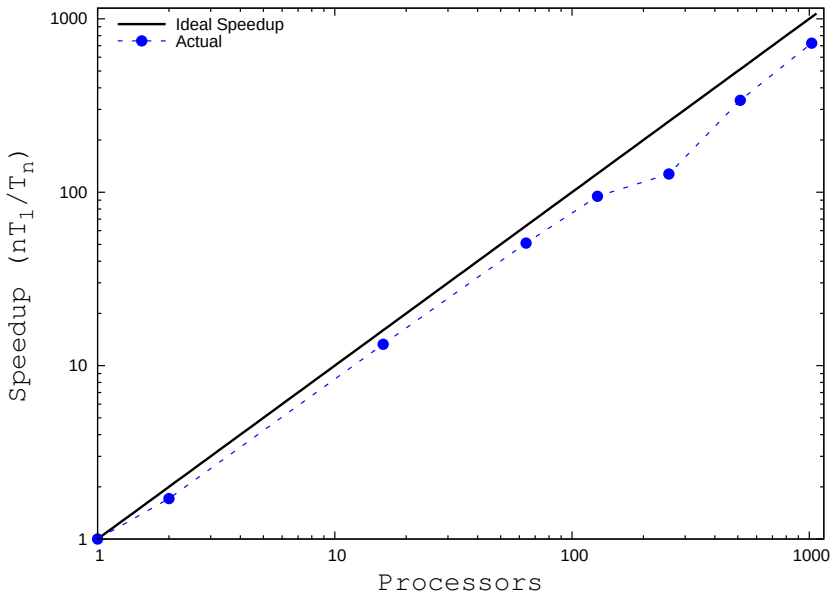

Figure 7: Weak scaling results of single phase LBM simulations.

As shown in Figure 6, upon division the of domain, an extra layer of cells also called "ghost cells", are added to each sub-domain. These ghost cells facilitate the transfer of information between adjacent sub-domains at every time-step, thus maintaining the continuity of entire domain. The simple nature of computations and low communication required leads to excellent scaling, that is needed for a complex problem of deformation of saturated porous media.

The communication is achieved using MPI (Message Passing Interface) an API that provides tools in the form of libraries which can be included in the users application for performing communication between processors. `MPI_Sendrecv` is used to transfer information of the ghost nodes to neighbouring ranks. Figure 7 shows the weak scaling results of the single phase LBM simulations. The problems being simulated is Poisuielle flow through a rectangular channel. In a weak scaling analysis the computational load on each rank is kept constant while the total ranks are scaled up to simulate larger problem. Thus the goal of a weak scaling analysis is to gauge how efficiently the method can scale the problem size while scaling the number of processors. This is in contrast to "strong scaling" where the goal is to gauge how efficiently

r

Table 2: Computational resources that were made use during this research work.

Resource	Type	Processors	Interconnect
Mercury	IBM cluster	$1.3/1.5GHz$ Intel It	Myrinet
Steele	Dell PowerEdge	$2.33GHz$ Intel Xeon	GigaBit Eth
Abe	Dell PowerEdge	$2.33GHz$ Quad Core	Infiniband
QueenBee	Dell PowerEdge	$2.33GHz$ Quad Core	Infiniband

the method solves a given problem size while the number of processors are increased. In the weak scaling analysis the computational load and the network communication per node are relatively the same, however in a strong scaling the computational load decreases and the network communication increases per processors as the number of processors are increased. For a weak scaling analysis the speedup $\mathcal{S}_n$ is calculated as

$$\mathcal{S}_n = \frac{nT_1}{T_n}, \tag{48}$$

where n is the number of ranks, T_1 is the simulation time for 1 rank and T_n is the simulation time for n ranks. The efficiency $\mathcal{E}_n$ of the method is given as

$$\mathcal{E}_n = \frac{\mathcal{S}_n}{n}, \tag{49}$$

where n is the ideal speedup.

In this test case, the domain size is increased from $64 \times 64 \times 64$ to $65536 \times 64 \times 64$ in multiples of 2, where the former domain size is run on a single rank and the later run on 1024 rank. The simulation were run on Mercury, an IBM cluster at National Center of Supercomputing Applications (please refer table 2). As can be seen in the plot LBM performs very well in the weak scaling analysis. For 1024 processors the speedup is 723.8 which translates to an efficiency of 70.7%

2.5.2 Parallelizing FEM

Typically parallelizing a finite element method follows the data parallelism approach (Kwon [50], Liu et al [55]). Here the elements in the domain are divided amoung the available ranks as shown in figure 8. This kind of partitioning creates ghost nodes as shown in the figure, although there are no overlapping or ghost elements.

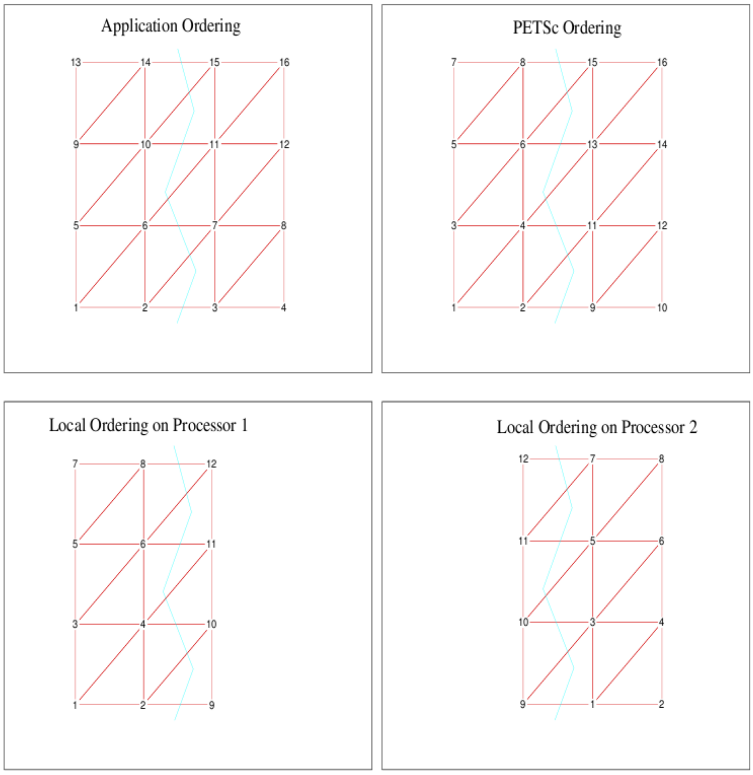

Figure 8: Mesh partitioning and subsequent PETSc and application ordering of finite element nodes.

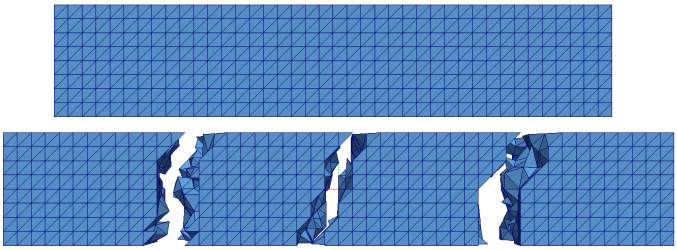

Figure 9: Decomposition of unstructured finite element mesh of a rectangular beam into four subdomains using K-way graph partitioning algorithm provided by PARMETIS

It is important to note here that unlike LBM, computations in FEM are not local in nature. Since at each time step a system of equations is solved, each degree of freedom (DOF) indirectly effects all the other DOFs. More particularly, the effect of a DOF on the rest of the DOFs is determined by connectivity. When a geometry is divided as shown in figure 8, in order to maintain the connectivity across the partitioning line, ghost cells are created. If a rank owns a set of ghost nodes the at each time step information regarding the ghost node needs to be communicated to the ranks that own them. In the present implementation Newmark's scheme is used for time integration, which requires several matrix-vector operation for each timestep. This results in several `MPI_Sendrecv`'s per timestep per ghost node, which is quite different from LBM where only one `MPI_Sendrecv` is required per timestep. Thus it becomes critical to reduce the ghost nodes which in turn implies reducing the partitioned surface area. This is "Graph partitioning" problem. In this work, the K-way graph partitioning algorithm provided by the graph partitioning tool PARMETIS (Karypis and Kumar [42]) is used to solve the graph partitioning problem and thus perform optimal partitioning of the finite element mesh. Figure 9 shows the result of using PARMETIS for partitioning the finite element mesh of a rectangular beam.

Subsequently parallel vector data structure is used to setup the displacement and force vectors while the sparse parallel matrix structure is used to setup up the combined stiffness matrix. The resulting parallel system of equations are solved using

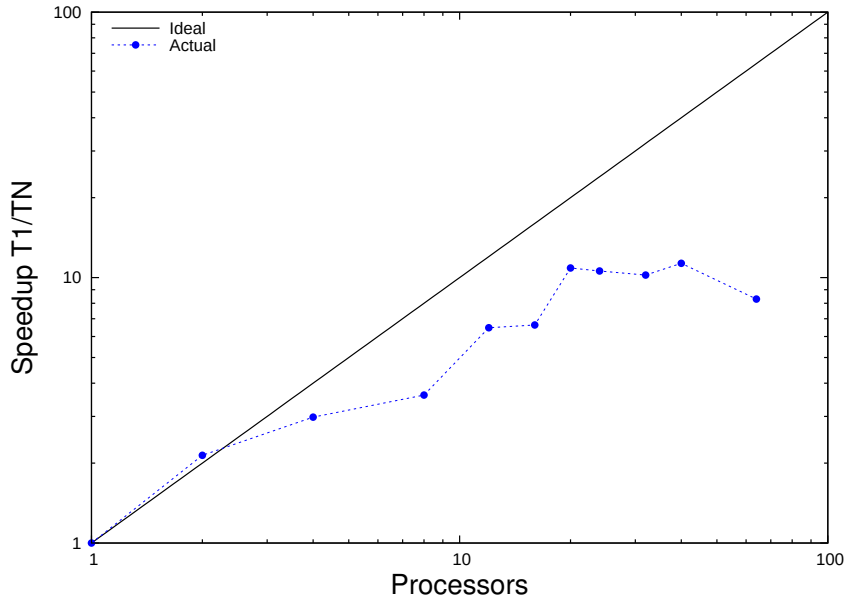

Figure 10: Strong scaling of the single phase finite element method. Test problem is cantilever beam with 1106730 degrees of freedom.

Krylov subspace methods. The libraries provided in the Portable, Extensible Toolkit for Scientific Computations (PETSc [64]) allow for convenient a way of setting up the data structures for parallel vector and matrix computations and also to choose from a variety of parallel iterative solvers.

Figure 10 shows the strong scaling results of the single phase solid deformation simulations using the parallel finite element method. The speedup in strong scaling is defined as

$$\mathcal{S}_n = \frac{T_1}{T_n}. \tag{50}$$

The test problem is a cantilever beam deflection with 1106730 degrees of freedom. The simulations where run on Steele cluster, a Dell PowerEdge machine at Purdue (2). 1106730 DOFs is a small number to see significant scaling capabilities. However the plot shows the ability of the code to scale as the computational resources are increased. A maximum efficiency of 60.4% is achieved on 32 ranks. The maximum speedup achieved is 19.98 on 36 ranks. Beyond 36 ranks the communication overhead outweights the reduction in computational time.

2.5.3 Parallelizing coupled LBM-FEM

As mentioned earlier, optimal mesh partitioniong is very critical for the efficiency and scalability of the FEM. As such a graph partitioning algorithm is used to partition the FE mesh as opposed to a cartisian coordinates based partitioning as implemented in the LBM. Because of the differences in the partitioning procedure it is convenient to use seperate ranks for the LBM calculations and seperate ranks for FEM calculations. Thus different MPI communicators are used for fluid ranks (`LBM_Comm`) and solid ranks (`FEA_Comm`).

However, at each timestep fluid force information needs to be communicated from the fluid ranks to the solid ranks and displacement and velocity information needs to be communicated from the solid ranks to the fluid ransk. Because the fluid and solid information is scattered over a number of different rank suitable data structures need to used to keep track of the send and receive destinations. We use the parallel vector data structures provided through PETSc. These communications have be done with the global communicator (`MPI_COMM_WORLD`).

Figure 11 shows the flow chart represenation of the algorithm used in the LBM-FEM code to perform coupled calculations in the fluid and solid phases. Notice that seperate MPI communicators are used to fluid phase calculations and solid phase calculations. In order to transfer fluid-structure interaction data the fluid ranks and solid ranks communicate through the global communicator.

Figure 12 shows the strong scaling results of the coupled LBM-FEM simulations. The test problems used is a compression of model saturated porous media made up of spheres in a simple cubic arrangement. The problem is described in chapter 4. Two test cases are used here; one with 128 spheres (313908 DOFs)in the domain and the other with 256 spheres (628545 DOFs). The LBM domain size is $5120 \times 41 \times 41$ for the first case and $10240 \times 41 \times 41$ for the second case. The simple cubic arrangement lead to a volume fraction of 0.39. The geometry setup allows for using equal number

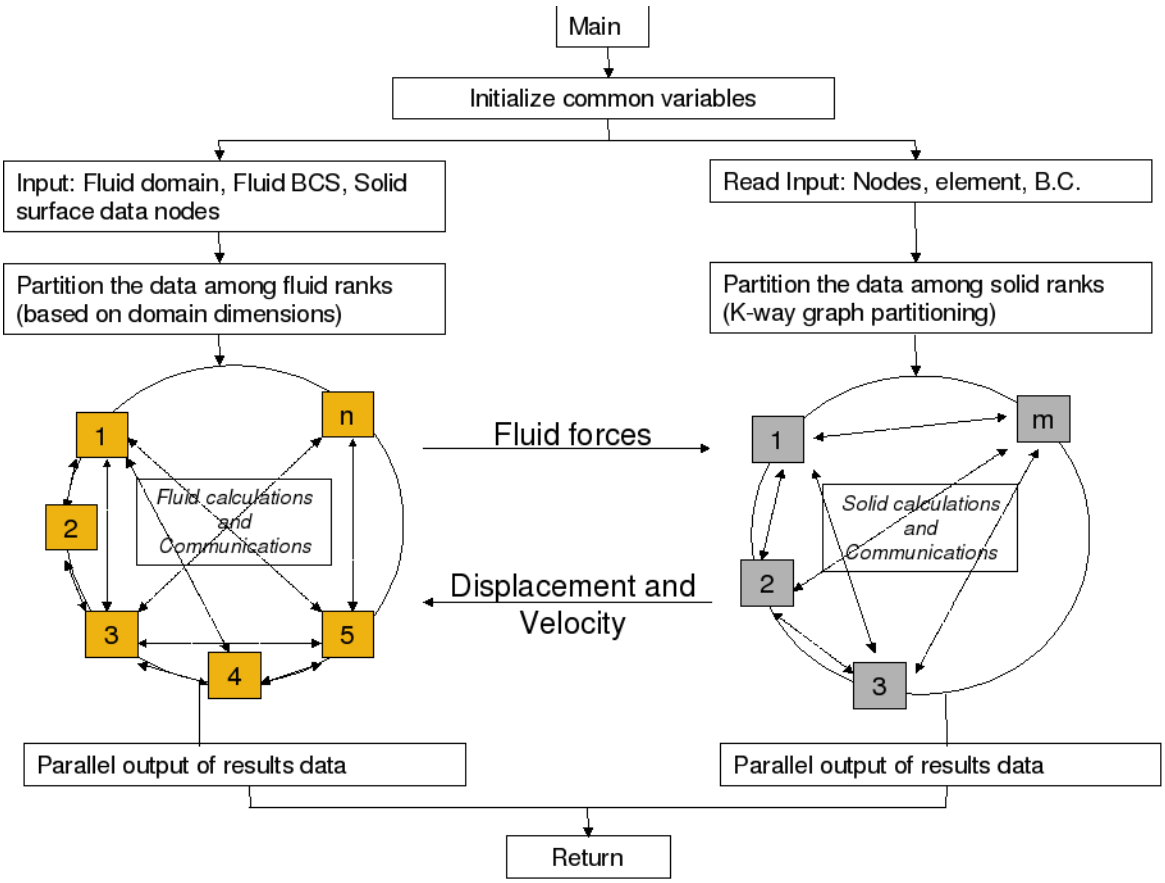

Figure 11: Flow chart representation of the algorithm used in the LBM-FEM code to perform coupled calculations in the fluid and solid phases.

of ranks for the fluid and the solid calculations. Thus when 32 ranks were used to simulate the problem, 16 ranks were used for the LBM calculations and 16 ranks were used for the FEA calculations.

For the 128 sphere case the plot shows good scaling till 256 ranks. When using 256 ranks for this problem, 128 ranks are used for the fluid and 128 are used for the solid phase. Thus each solid rank performs computations of one sphere. Since there is no connectivity between the nodes of two different spheres, there is no ghost node and thus no communication required for this division. Thus this can be considered as an ideal geometry setup and ideal division. The efficiency for this case is 83.6%. However, when the ranks are increased further, the speedup decreases and the efficiency reduces to 67.1%. This is because, now 256 ranks share 128 spheres, thus each is split into two ranks. This create a lot of ghost nodes resulting in a lot of communication overhead.

A similar trend is seen in with the 256 sphere simulations. When 512 ranks are used the 256 spheres are divided amoung 256 ranks, which results in no ghost nodes and thus minimal communication with the solid ranks. This leads to an efficiency of 71.8% on 512 ranks. But when the ranks are incrased to 1024, the efficiency reduces to 12.1%.

This shows that the FEA calculations are the bottleneck in the LBM-FEM code. And reducing the partitioned surface area or the ghost nodes during the mesh partitioning leads to significant gains in the efficiency of the code.

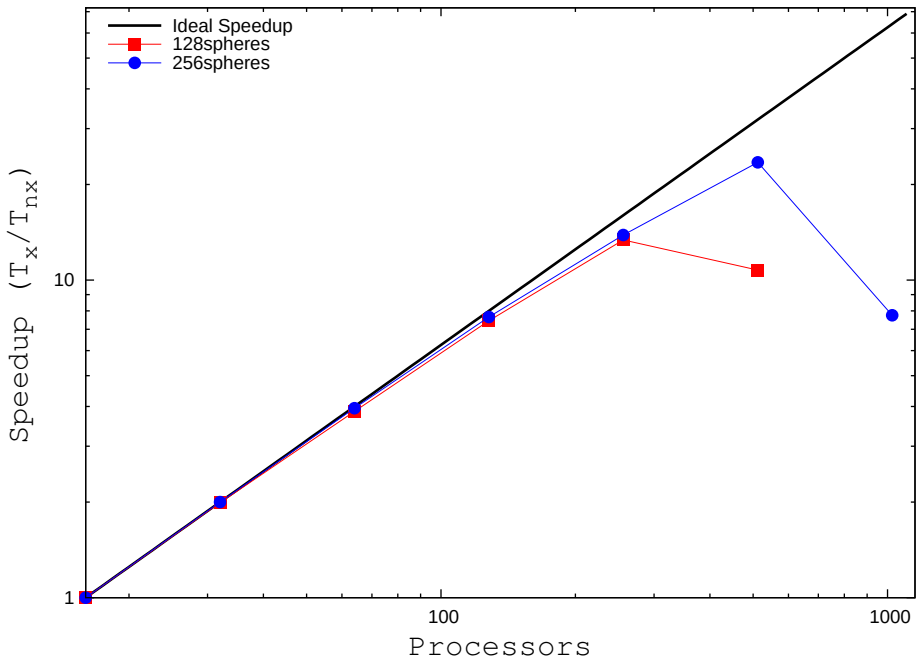

Figure 12: Strong scaling results of the parallel coupled LBM-FEM code. The test problems used for testing speedup are described in chapter 4.

CHAPTER III

VALIDATION OF METHOD

The method has been validated against experimental and analytical data for capability in modeling fluid-structure interaction in complex geometries such as a porous media. The problem of settling of sphere in a channel with rectangular cross-section was chosen to test the fluid-structure interaction modeling. In order to test the capability of code to model flow in complex geometries, the problem of flow through a regular arrangement of spheres was chosen. The parallel transient finite element implementation was tested by comparing the wave propagation speed in a rectangular cantilever beam. Finally the near contact modeling was tested by comparing against the Hertz contact model for deformation of two spheres under compression.

3.1 Sphere settling in a rectangular channel

The effect of walls on the settling of a single solid sphere in a rectangular channel has been studied experimentally by Miyamura et al [58]. They obtained the wall correction factor F_w for spheres of different relative radii $r*$. The wall correction factor provides the effect of wall on the settling velocity of a particle and is given as

$$F_w = \frac{v_w}{v_f}, \tag{51}$$

where v_w is the sphere steady state settling velocity in a channel and v_f is the steady state settling velocity in a free stream. The relative radii is given as $r* = \frac{r}{L}$, where r is the radius of the sphere and L is the edge length of the channel as shown in figure 13.

The above problem of sphere settling in a channel is used as a model problem.

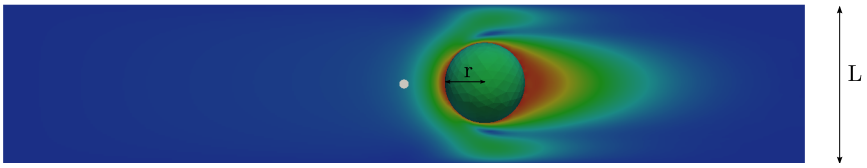

Figure 13: Hindered settling of single solid sphere of radius r in a channel with square cross section of lenght L

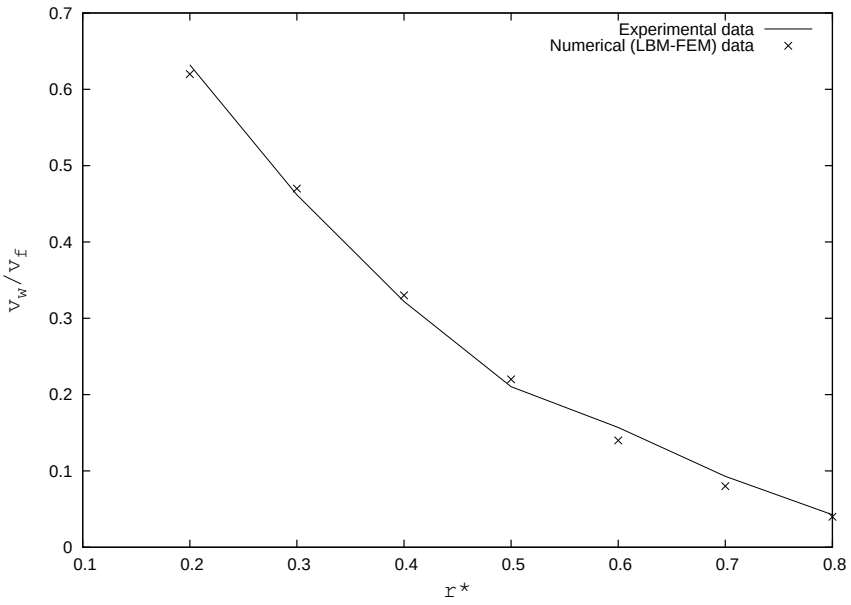

Figure 14: Comparsion of LBM-FEM method with experimental data for hindered settling of spherical particle in a channel with square cross-section. r^* is the effective radius of the sphere, v_w is the hindered settling velocity of the sphere and v_f is the settling velocity in a free stream.

Aidun et al [2] found good agreement between the lattice Boltzmann simulation of settling of a smooth sphere and the experimental data provided by Miyamura et al. Here the simulations are extended to discretized finite-element spheres that are solved in a parallel framework.

The boundary conditions are set to bounce-back on the four wall with zero velocity at the inlet (left) and stress-free at the outlet (right). The sphere is given a high value of Young's Modulus to mimic a rigid sphere. At the start of the simulation a body force is applied to the sphere and with time allowed to reach a steady state velocity v_w. The length of channel was set to 400 lattice units and the channel width and

height were varied to vary $r*$ from 0.2 to 0.8. The diameter of the sphere was kept constant ($= 40 lattice units$) in all the cases.

Figure 14 shows the comparison of the LBM-FEM method with the experimental data. The decrease in the settling velocity due to the presence of the wall as predicted by the numerical simulations matches that with the experimentally developed correlation. Thus it is seen that the implemented Standard Bounce-Back (SBB) method for modeling the interaction of fluid and solid phase provides an accurate measure of the forces generated during of interaction of both the phases.

In these simulations the value of parameter l_{fea} is set to 4. However, MacMeccan et. al. have shown that $l_{fea} = 2$ also gives equal accurate results.

3.2 Pressure drop across an array of spheres

Analytical models have been proposed (Bird et al.[13]) to describe the pressure drop across an array of spheres based on modeling the porous media as a bundle of capillary tubes. However such models underestimate the pressure drop because they do not take into account the energy dissipation in elongation and contraction of fluid elements.

In order to understand flow through porous media Durst et al [28] performed experimental investigations of flow through an array of spheres. The empirical relationship, obtained by Durst et al. [28], between pressure drop and fluid velocity for flow through spheres is given as

$$\Omega = 182 + 1.75Re, \tag{52}$$

where Ω is friction factor given as $\frac{\Delta P}{\Delta L}\frac{D_p}{\rho {U_0}^2}\frac{\epsilon^3}{(1-\epsilon)}Re$ and Re is Reynolds number given as $\frac{U_0 D_p \rho}{\mu^F(1-\epsilon)}$, where D_p is the diameter of spheres, $\frac{\Delta P}{\Delta L}$ is the pressure drop, U_0 is the average velocity, ϵ is the porosity, ρ and μ^F are the density and viscosity of the fluid respectively.

In order to validate the LBM-FEM method to model flow through porous media

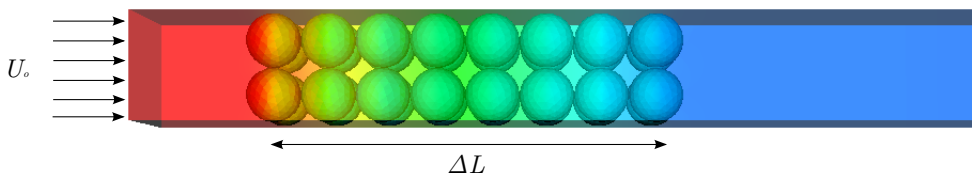

Figure 15: The geometry used to validate Lattice Boltzmann method to model flow through porous media. The porous media is represented by regular arrangement of spheres. At the inlet (left) a constant velocity U_o is applied and at the outlet (right) stress-free boundary condition is applied. A periodic boundary condition is applied on the rest of the four walls. The pressure drop across the length ΔL is measured.

we have used the above mentioned experimental results of flow through spheres to compare. The geometry of spheres used in the LBM-FEM validation is as shown in figure 15. Due to the approximation of the sphere geometry using finite elements the porosity of the arrangement varies such that $0.49 < \epsilon < 0.51$.

The boundary conditions are periodic along the four walls with a constant uniform velocity profile at the inlet and a stress free or outlet flow boundary condition at the outlet. For a given porosity ϵ the Reynolds number $Re = \frac{U_0 D_p \rho}{\mu^F (1-\epsilon)}$ can be changed by changing the inlet average velocity U_0 or the particle diameter D_p. Since the velocity in lattice Boltzmann simulations is limited by the mach number $c_s = \frac{1}{\sqrt{3}}$, simulations of high Reynolds number are achieved by increasing the sphere diameter. In lattice units the diameter of particles chosen in these simulations are 40, 80, 160 and 320. The minimum particle diameter chosen is twice what Bernsdorf et al. [3] showed to be sufficient for obtaining results within 3% of experimental value in similar simulations of flows through spheres.

Figure 16 shows the comparison of LBM-FEM method with experimental data for pressure drop in flow through an array of spheres. As can be seen the results of LBM-FEM method match closely with experimental correlation developed by Durst et al. The value of the friction coefficit Ω is found to be very sensitive to the volume of spheres V_s through the variable ϵ. In the current simulations the geometry of the sphere is described by triangular surface elements. Such a representation introduces

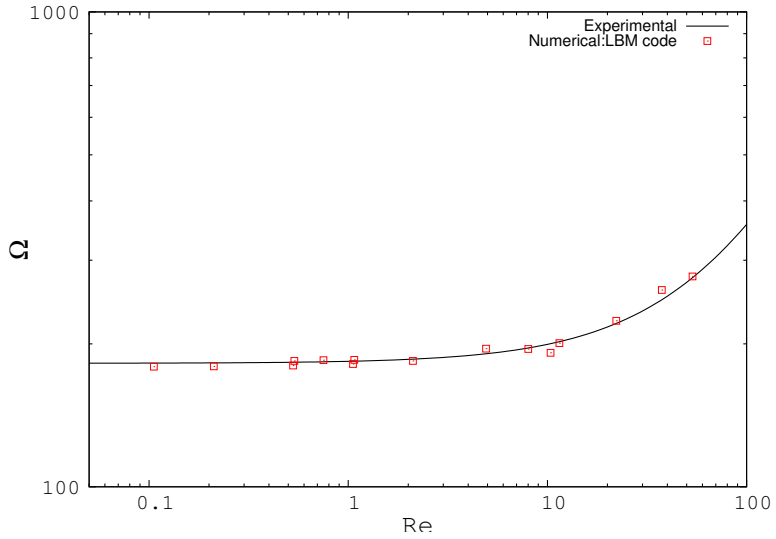

Figure 16: Comparison of LBM-FEM method with experimental data for pressure drop in flow through an array of spheres. Ω is friction factor given as $\frac{\Delta P}{\Delta L}\frac{D_p}{\rho {U_0}^2}\frac{\epsilon^3}{(1-\epsilon)}Re$ and Re is Reynolds number given as $\frac{U_0 D_p \rho}{\mu^F(1-\epsilon)}$, where D_p is the diameter of spheres, $\frac{\Delta P}{\Delta L}$ is the pressure drop, U_0 is the average velocity, ϵ is the porosity, ρ and μ^F are the density and viscosity of the fluid respectively.

uncertinity in the exact location of boundary for the application of "bounce-back" scheme. Thus there are some difference between the volume of the finite element meshed geometry of spheres and the lattice Boltzann volume of spheres, which may attritube to the slight difference between the numerical simulation results and the experimentally obtained empirical data.

The results shown above validates the use of "link-bounce-back" boundary condition to model no-slip condition on the walls of solid geometry. The use of this boundary condition has accurately predicted the energy losses due to both shear as well as elongations and contraction of fluid elements.

3.3 Cantilever beam deflection

$$\delta(y=0) = \frac{Px^3}{6EI} + \frac{Pl^2x}{2EI} + \frac{Pl^3}{3EI} \tag{53}$$

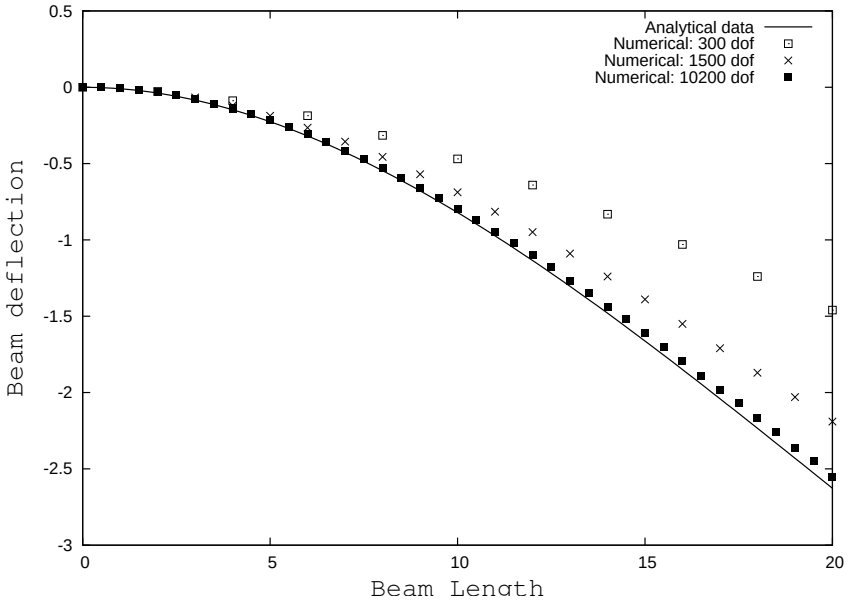

Figure 17: Comparison of deflection $\delta(y = 0)$ obtained from a static FE analysis with the analytical deflection given in equation 53. The lines represent the analytical data and the points represent data from FE simulations. The abscissa represents the length along the axis of the cantilever beam.

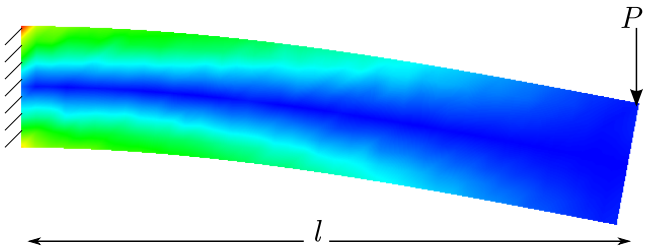

Figure 18: Deflection of a Cantilever beam of length l under an applied load P at the beam edge. The color represents the stress variation inside the beam.

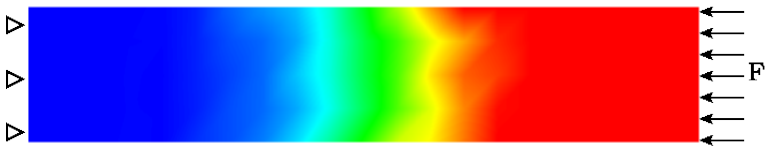

Figure 19: Wave propagation in a rectangular beam. The beam is fixed at the left and is applied a compressive load on the right end. The color represents the stress distribution in the beam

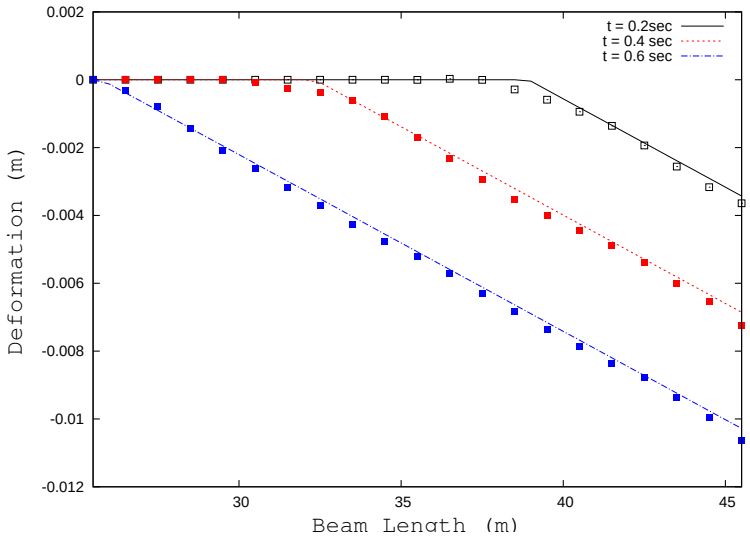

Figure 20: Comparison of deflection $u(x,t)$ obtained from FE analysis with the analytical deflection given in equation 54. The lines represent the analytical data and the points represent data from FE simulations. The abscissa represents the length along the axis of the cantilever beam.

3.4 Wave propagation in a beam

In order to test the transient finite element implementations for accurately modeling time-dependent response of solid, the method was tested against the problem of wave-propagation in a beam. A compressive load $F(t)$ is applied to a rectangular cantilever beam as shown in figure 19. In this case the load is a step function that remains constant after time $t = 0$. No mass or stiffness damping is used, so as to capture all the modes during the wave propagation. The element edge length was chosen to be equal to $\frac{\omega}{\delta t}$, where ω is the wave speed and δt is the timestep. The deformation response $u\,(x,t)$ for this problem is given as

$$u\,(x,t) = \begin{cases} 0 & \text{if } x < \omega t\ , \\ \frac{F(x-\omega t)}{EA} & \text{if } x > \omega t\ , \end{cases} \tag{54}$$

where F is the applied compressive load, E is the Young's modulus, A is the cross-section area. Figure 20 shows the comparsion of the numerical results with the above equation. As can be seen the wave propagation speed is accurately predicted

by the finite element method.

3.5 Validation of Contact Model

The contact model has been tested by analysing the deformation when two frictionless bodies are brought into contact under an external force. Hertz solved the problem within elastic limit [70]. The analytical expression for the relative displacement (α) of the centers of two elastic bodies with convex surfaces compared to their non-deformed configuration is given as

$$\alpha = \left[\frac{9P\left(1-\nu^2\right)}{8R^*E^2}\right]^{\frac{1}{3}}, \tag{55}$$

where P is the applied load, E is the Young's modulus and ν is the Poisson ratio. $\frac{1}{R^*}$ is equal to $\frac{4}{R}$ for spheres and $\frac{2}{R}$ for cylinders; R being the radius of curvature of the convex surface.

The geometries used in this study are shown in figure 21. In figure 21a two spheres of equal radii R are alinged along the x-axis and a compressive load P is applied. The diameter of the spheres was chosen to be 40 lattice units, which allows for resolving the transfer of fluid-structure interaction forces accurately ([56]). Two different mesh resolutions were used to discretize the geometry of spheres. The finite element edge length of the coarse mesh is approximately 4 lattice units which leads to approximately 10 elements across the diameter of the sphere. The fine mesh has twice the resolution of the coarse mesh, thus it has 20 elements across the diameter of the sphere. In this study, since the contact parameter A_c scales with the applied stress load $\sigma = \frac{P}{\Pi R^2}$, the value of A_c increases as the load P is increased.

Figure 21c shows the comparison of non-dimensional deformation α/R between the implemented contact model in LBM-FEM with Hertz's contact model. As can be seen, the predicted deformation matches well with the analytical model, particularly near small deformation ($\frac{\alpha}{R} < 0.04$). The mesh resolution does not have a major effect

on deformation when $\frac{\alpha}{R} < 0.04$. However for $\frac{\alpha}{R} >= 0.04$ the fine mesh gives better results for the predicted deformation. Further, the simulation results deviate from the analytical model as the deformation increases. This deviation, also seen in finely meshed spheres, is mainly due to lack of enough mesh resolution. However it is also well known that for finite deformations Hertz's model over-predicts the value of α [29].

Figure 21b shows the second geometry used to test the contact model. Two cylinders of radii R and orthogonally aligned axis, are brought into contact under a compressive force P. The diamter of the cylinders was chosen to be 40 lattice units to match those of the spheres. As in the case of spheres, two mesh resolutions were tested. The coarse mesh has 10 elements across the diameter, while the fine mesh has 20 elements across the diameter of the cylinder. Figure 21d shows the comparison with Hertz's contact model. A similar behaviour as in the case of spheres. There is good match with the Hertz model for $\frac{\alpha}{R} < 0.04$ and here the coarse and fine mesh results do not differ a lot. The results deviate from the Hertz model as $\frac{\alpha}{R} >= 0.04$ and here the fine mesh gives better results for predicted deformation.

3.6 Sample Simulation

The versatility, robustness and efficiency of the method is demonstrated through the simulation of a model saturated porous media. The porous media used in this simulation consists of a regular arrangement of spheres as shown in figure 22(a). The diameter of the spheres is 40 lattice units. The element size chosen to discretize the spheres in space is given by $l_{fea} = 4$, which is same as the coarse mesh chosen in the validation of contact model. Due to the approximation of the sphere geometry using finite elements the porosity (ϵ) is slightly lower than the porosity for a Body-Centered-Cubic (BCC) arrangement ($\epsilon \approx 0.49$). The non-dimensional parameter ρ^*, which represents the ratio of solid density (ρ_s) to the fluid density (ρ_f) is chosen to

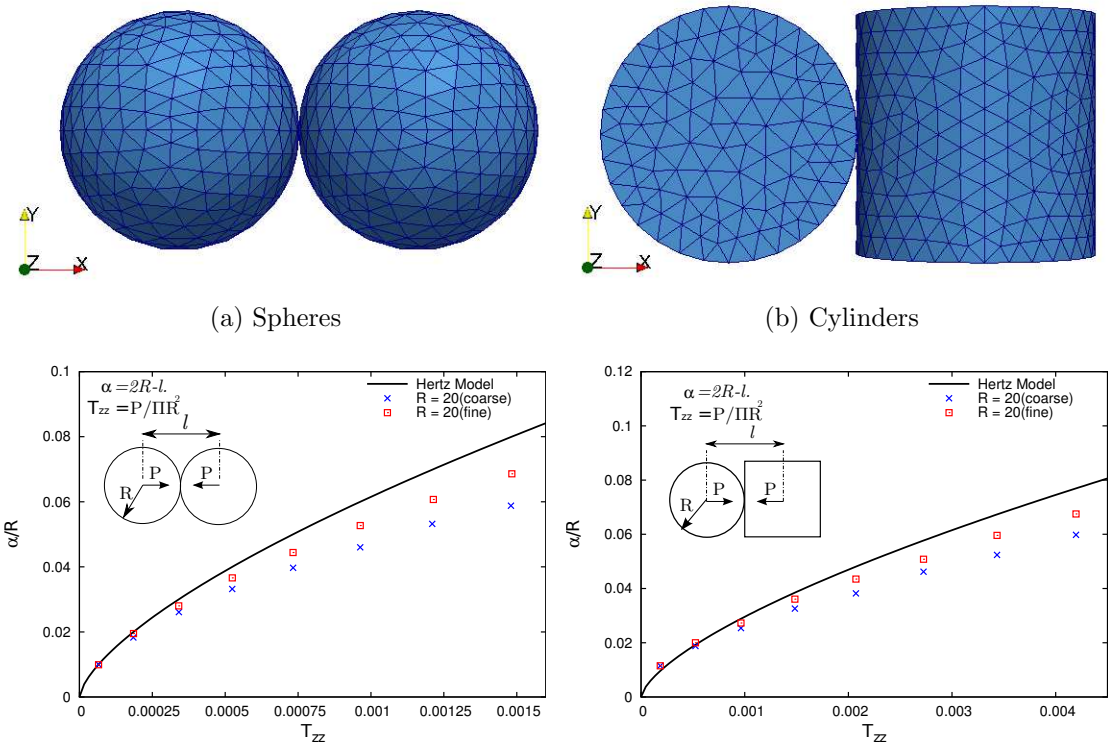

(a) Spheres

(b) Cylinders

(c) Contact of spheres

(d) Contact of cylinders

Figure 21: Comparison of the Hertz contact model with the near contact model implemented in LBM-FEM method. α represents the deformation due to the compressive load P and R is the radius of the spheres and cylinders. The solid line represents the analytical model by Hertz and the points represent the LBM-FEM simulation results using coarse mesh ($\times$) and fine mesh ($\boxdot$.

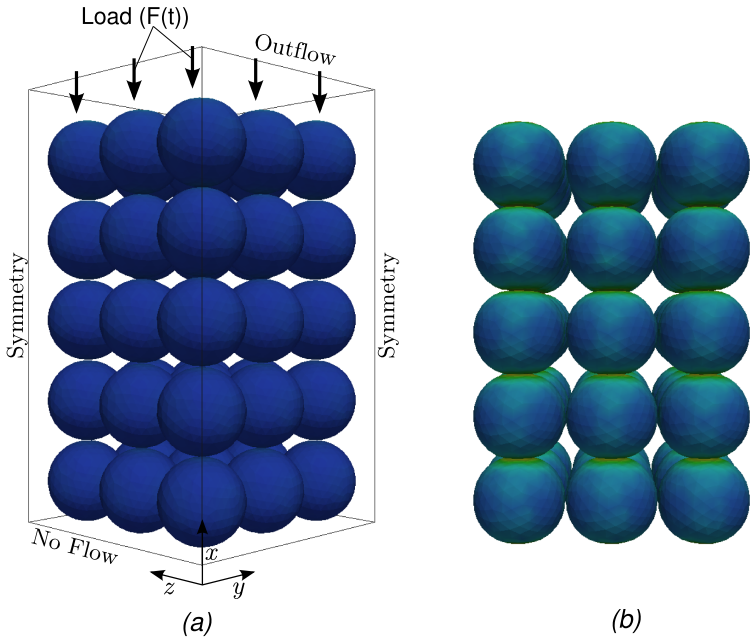

Figure 22: (a) Model saturated porous media made up of regular arrangement of spheres. Also shown are boundary conditions for the fluid and the loading direction for the solid phase. (b) The configuration of the porous media at steady state. The color represents strain.

be 2.0. Further the non-dimensional parameter E^* given as

$$E^* = \frac{ER^2\rho_s}{(\mu^F)^2} \tag{56}$$

(where E_s represents the Young's modulus of the solid, R is the radius of the spheres and μ^F is the dynamic viscosity of the fluid), is chosen to be $2.35E+04$.

The boundary conditions for the problem are also shown in figure 22-a. For fluid, a symmetry boundary condition is applied along the $x-y$ and $x-z$ sides of the domain. At the top, an outflow or stress-free boundary condition is applied and at the bottom a no-flow boundary is applied. For the solid phase, the nodes near the $x-y$ and $x-z$ walls are constrained to move only in the vertical direction. The nodes at the bottom are constrained to not allow any movement in vertical direction. Further a time-dependent load ($F(t)$) is applied on nodes at the top. In this problem, the Heavyside function is chosen to be the time-dependent load, such that when

$t > 0; F(t) = P$.

The chosen finite element (FE) and lattice-Boltzmann (LB) meshing resulting in a total of 108K FE-degrees of freedome(DOFs) and $57,000 KLB - DOFs$. The problem was run on a single node of a Dell Power Edge 1950 cluster (Steele: Purdue) with each node containing two Quad-core Intel Xeon $2.33 GHz$ processors and $16 GB$ of memory. Five core were used for the fluid phase and three for the solid phase. The problem was run for 15,000 LBM timesteps to reach steady state. The resulting deformed porous media is shown in figure 22(b), where the color represents strain.

Figure 23 shows the average displacement experienced by the nodes at the top of the arrangement with time. The diplacement has been normalized using the radius of the spheres R. Time has been non-dimensionalized as $t^* = \frac{t\nu}{R^2}$, where ν is the kinematic viscosity of the fluid. The displacement shows a rapid non-linear behaviour initially but reaches a steady state value with time. Further investigations are needed to corroborate the method with established models [25].

Figure 24 shows the variation of pore pressure at $x = 3R$ with time. Pressure has been normalized as $P^* = \frac{PR}{\mu^F U}$, where μ^F is the dynamic viscosity of the fluid, and U is the average velocity of the solid phase. As expected, the pressure increases rapdily initally because of the compression process and with time reduces to zero. The fluctuation seen in the plot are a consequence of the weakly compressible nature of LBM.

3.6.0.1 Explanation of pressure fluctuations

These fluctuations are caused due to a combination of the compressible nature of LBM and the imposed BCs. The compressible nature of LBM with the discrete representation of the solid surface causes small fluctuations in the fluid density as the solid moves. The time scale of these fluctuations are small and their magnitude increases with increasing velocity of solid surface.

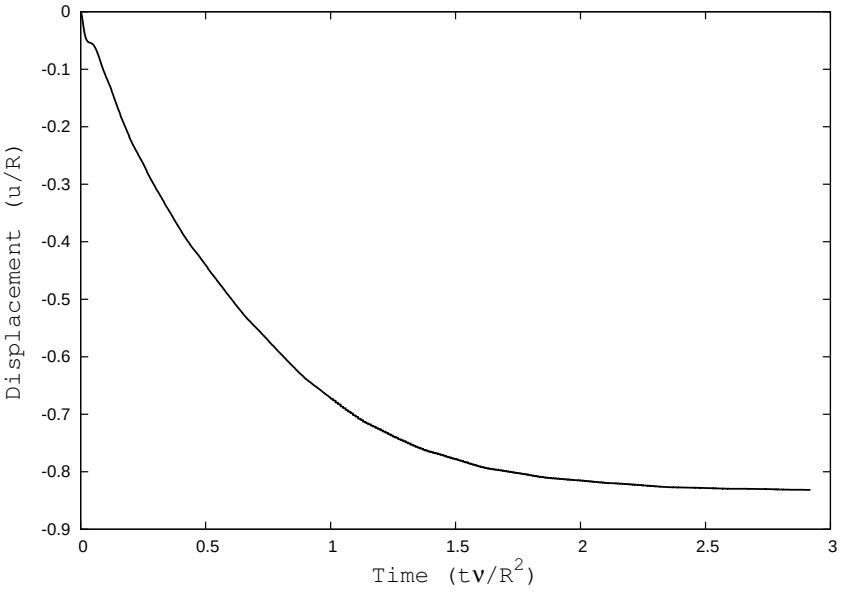

Figure 23: Average normalized displacement w.r.t time.

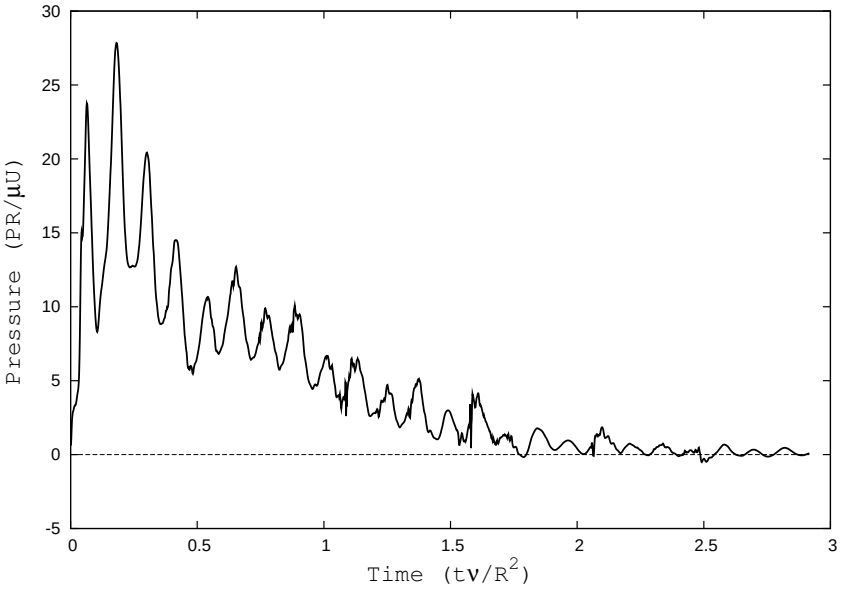

Figure 24: Average Pore Pressure w.r.t time ($x = 3R$).

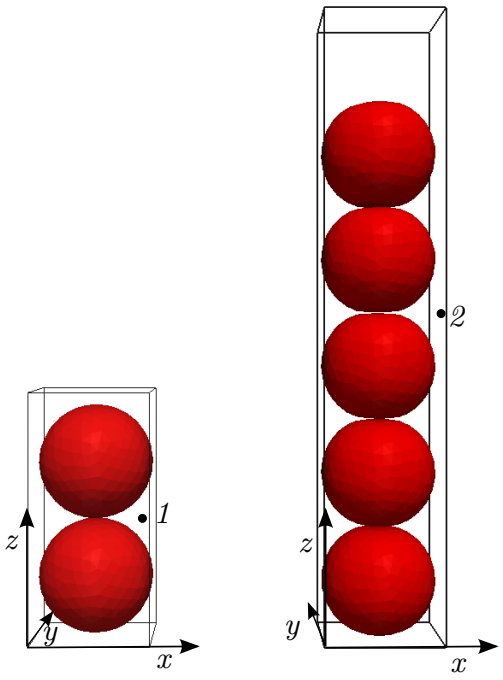

Figure 25: Two different geometris of two spheres and five spheres used to understand the pressure fluctuations.

However, when these small fluctuations propagate to the other end of the domain ($z = 0$)and get reflected back, they again interact with the generated fluctuations. The interaction of these two waves causes a peak in the density and thus in the fluid pressure value. As these fluctuations pass each other there is a wake respresented by a low pressure region.

To illustrate this we look at the pressure response in two geometries as shown in figure 25. In the case of 2sphere goemetry the average pressure at $z = 40$ lbm units is plotted and in the case of five spheres goemetry the average pressure at $z = 120$ is plotted. Figure 26 shows the variation of pressure with time at the chosen location in both the geometries under the influence of an applied instantaneous load.

The speed of sound in LBM is given as $c_s = \frac{1}{\sqrt{3}} = 0.5773$. Assuming that these shock waves are generated at the boundary of all the solid spheres, we see that the

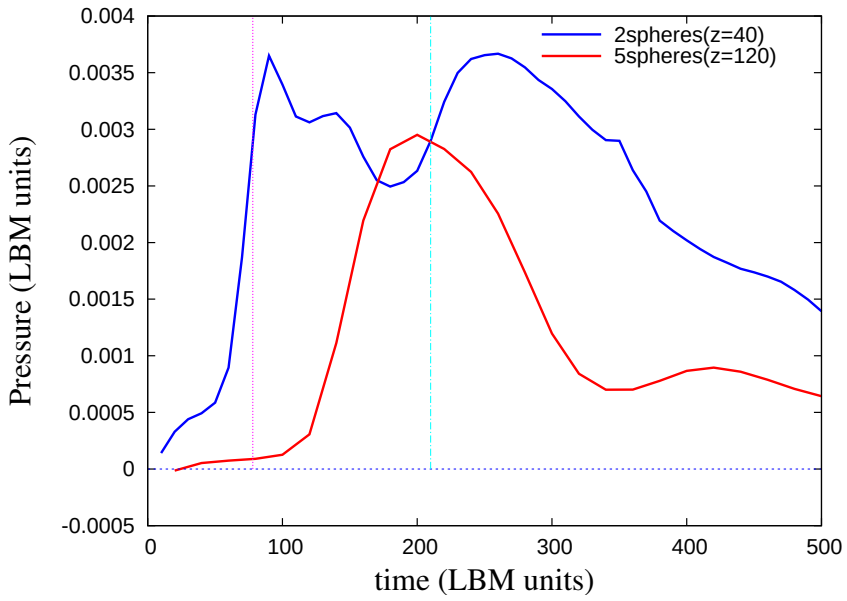

Figure 26: Variation of pressure with time in two geometries. 2 sphere geometry at z=40, 5 sphere geometry at z=120 LBM units.

quickest reflected wave to reach the locations $z = 40$ or $z = 120$ is generated at the bottom of the domain. Thus the wave reaches $z = 40$ at $z/c_s = 70$ time units in the case of 2 spheres and $z/c_s = 210$ time units in the case of 5 spheres goemetry. As seen from the plots the peak of pressure is also located around $t = 70$ and $t = 200$ time units in both the cases.

It should be noted that LBM is a weakly compressible scheme and in the small time scale does not reproduce accurate pressure behaviour. Only in the long time scale does it recover the Navier-Stokes equations. As can be seen from figure 24 as the simulation time increases there pressure fluctuations reduce.

CHAPTER IV

MACROSCOPIC BEHAVIOUR OF MODEL POROUS MEDIA

In the following the LBM-FEM method has been used to investigate the deformational behaviour of saturated porous media. Model porous media made up of spheres and cylinders in regular arrangements have been used for the study. Model porous media developed through the regular arrangement of simplified geometries allow for leveraging symmetry properties in the geometry apart from simplying the processing of generating effective meshes.

In this study, the model porous media is subjected to a compressive load as described in section 1.1.2.1. The deformational characteristics of the media are studied in time. For the comparison, the bulk properties of the macroscopic porous media are obtained through the single phase properties of the constituents.

4.1 Behaviour of Simple Cubic Granular Porous Media

The problem of instantaneous compression of a semi-infinite medium as discussed above is duplicated using a model porous media. The porous media is approximated using uniform spheres in a simple cubic (SC) arrangement. In such an arrangement the geometric symmetry can be used to simplify the simulation geometry. Thus, a column of spheres arranged vertically as shown in figure 27 is used to represent the granular SC arrangement. The column of spheres are submerged in fluid, thus representing a saturated porous media.

The boundary condition at the bottom ($z = 0$) is a no-slip, no-displacement

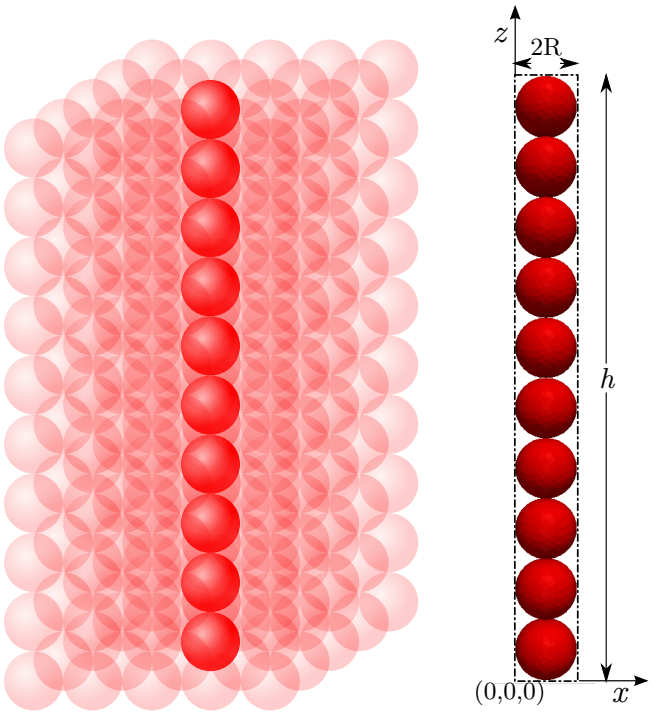

Figure 27: 10 spheres stacked vertically in a column of fluid, representing a simple cubic arrangement. The dotted line represents the simulation domain.

condition given as

$$\mathbf{v} = 0; u_z = 0; at\ z = 0; \tag{57}$$

where $\mathbf{v}$ is the fluid velocity vector, $\mathbf{u}$ is solid displacement vector. At the top, an outflow condition is applied on the fluid phase, and a load $f(t)$ is applied on the solid phase; given as,

$$\frac{\partial v_x}{\partial z} = \frac{\partial v_y}{\partial z} = \frac{\partial v_z}{\partial z} = 0; \mathbf{F}(t) = -f(t)\hat{k};\ at\ z = h, \tag{58}$$

where $\mathbf{F}(t)$ is the load vector and h is the height of the column. In this paper we only discuss the response of using a constant load with time. On the four vertical wall, symmetry conditions are applied, given as

$$v_x = 0; u_x = 0; at\ x = 0, 2R; \tag{59}$$

$$v_y = 0; u_y = 0; at\ y = 0, 2R; \tag{60}$$

where $2R$ is the diameter of the sphere and width of the domain in x and y directions.

The initial conditions are given as

$$\mathbf{v}(\mathbf{x}, 0) = \mathbf{0}; \tag{61}$$

$$\mathbf{u}(\mathbf{x}, 0) = \mathbf{0}; \tag{62}$$

where $\mathbf{x}$ is the position vector.

In the following, we compare the deformational behaviour of the model porous geometry through DNS to the analytical model proposed by de Boer et al.[25]. Since the analytical model is based on mixture theory, which assumes the porous media to be a binary mixture of superimposed but immiscible constituents, the model makes use of bulk properties of the media. Two important bulk properties that appear in the analytical model are the permeability (K^F) and average bulk elastic modulus (E_{avg}). In the following we describe the calculation of these bulk properties for the chosen model porous media. It should be noted that these parameters are evaluated only to compare the LBM-FEM direct numerical simulation results to the mixture theory based analytical model. These parameters are not required and have not been used in the direct numerical simulations.

4.1.1 Permeability of Simple Cubic arrangement

The conventional (Darcy) permeability K^F is given as $\frac{\kappa^F \rho^F g}{\mu^F}$ where κ^F is the intrinsic permeability with dimensions L^2, ρ^F is fluid density, g is acceleration due to gravity and μ^F is the fluid dynamic viscosity. There are a number of different models to predict the value of intrinsic permeability κ^F. In this study the Kozeny-Carman relationship between κ^F and porosity n^F is used. For porous media made of spherical particles, the updated Kozeny-Carman relationship is given as

$$\kappa^F = \frac{{d_p}^2 (n^F)^3}{180\,(1 - n^F)^2} \tag{63}$$

where d_p is the average diameter of the particles that comprise the porous media and n^F is the void fraction or porosity of the medium. The resulting value of K^F for the chosen SC arrangement for the chosen SC arrangement is listed in table 3.

4.1.2 Bulk elastic properties of Simple Cubic arrangement

The values of λ^S and μ^S used in the de Boer et al.[25] model correspond to the bulk elastic properties of the macroscopic porous media. However the material properties used in the LBM-FEM simulations correspond to the solid constituent. Thus, in order to compare the TPM model with the direct numerical simulation approach, a correspondence needs to established between the bulk elastic properties of the macroscopic porous media and those of solid constituent.

For a SC arrangement under homothetic loading conditions [34] derived the relationship between stress and strain for finite loading conditions. The application of normal stresses, in a SC arrangement, results only in normal component of strains. The relationship between the infinitesimal increase in normal stress ($d\sigma_{ii}$) and the corresponding infinitesimal increase in the normal strain ($d\epsilon_{ii}$) is given by Deresiewicz as

$$d\epsilon_{ii} = \frac{2R}{E^* a} d\sigma_{ii}, \tag{64}$$

where E^* is the given as $\frac{E}{(1-\nu^2)}$, where E is the Young's modulus and ν is the Poisson ratio. R is the radius of the spheres. Further a is the instantaneous contact radius between the spheres. The Hertzian contact model is used to predict the contact radius as

$$a = \left[\frac{3R^* P_z}{E^*}\right]^{1/3}, \tag{65}$$

where P_z is the applied load and R^* is equal to $\frac{R}{4}$ for spheres of radius R. From equation 64 one can obtain a bulk elastic modulus (E_b) of the system which is essentially

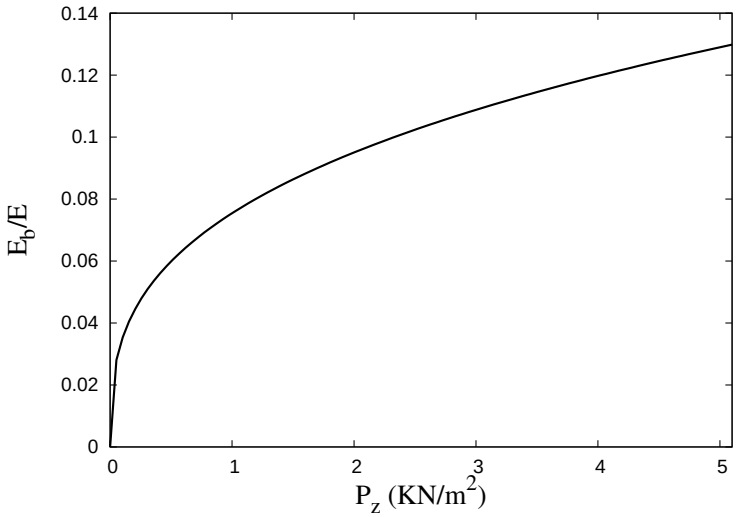

Figure 28: Instantaneous compressive bulk modulus E_b as a function of applied load.

the rate of change of stress with respect to strain and is given as

$$E_b = \frac{E^* a}{2R}. \tag{66}$$

It should be noted here that the above expression shows that the compressive modulus E_b is not only a function of material properties (E,ν), but also a function of instantaneous contact radius a and thus a function of applied force P_z. This implies that the compressive modulus E_b can be very small compared to the Young's modulus (E) if the applied stress (P_z) is small. Figure 28 shows the variation of the instantaneous bulk modulus with load P_z. Thus for small values of P_z the ratio E_b/E is also very small. For instance for the parameters chosen for these simulation, as presented in table 3, the ratio E_b/E is given by 0.027. Physically, the small value of E_b compared to E can be interprited as the high compressibility of the arrangement when the value of contact radius a is very small. As a tends towards zero, the stress concentration at the contact points is large and hense the strucutre is very compressible. Appendix B provides further justification of such low value of E_b and also compares E_b with Deresiewicz's results.

Table 3: Values of parameters used for comparing LBM-FEM code with de Boer et al.[25] model, for the case of spheres in SC arrangement.

E	$47.02MPa$
E_{avg}	$2.7325MPa$
n^F	0.5138
n^S	0.4862
ρ^{FR}	1000 kg/m^3
ρ^{SR}	2000 kg/m^3
λ^S	1.4626 MN/m^2
μ^S	1.0591 MN/m^2
K^F	0.000255 m/s
γ^{FR}	10.0 KN/m^2
$f(t)$	0.0489 KN/m^2

As mentioned above, the expression given in equation 66 represents the instantaneous bulk elastic modulus of the system, which varies as the contact radius a varies during compression. The contact radius a varies as the cube root of the applied load P_z. Thus if the loading is assumed to be a quasi-static process, an average bulk modulus of the system can be obtained by integrating equation 66 between $P_z = 0$ to $P_z = P_o$ and normalizing with P_o. This results in the average bulk elastic modulus (E_{avg}) given as

$$E_{avg} = \frac{3E^* a_o}{8R}. \tag{67}$$

where a_o is the contact radius due to the applied load P_o. In this study, the single phase Young's modulus E used for the spheres in LBM-FEM simulations are given in table 3. The average bulk modulus E_{avg} and the corresponding Lame's constants (λ^S, μ^S), used in de Boer et al.[25] model, for the porous media are also given in table 3.

4.1.3 Deformation of Simple Cubic Granular Media

Equation 25 gives the dynamic response of a semi-infinite saturated porous medium under time dependent external load. Since real geometries have the limitation of finite length, geometries of three different lengths are chosen for comparison with de

Boer et al.[25] model. One-dimensional SC arrangement of $10, 20$ and 32 spheres are used in this study. All the arrangements contain spheres of equal diameter and same material properties to model an isotropic and homogeneous porous media.

The values of contact parameters correspond to those chosen for a similar load to validate with Hertz model. Thus no open-ended parameters are involved in this study.

Further the effect of finite element mesh resolution on the deformation response has been studied. Two different finite element mesh resolutions have been used to discretize the spheres. The first mesh has 10 elements across the diameter of the sphere. The parameter l_{fea} defined as the ratio of average finite element edge length to the unit LBM edge length is equal to 4. While the other mesh has 20 elements, twice as many, across the diameter of the sphere, thus $l_{fea} = 2$.

The values of non-dimensional parameters are chosen to be $Re, Ca \ll 1$, $\rho^* = 2.0$, $n^* = 0.95$ and $K^* = 0.003$. The detailed list of all the parameters and their values in SI units are listed in table 3.

Figure 29 shows the results of using the mesh with l_{fea} equal to 4. The average deformation responses of top surface nodes for $10, 20$ and 32 sphere geometries under impulse loading using LBM-FEM method are compared to de Boer et al.[25] model and found to match closely. An asymptotic behaviour is seen in the deformation that varies with the domain size. The asymptotic behaviour marks the deformation reaching a steady state, when the internal stress in the geometry balances the applied load. Concordant to intuition, the on-set of steady state is delayed with increasing domain size. This is because the deformation corresponding to a given bulk strain is higher with increasing domain size. The 10 sphere domain reaches steady state quickly followed by the 20 sphere geometry, while the 32 sphere geometry does not reach a steady state within the simulated time.

The effect of using a finer mesh resolution has been studied by choosing l_{fea} equal

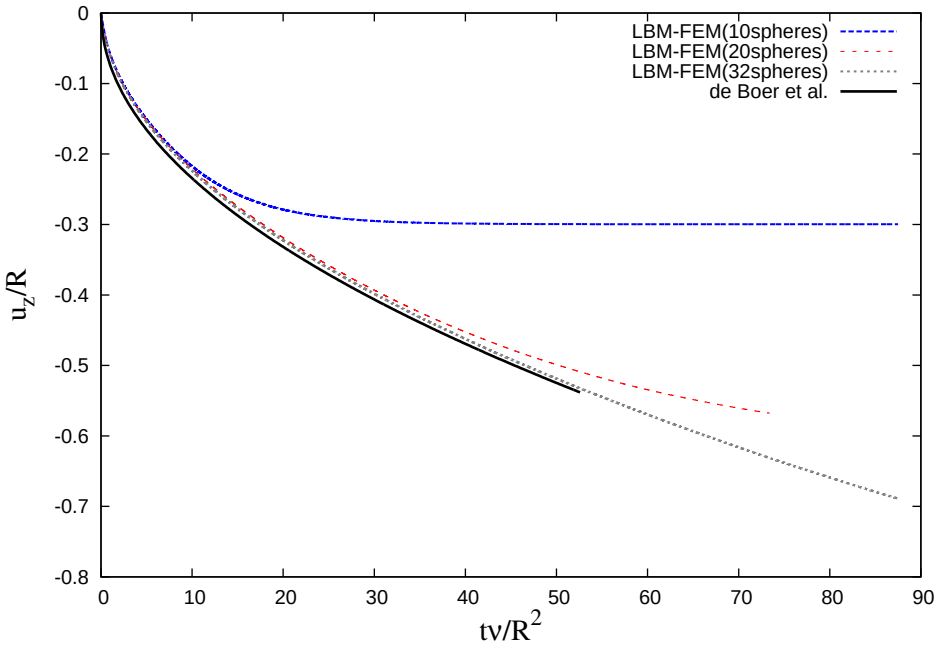

Figure 29: The average displacement of the top surface nodes of simple cubic arrangement of spheres with 10, 20 and 32 spheres using LBM-FEM direct numerical simulations with $l_{fea} = 4$. The displacement response is compared to the analytical model proposed by de Boer et al.[25]

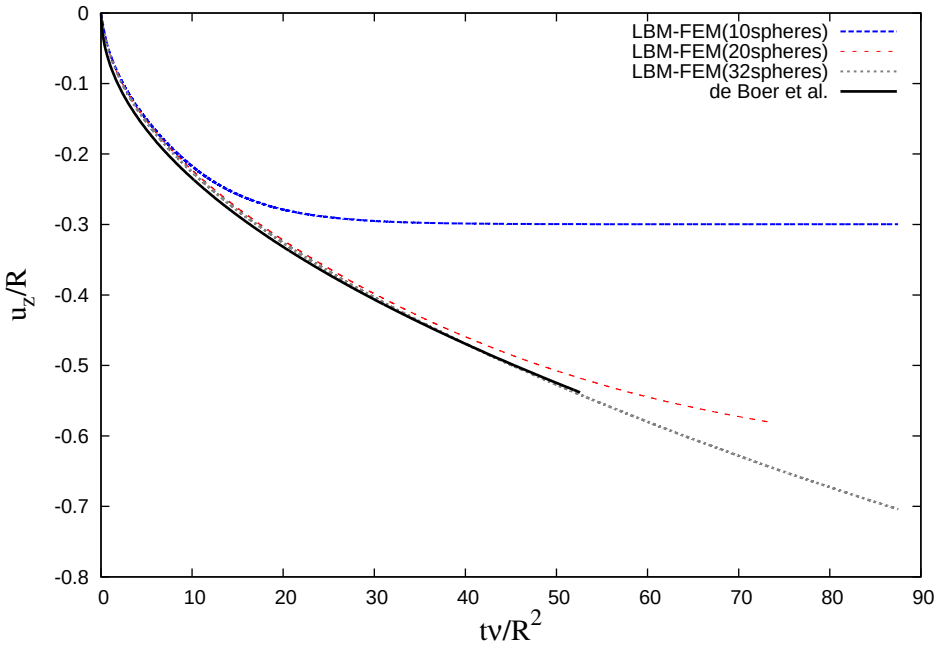

Figure 30: The average displacement of the top surface nodes of the model porous media geometries using simple cubic arrangement of spheres. The model geometries of 10, 20 and 32 spheres have been meshed using $l_{fea} = 2$. The displacement response is compared to the analytical model proposed by de Boer et al.[25]

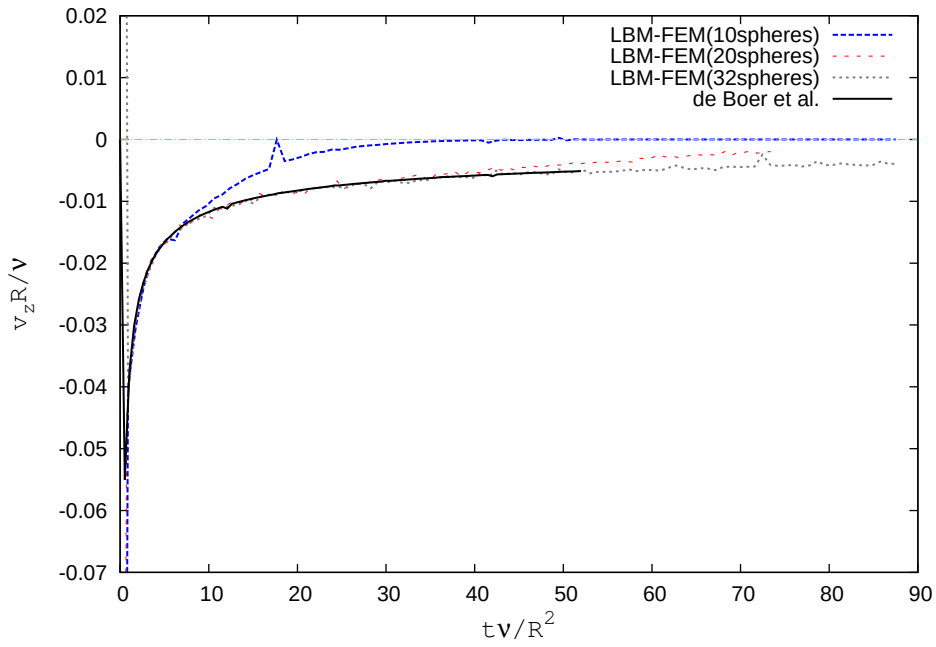

Figure 31: Comparison of the velocity response of the model porous geometries made up of spheres with the analytical model.

to 2. The results are shows in figure 30. It is seen that LBM-FEM simulation results match the analytic model more closely. It is to be noted that although there is some difference between the coarse and fine mesh results the difference is less than 3%. Thus further mesh refinement would not lead to significantly different behaviour in the deformation response. In subsequent plots, the results shown have been generated using l_{fea} equal to 4.

Figure 31 shows the average velocity response of the top surface of nodes for $10, 20$ and 32 sphere geometries and its comparison with de Boer et al.[25] analytical model. The velocity is large at the beginning of the compression followed by a rapid decrease and then an asymptotic behaviour to zero. This suggests rapid deformation during the early part of compression followed by a slow deformation phase. Again it is seen that the 10 spheres geometry seizes to deform first followed by 20 spheres geometry, whereas the 32 spheres geometry follows de Boer et al.[25] model closely within the simulated time. The small fluctuations in the velocity response are caused due to

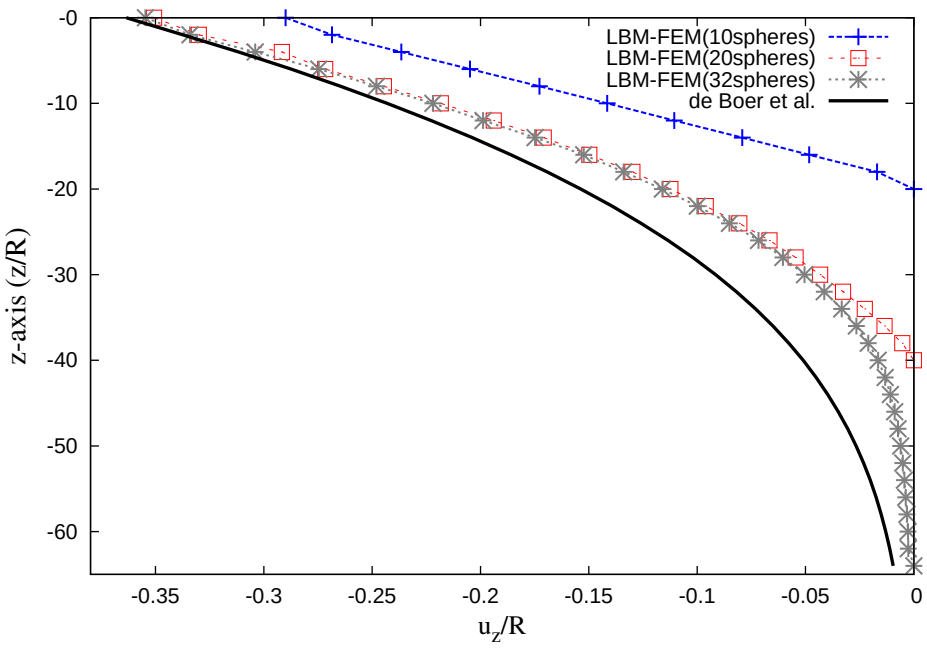

Figure 32: Comparison of displacement along the z-axis from LBM-FEM simulations of SC arrangement and the de Boer et al. model at $\frac{t\nu}{R^2} = 24$. $z = 0$, represents the top surface and z is positive downwards

minor instabilities arising from the contact model.

Figure 32 shows the normalized displacements along the z-axis from the LBM-FEM simulations of 10, 20 and 32 sphere geometries, along with the de Boer et al. model data. The z-axis is positive in the downward direction, such that $z = 0$ indicates the top surface of the geometries. The displacement values have been collected at time $\frac{t\nu}{R^2} = 24$. At this time, the 10 sphere geometry has reached the final deformation state. Thus, the 10 sphere curve shows a linear behaviour, indicting the constant strain throughout the geometry. The 20 and 32 sphere geometries have not reached the final deformation, hence their plots do not show a linear behaviour. The 20 sphere curve matches well with de Boer et al. model at the top ($z = 0$), but diverges quickly below the top surface due to its limited geometric length. The 32 sphere curve also matches well with the de Boer et al. model at the top and diverges towards the bottom. However, it shows a better match with the analytical model than the 20

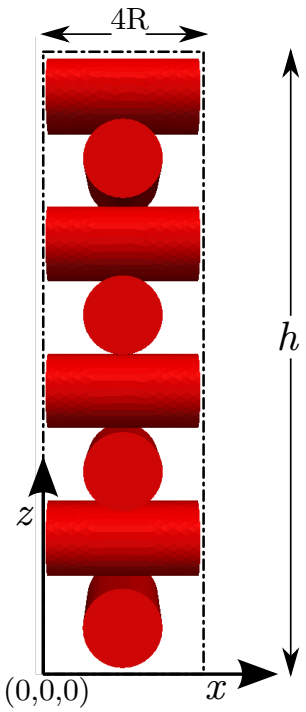

Figure 33: Setup and dimensions of model porous media geometry made up of cylindrical arrangements. Dotted lines shows the simulation domain.

sphere curve.

4.2 Behaviour of Ordered Fibrous Porous Media

In this section, the behaviour of saturated porous media under instantaneous compressive loading is analyzed using model porous media made of cylindrical arrangements. Ordered orthogonally crossing cylinders as shown in figure 36 make up the porous media. The symmetric nature of such a geometry can be made use to simplify the simulation geometry, as shown in figure 33.

The boundary conditions for the fluid and solid phases are the same as discussed for SC arrangement. At the bottom, no-slip, no-displacement condition is imposed given as

$$\mathbf{v} = 0; u_z = 0; at\ z = 0; \tag{68}$$

At the top, load is applied to the solid FE nodes and outflow condition is applied on

the fluid; given as,

$$\frac{\partial v_x}{\partial z} = \frac{\partial v_y}{\partial z} = \frac{\partial v_z}{\partial z} = 0; \mathbf{F}(t) = -f(t)\hat{k};\ at\ z = h, \tag{69}$$

Finally on the four vertical wall a symmetry condition is applied, given as,

$$v_x = 0; u_x = 0; at\ x = 0, 4R; \tag{70}$$

$$v_y = 0; u_y = 0; at\ y = 0, 4R. \tag{71}$$

The initial conditions are given as

$$\mathbf{v}(\mathbf{x}, 0) = \mathbf{0}; \tag{72}$$

$$\mathbf{u}(\mathbf{x}, 0) = \mathbf{0}; \tag{73}$$

where $\mathbf{x}$ is the position vector.

In order to compare the direct numerical simulations with the mixture theory model of de Boer et al.[25] the values of two bulk parameters need to be obtained i.e the permeability (K^F) and the average bulk elastic modulus (E_{avg}) of the porous media. In the following, these parameter are evaluated for ordered orthogonally crossing cylindrical arrangements as shown in figure 36.

4.2.1 Permeability of ordered orthogonally crossing fibrous arrangement

As discussed in the section 1, there have been a lot of studies, numerical, experimental and analytical in understanding and developing models to predict permeability of a porous media made up of cylindrical arrangements. Most of these studies have been conducted to investigate flows in very low to low solid volume fractions ($n^S <$ 0.3). However, the geometrical arrangement that is intended to be used in these simulations has a solid volume fraction of $n^S = 0.3927$. The only investigations using orthogonally crossing cylindrical arrangements in high solid volume fraction

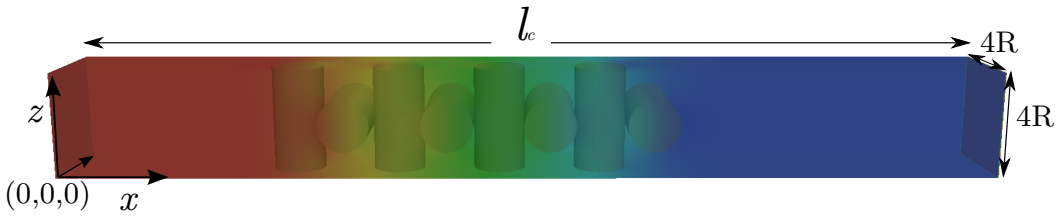

Figure 34: Setup and dimensions of the geometry used to determine permeability of the ordered orthogonally placed cylindrical arrangements. The color contours represents pressure variation at steady state.

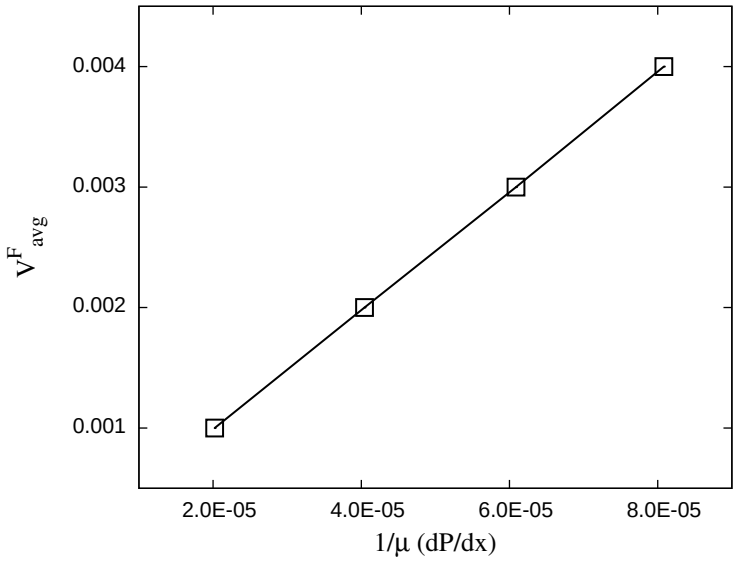

Figure 35: Variation of pressure drop ($\frac{1}{\mu}\frac{dP}{dx}$) with average flow velocity V_{avg}. The slope of the line gives the permeability (κ^F). The velocity and pressure gradient values are in Lattice Boltzmann units.

geometries has been performed by [66]. However, the geometry used by them is a layered cylindrical arrangement where each layer consists of overlapping cylinders. Further these layers are separated from each other by cylinder half distance. Thus due to the lack of information available for permeability in orthogonally crossing cylindrical arrangements where the flow is normal to the cylinder axis, a permeability study has been carried out.

The Darcy's law relates the average fluid velocity to the pressure gradient in the fluid and is given as

$$\langle \mathbf{v} \rangle = \frac{\kappa^{\mathbf{F}}}{\mu} \cdot \nabla P, \tag{74}$$

where $\langle \mathbf{v} \rangle$ is the average flow velocity, μ is the fluid viscosity, ∇P is the resulting pressure gradient and $\kappa^{\mathbf{F}}$ is the intrinsic permeability tensor that only depends on the geometry of the porous media. For a homogeneous isotropic system, $\kappa^{\mathbf{F}} = \kappa^F \mathbf{I}$ where $\mathbf{I}$ is the identity tensor.

In order to obtain the value of κ^F for the cylindrical arrangement, numerical simulations of fluid flow through the arrangement have been performed. The lattice Boltzmann method has been used to simulate fluid flow. The method has already been validated for accurate prediction of pressure drop in flow through porous media [47].

The 8 cylinder arrangement as shown in figure 34 is used to determine the permeability. Each cylinder has a diameter of 40 lattice units and length of 80 lattice units. A fluid domain of 720x80x80 lattice units is used in these calculations. This length of the domain provides enough space before and after the geometry to eliminate entrance and outlet to effect the pressure drop calculations. The fluid flows in the x-direction, the boundary conditions are;

$$\mathbf{v} = V_o \hat{i};\ at\ x = 0; \tag{75}$$

$$\frac{\partial v_x}{\partial x} = \frac{\partial v_y}{\partial x} = \frac{\partial v_z}{\partial x} = 0;\ at\ x = l_c, \tag{76}$$

$$v_y = 0;\ at\ y = 0, 4R; \tag{77}$$

$$v_z = 0;\ at\ z = 0, 4R; \tag{78}$$

The inlet velocity is varied and the resulting pressure drop is measured. In each case, the simulations are run till a steady state distribution of pressure and velocity values are attained throughout the domain.

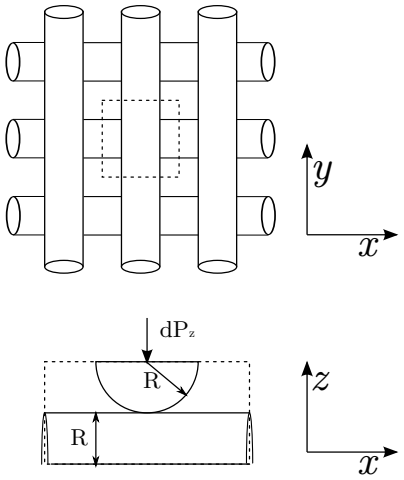

Figure 36: Ordered orthogonally aligned axis, arrangement of two layers of cylinders. Due to symmetry, the dotted region can be taken as a unit cell which has the same elastic characteristics as the entire arrangement.

Figure 35 shows the variation of pressure ($\frac{1}{\mu}\frac{dP}{dx}$) with average flow velocity V_{avg}. The inverse of the average slope of the line gives the intrinsic permeability (κ^F). The value of average Darcy permeability resulting from these simulations is given in (table 4). This is the value of permeability that is used in the analytical model for comparison with LBM-FEM simulations.

4.2.2 Bulk elastic properties of ordered orthogonally crossing fibrous arrangement

The simple ordered orthogonally crossing homogeneous and isotropic cylindrical arrangement is as shown in figure 36. The two layers of cylinders are placed such that the axis of one layer is orthogonal to the axis of the other layer. Due to symmetry, the dotted region can be taken as a unit cell which has the same elastic characteristics as the entire arrangement.

In this analysis, we only look at the bulk modulus of the unit cell in the z-direction. Generally in transversly isotropic porous media such as the one shown in figure 36, one is interested in the compression of the porous media in the transverse direction, which in this case is the z-direction. In order to obtain the bulk modulus of this unit

cell, the Stress-Strain relationship is examined for compressive (Z-direction) loading. The authors follow the analysis presented by [34] for the Stress-Strain relationship of a simple cubic arrangement of spheres under finite deformation.

Let there be an incremental force dP_z applied to the unit cell as shown in figure 36. Each cylinder has two points of contact within a unit cell length, one at the top and one at the bottom. At these points of contact there is a normal reaction force (dN_z). Due to the geometric symmetry, these contact forces, at top and bottom, are equal and opposite and also equal to the applied external load dP_z.

Thus, the expression for the incremental compressive stress $d\sigma_z$ is given as

$$d\sigma_{zz} = \frac{dP_z}{16R^2}. \tag{79}$$

The relative incremental displacements of the cylinders is the incremental strain given as

$$d\epsilon_{zz} = \frac{d\alpha}{2R}, \tag{80}$$

where α is the incremental displacement of the cylinders in the z-direction. Thus the relationship between incremental stress and incremental strain is given as

$$d\epsilon_{zz} = 8RCd\sigma_{zz}, \tag{81}$$

where $C = \frac{d\alpha}{dP_z}$ is the normal compliance. Now, the Hertz contact theory can be used to evaluate the compliance C. According to Hertz contact theory the contact radius a and the normal displacement α for two orthogonal cylinders with same radius R and material properties E, ν in contact under a compressive force P_z is given by

$$\alpha = \left[\frac{9{P_z}^2}{8R^*{E^*}^2}\right]^{\frac{1}{3}}, \tag{82}$$

$$a = \left[\frac{3P_zR^*}{E^*}\right]^{\frac{1}{3}}, \tag{83}$$

where $E^* = \frac{E}{1-\nu^2}$ and $1/R^* = 2/R$; R being the radius of the cylinders. Therefore the compliance C is given as

$$\frac{d\alpha}{dP_z} = \frac{1}{E^* a}. \tag{84}$$

Substituting the value of compliance into the Stress-Strain relation given by equation 81 we get

$$d\epsilon_{zz} = \frac{8R}{E^* a} d\sigma_{zz}. \tag{85}$$

The above equation gives the instantaneous bulk elastic modulus (E_b) of the system as

$$E_b = \frac{E^* a}{8R}. \tag{86}$$

In order to obtain an average bulk elastic modulus of the system (E_{avg}) one can integrate the above expression from $P_z = 0$ to $P_z = P_o$ and normalize the resulting expression with P_o. Thus the average bulk modulus of the system is

$$E_{avg} = \frac{3E^* a_o}{32R}. \tag{87}$$

where a_o is the contact radius due to the applied load P_o. The above value of bulk modulus is lower than the bulk modulus for the SC spherical arrangement, even though the relative displacement α is lower for contact between cylinders compared to contact between spheres, for the same applied load P. This is because of the low solid volume fraction in the case of cylindrical arrangement ($n^S = 0.3836$) compared to the spherical arrangement ($n^S = 0.5138$). Table 4 lists the values of E, E_{avg} and Lame's constants λ^S, μ^S.

Table 4: Values of parameters used for comparing deformation of cylindrical arrangements with de Boer et al.[25] model

E	$46.08MPa$
E_{avg}	$0.8973MPa$
n^F	0.6164
n^S	0.3836
ρ^{FR}	1000 kg/m^3
ρ^{SR}	2000 kg/m^3
λ^S	0.4803 MN/m^2
μ^S	0.34781 MN/m^2
K^F	0.000738 m/s
γ^{FR}	10.0 KN/m^2
$f(t)$	0.01677 KN/m^2

4.2.3 Deformation of Ordered Orthogonally crossing Fibrous Media

The deformation of a model porous media under instantaneous compressive loading is analyzed in the following. The model porous media is made up of layers of ordered orthogonally crossing cylinders as shown in figure 36. Three different sizes of geometries consisting of $8, 16$ and 32 cylinders are used.

The contact parameters used are the same as those chosen to validate the Hertz's contact model (figure 21d). Thus no open ended parameters have been used in this study. The FE mesh used to resolve the cylinders is as shown in figure 21b, which results in 10 finite elements across the diameter of each cylinder.

The values of non-dimensional parameters chosen in this study are $Re, Ca \ll 1$, $\rho^* = 2.0$, $n^* = 0.6223$ and $K^* = 0.092$. The detailed list of all the parameters and their chosen values are provided in table 4.

Figure 37 shows the average deformation of the top surface of the three geometries and their comparison with the analytical model of de Boer et al.[25] for instantaneous compressive loading. The plot shows a similar behaviour of deformational response as seen for the spherical arrangements, albeit there is a lot more deformation occurring. The longer geometries deform more than the shorter geometries. Again there is a good match between the deformation response of the model porous media geometries and the analytical model of de Boer et al.[25].

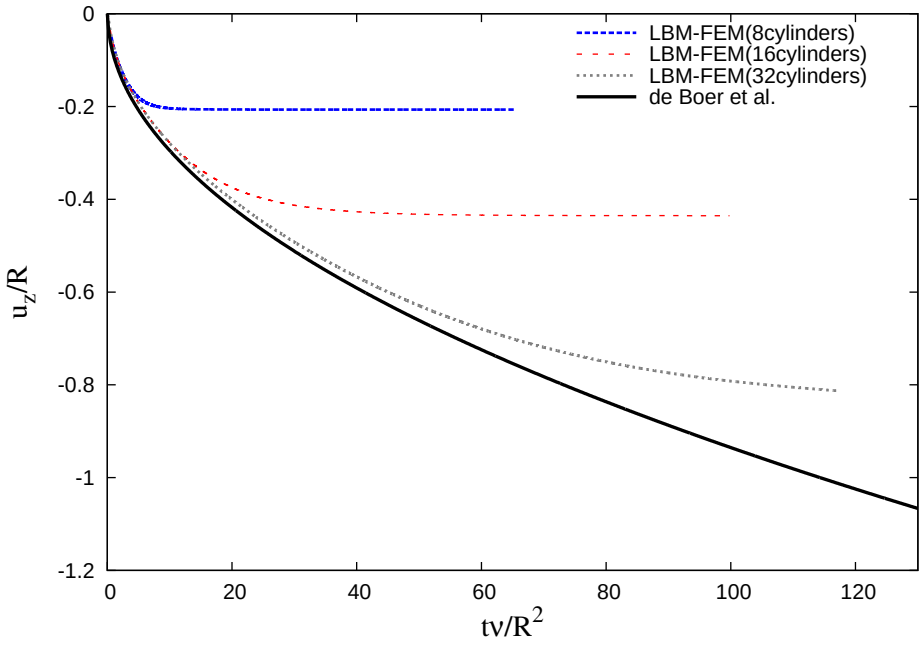

Figure 37: Comparison between LBM-FEM simulations of saturated porous media compression with de Boer et al.[25] model. Deformational response of top surface nodes of 8, 16 and 32 cylinders geometries are shown.

Figure 38 shows the comparison of velocity response between the LBM-FEM simulations of compression of model porous media using cylindrical arrangement with de Boer et al.[25] model. Again we see a good match between the analytical model and LBM-FEM simulations results, particularly for the 32 cylinder geometry.

Figure 39 shows the normalized displacements along the z-axis from the LBM-FEM simulations of 8, 16 and 32 cylinder geometries, along with the de Boer et al. model data. The z-axis is positive in the downward direction, such that $z = 0$ indicates the top surface of the geometries. The displacement values have been collected at time $\frac{t\nu}{R^2} = 20$. At this time, the 8 cylinder geometry has reached the final deformation state. Thus, the 8 cylinder curve shows a linear behaviour, indicting the constant strain throughout the geometry. The 16 cylinder geometry also shows a similar behviour. However, the 32 cylinder geometries has not reached the final deformation, hence its plot does not show a linear behaviour. Further, the 32 cylinder geometry matches

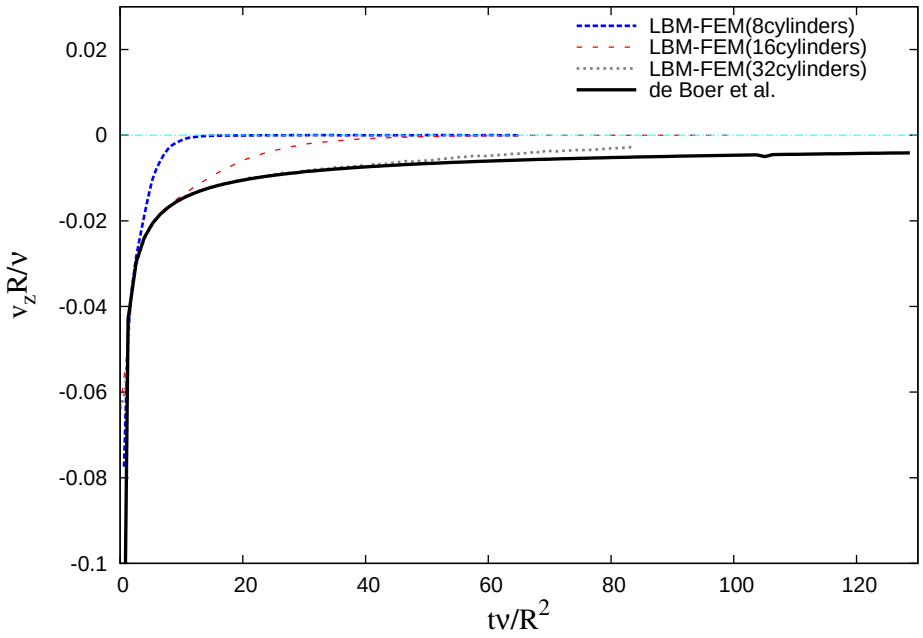

Figure 38: Comparison of velocity response between LBM-FEM simulations of saturated porous media compression with de Boer et al.[25] model. Velocity response of top surface nodes of 8, 16 and 32 cylinder geometries are shown.

with the analytical solution closely. The match is better at the top and deviates towards the bottom of the geometry. This shows that as the size of the geometry increases there is a better match with the analytical solution.

This study shows that the macroscopic behaviour of a generic porous media can be recovered using regular arrangements of simple geometries as long as the porosity, permeability and the bulk modulus is matched between the porous media and the simplied geometry. The study also shows that the average bulk elastic modulus calculated based on small strain theory and Hertz contact model provides a good estimate of the elastic property of the model porous media made up of spheres and cylinders in ordered arrangement in small strain limit.

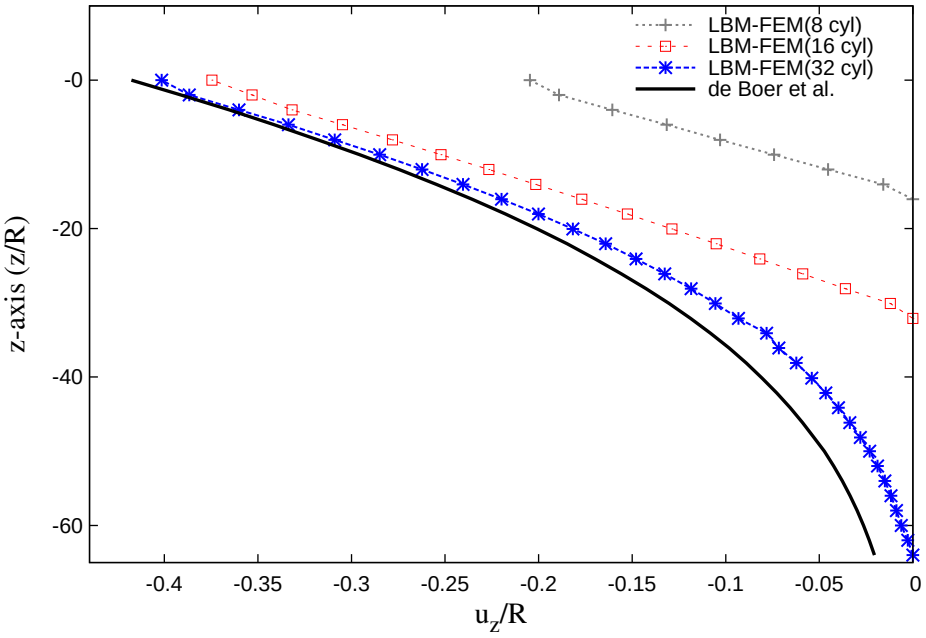

Figure 39: Comparison of displacement along the z-axis from LBM-FEM simulations of SC arrangement and the de Boer et al. model at $\frac{t\nu}{R^2} = 20$. $z = 0$ represents the top surface and z is positive downwards.

CHAPTER V

MODELING COMPLEX FIBROUS POROUS MEDIA

5.1 Wet-Pressing and Felts

In the paper industry, wet-pressing is a critical component of paper making. In the process of wet-pressing continuous sheets of wet paper and felt pass through rollers or a roller and a die, as shown in Figure 1. Water in the paper web is squeezed partially into the felt and partially out of the system. Subsequently the moist paper passes through a series of heated rollers where the rest of the water is removed through vaporization.

As can be seen in the above table, the cost of removing water in the drying stage is expensive because of the energy intensive process of vaporization. Energy spent in drying can be reduced if water is removed more effectively during pressing. On an average the percentage solids content entering the drying is between 45% and 50%. Figure 3 shows the effect of increasing the ingoing solids on the cost of drying. As can be seen an increase in the solids from 50% to 52% going into the drying section,

Figure 40: Water removal during wet pressing

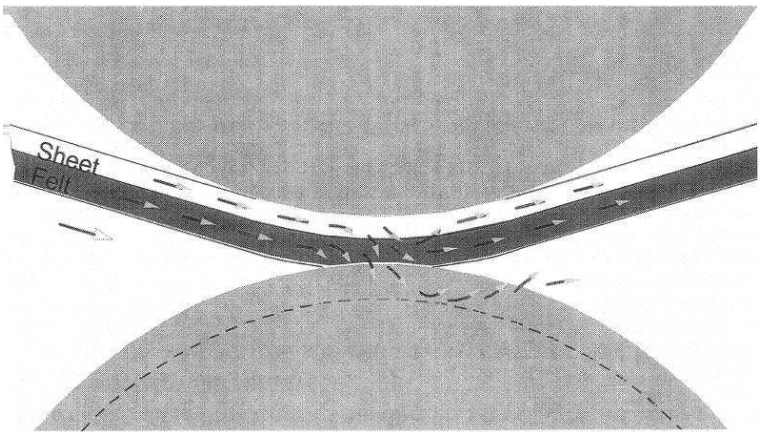

Table 5: Comparing Pressing And Drying

Process	% solids at end of process	Energy/Kg of water removed
Pressing	45-50	2.786 KJ/Kg
Drying	85-93	2257 KJ/Kg

Figure 41: Relative cost of water removal in forming, pressing and drying

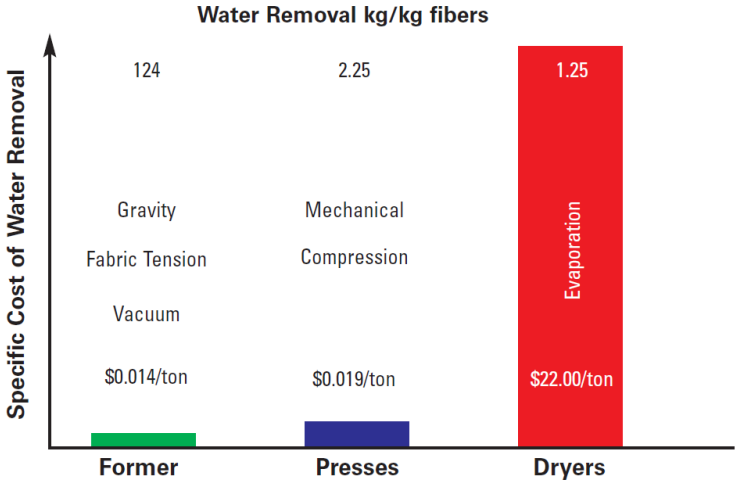

leads to a change in cost per ton of drying by $10. Paper mills vary a lot in terms of the production, but roughly the production of paper is between 10,000-100,000 tons per year. Thus efficiency improvements of the order of 1-2% increase in solids can accumulate to hundreds of thousands of dollars on energy savings.

Consequently the process of pressing has been studied extensively, albeit from the perspective of designing effective presses section with optimal loading profile. Experimental studies were conducted by Wahlstrom (1960) [73] which resulted in proposing a three phase process of pressing based on the compression of paper web. The first phase consists of the paperfelt system entering the press nip and extends till the mid nip region. The second phase starts from the midnip and ends when void regions start to develop in the paper and felt system. Following the end of second phase is the third phase which then continues till the paperfelt system exit the rollers. Most of the water is removed in the first phase and in the final phase he

Figure 42: Cost of drying with varying ingoing solid percentage

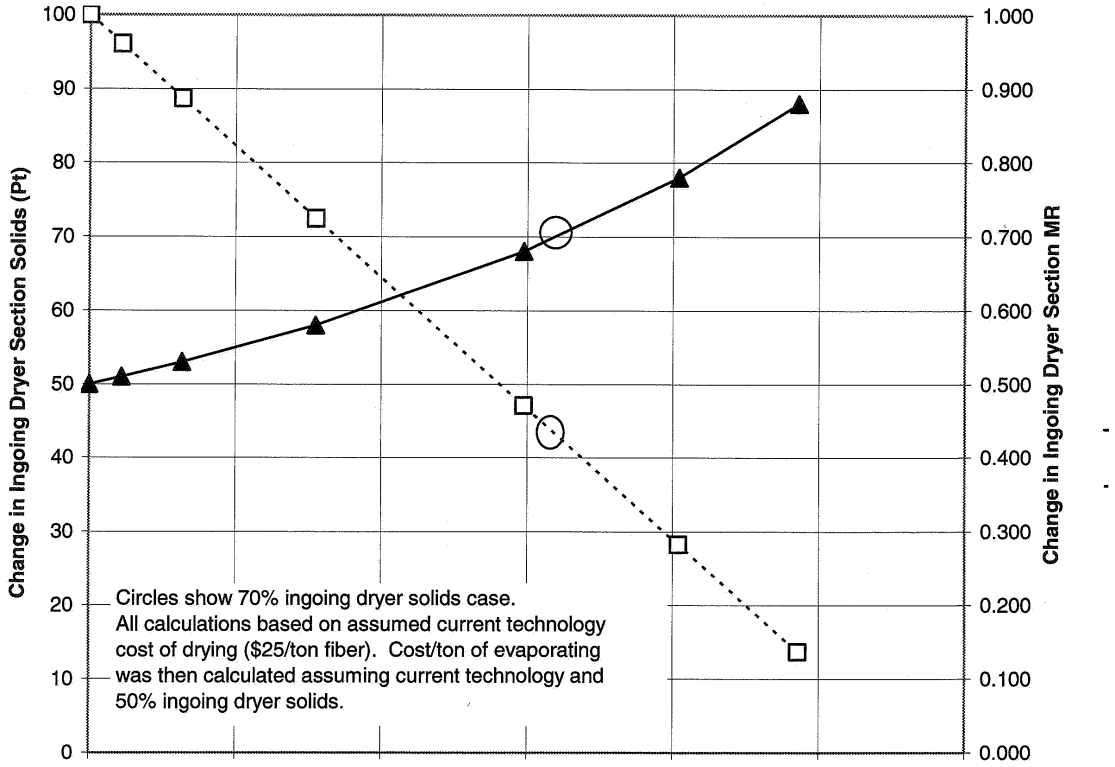

proposed rewetting due to capillarity. He also investigated the effect of felt properties and found that low drainage resistance, low compressibility and high density of felt promote water removal from paper.

Nilesson and Larson (1964) [60] proposed a fourphase pressing regime as shown in Figure 43. They included an additional phase at the beginning of the process where the paperfelt system enters the nip and reaches saturation. The phases that follow the first phase match the phases proposed by Wahlstrom.

Busker (1980) and Busker et. al.(1984) conducted several experimental studies to understand the effects of nip pressure and residence time of pressing. These findings resulted in proposing parameters that are important to the effective water removal in press section. Table gives the list of the variables that were considered important by Busker et al. They classified them as primary and secondary variables based on the extent of their effect on water removal. The primary variables showed 4%

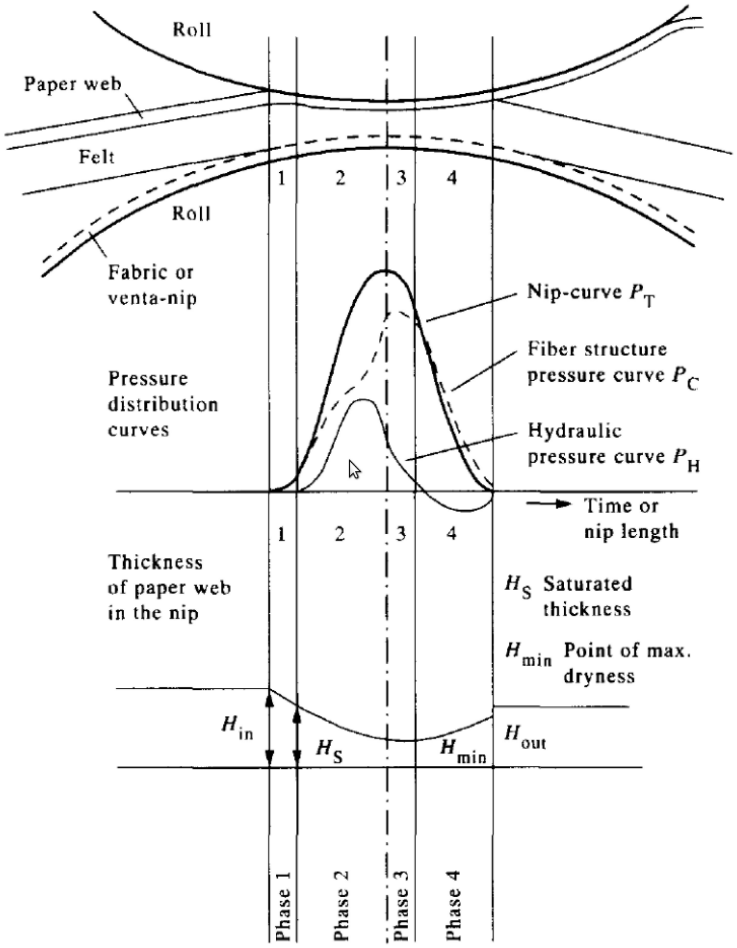

Figure 43: The four phase process of wet-pressing as proposed by Nilsson and Larson (1964) [60].

Table 6: Primary and Secondary variables that influence the process of wet-pressing as given by Busker and Cronin (1984)

Primary Variables	**Secondary Variables**
Post-nip rewet	Initial felt flow resistance
Ingoing sheet dryness	Ingoing felt dryness
Grammage	Rewet in the nip at speed
Furnish Properties	Shape of pressure profile
Double Felting	Roll Cover
Sheet Temperature	Felt Design
Impulse	Roll Venting
Felt Pressure Uniformity	

improvement in solids content while the secondary variables showed 2% improvement in solids content.

The numerical investigations in this area flowed the principles of consolidation theory, in the sense that the total stress load T is considered to be distributed between the fluid phase p and the porous solid region T^S. The fluid phase pressure also called the pore pressure or the hydraulic pressure p , is considered to create a pressure gradient in the fluid, such that the fluid flows away from the rollers. The hydraulic pressure along with Darcy's equation gives the fluid velocities as

$$n^F(\mathbf{v}^F - \mathbf{v}^S) = \frac{\kappa^F}{\mu^F}\nabla p \tag{88}$$

where $\mathbf{v}^F$ and $\mathbf{v}^S$ are the velocities of the fluid ans solid phase respectively.

In order to model the deformation of the solid structure and its effect on the flow of fluid, there have been a number of different models proposed.

Kerekes and McDonald (1991) [45, 44, 46] proposed a model for determining the moisture ration m of paper web, based on a decreasing permeability model. Using the KozenyCarman relation they made assumptions about the variation of properties like permeability and saturation to obtain an expression for moisture ratio given as

$$\frac{m}{m_o} = \left[1 + \frac{\phi f T}{m_o v}\right]^{\frac{1}{\phi}}, \tag{89}$$

where m_o is the initial moisture ratio, T is the total applied pressure, v is the velocity of the belt. Here ϕ the compressibility factor and f the permeability factor are variables which were evaluated by comparing with experimental data. Roux and Vincent [63] studied a twodimensional, threephase model for pressing and included capillary effects in the model. Kataja (1992) [43] developed a one-dimensional model in transverse direction for wet-pressing that included air, water and solid as three phases. Bezanovic et al. (2006[6], 2007[7], 2007[8]) performed rigorous mathematical analysis addressing existence, uniqueness and qualities of solution for a simplified onedimensional model of pressing. They incorporated a three phase model for paper and felt in terms of water saturation and void ratio. For a balance of dynamics between the paper and felt regions, a cross and matching boundary conditions are applied. This results in a nonlinear diffusion equation and a first order hyperbolic equation, which they solve numerically. However, for closure they formulated the constitutive relations between load and void fraction and the relation between void fraction and permeability as smooth parametric functions. The behavior of saturation and porosity in both phases with during pressing are reported.

As seen from the above literature then numerical investigations have been based on homogenization principles. Thus the studies made assumptions about the homogeneity of paper and felt structure and reduced the problem to a single dimension, usually in the transverse direction (perpendicular to machine direction). However in reality the felt structure is highly non-homogeneous and the newer felt design necessitate a variation in felt porosity being low near the paper surface and being high away from it. Figure 44 shows as sample felt structure that has been developed by obtaining x-ray microtomography images of real felt and then performing image analysis to reconstruct the solid model.

The figures shows a felt geometry that is highly nonhomogeneous and anisotropic. With varying fiber diameter, porosity and fiber orientation.

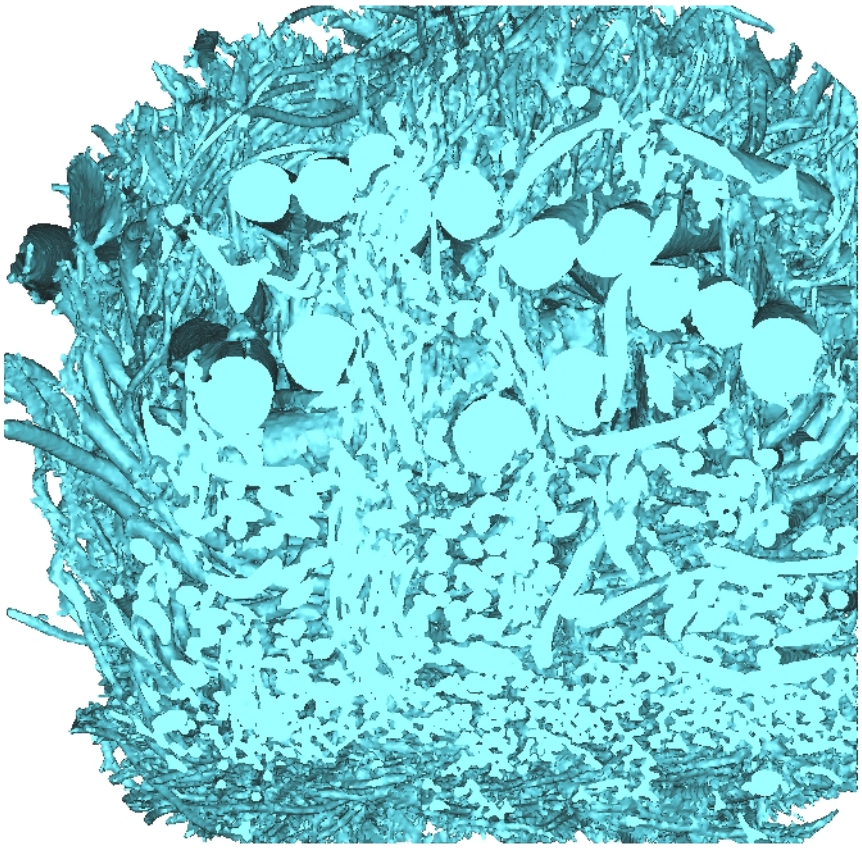

Figure 44: Three dimensional image of a $3 \times 3 \times 3.5$ mm sample of wet-pressing felt. The image was generated using the X-ray microtomography images of the real felt sample and then using image processing to concatenate the images and reconstructing the solid model.

The lack of a comprehensive understanding of the various parameters on the deformation and de-watering of felts has meant that the designs have been based on a qualitative understanding. Improvements in the felt design are possible if there is a better understanding of the process of felt deformation during pressing. Particularly, the effect of parameters like porosity, permeability and compressibility of felt on applied impulse profiles. Further information on the how the velocities in longitudinal and compression directions scale and compare can help in developing better models for the process of pressing.

5.2 Model layered fibrous porous media

As has been shown in chapter 3, the LB-FE method based on direct numerical simulation is a powerful tool to investigate behaviour of saturated deformable porous media. In spite of its efficiency and robustness, the method is dependent on the quality of the finite element mesh for accuracy. In the last decade, there have been improvements in the area of automatic mesh generation and adaptive mesh refining. Thus, it is not unreasonable to expect to be able to mesh the complex geometric structure of a real felt based on X-ray microtomography or MRI imaging.

However, in order to obtain accuracy of the order to $0.01 - 0.001$ microns it is necessary to use a fine mesh to resolve the geometry, usually of the order to 0.001 microns. Such a fine mesh can increase the computational load exponentially with the increase in the domain size. For a geometry of $3 \times 3 \times 3.5$ mm, the expected size of the finite element mesh is between $10^8 - 10^9$ degrees of freedom (DOF). Constructing and solving stiffness matrices for such huge geometries are prohibitive even with peta-scale level computational power.

Thus, it becomes necessary to look into ways by which the complex geometry of non-woven fibrous structures can be simplified to more regular arrangement of simple geometries. In chapter 4, it was shown that the deformational behaviour of a generic

porous media can be recovered using regular arrangements of simple geometries. In particular it was shown that cylinders arranged in an ordered orthogonal manner can be used to recover the deformational characteristics of a porous media with similar porosity (n^F), hydraulic conductivity (K^F)and the average bulk modulus (E_{avg}). Thus the parameters n^F,K^F and E_{avg} can be considered as the matching/similarity parameters that need to be matched between a real porous geometry, such as a non-woven structure and the model geometry to recover the deformational behviour of the real porous geometry.

This transformation in the geometry would then allow for drastic reduction in the computational size and meshing complexity without any significant change in the physics being modeled. As a consequence, the deformational behaviour of real non-woven structures with varying microstructure and properties through out the media can still be investigated.

In order to develop the model geometries that match the real fibrous geometries it is important to understand the effect of microstructure and fiber arrangement on the matching parameters n^F,K^F and E_{avg}. In the following, the effect of the fiber microstructure and arrangement is evaluated on the similarity/matching parameter permeability (n^F).

5.2.1 Literature in permeability of layered fibrous porous media

There is a lot of literature describing the effect of microstructure on the permeability of Fibrous media. Microstructure of fibrous materials, in general, can be considered to fall into three major categories: aligned structures, where axis of the cylindrical fibers are oriented either perpendicular or parallel to the flow direction (see, for instance, Chen and Papathanasiou, 2006, 2007), layered structures, where axes of cylindrical fibers lie randomly in the plane perpendicular to fluid flow (see, for instance, [75, 57, 77]), and random structures, where fibers axes can be randomly arranged in any

spatial direction ([71, 52])

The present work, focuses on non-woven structures which have application in absorbency products, filtration production and some composite products. The manufacturing process of such fibers consists of layer-by-layer deposition of fibers onto a flat surface with the axis of the fibers almost parallel to the flat surface [67]. This kind of fibrous media can be classified as a "layered" media [49], with transversely isotropic properties. Examples of such fibrous media are "felts", "filtration mats" etc.

Spielman and Goren [67] were one of the earliest to investigate the problems of permeability of layered porous media where the fiber axis is perpendicular to the direction of flow. They did not differential between fibrous media where the fiber axis are parallel to each other; orthogonal to each other or randomly oriented. They used Brinkman relation to derive the flow profile near a cylindrical fiber embedded within a fibrous network. The Brinkman relation essentially says that near an obstacle embedded within a porous media, the pressure drop is not only effected by the viscous dissipation effects but also due to the presence of other obstacles near by and is given as

$$\nabla P = \mu \nabla^2 \mathbf{v} - \mu \kappa^F \mathbf{v}, \tag{90}$$

where $\mathbf{v}$ is the velocity of the fluid close to the obstacle, κ^F is the intrinsic permeability, μ is the viscosity and P is the pressure. Using the above relation along with the continuity and appropriate boundary conditions Spielman and Goren obtain the velocity profile near a cylindrical fiber within a fibrous structure. They use the velocity profile to determine the drag force on the fibers and thus show that the variation of permeability with solid volume fraction (n^S) is given as

$$\frac{1}{2} + \frac{\sqrt{\kappa^F}}{r} \frac{K_1(r/\sqrt{\kappa^F})}{K_0(r/\sqrt{\kappa^F})} = \frac{1}{4n^S}, \tag{91}$$

where r is the fiber radius and K_i is the modified Bessel's function of order i.

It can be noticed that these expression only contain the fiber radius r and the

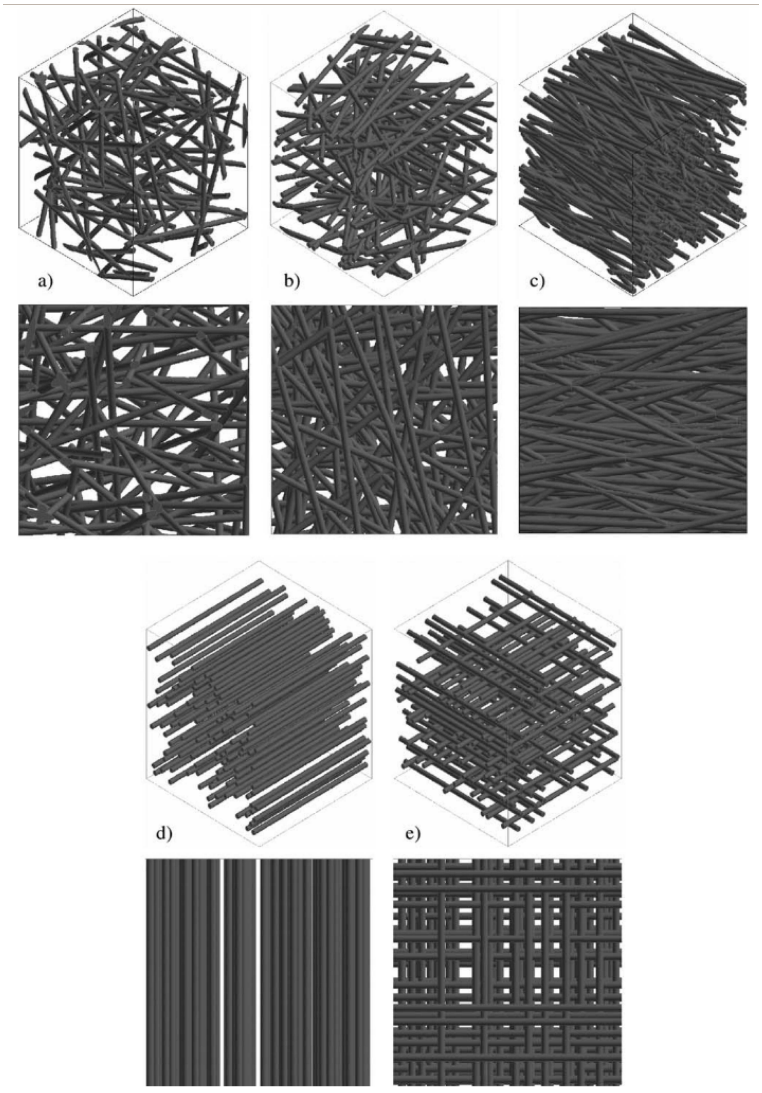

Figure 45: The fibrous microstructures considered in [69] from isometric and side views. a) 3D isotropic b) layered with random in-plane fiber orientation, c) highly oriented layered; d) disordered unidirectional e) disordered orthogonal media.

solid volume fraction n^F. The fiber orientation distribution and surface area normal to flow direction do not seem to have any effect on the permeability of layered fibrous media.

Jackson and James [39] provided insight into the experimental and theoretical studies conducted on fibrous porous media and provided an expression for permeability based on a simple weighted averaging of the stream wise and transverse permeability values as

$$\kappa^F = \frac{3r^2}{20n^F}\left(-\ln n^S - 0.931\right). \tag{92}$$

The popular empirical correlation of Davies [22] based on experimental work on planar fibrous sheets is also included here and is given as

$$\kappa^F = \frac{r^2}{16(n^S)^{3/2}(1+56n^{S^3})}. \tag{93}$$

In order to investigate the effect of fiber orientation distribution on the permeability of fibrous media Tahir and Tafreshi [69] performed numerical studies on virtually generated three-dimensional fibrous porous media. Figure 45 shows the various geometrical arrangements of fibers considered in their study. The unidirectional arrangement has all fibers aligned in the same direction but randomly placed in each layer. The orthogonal arrangement has fibers in one layer orthogonal to the fibers in adjacent layers, but the fibers are placed randomly within each layer. The highly oriented fibers have a standard deviation of 15^o in their θ_{xy} angle and the moderately oriented have a standard deviation of 30^o in their θ_{xy} angle. In the case of random arrangement this angle is 45^o. Note that in all these cases the θ_z is zero.

They used computational fluid dynamic tools based on finite volume method to simulate flow through the shown fibrous structures. The results of their study on the effect of fiber orientation distribution on the permeability of layered fibrous media are shown in figure 46. From the figure it is clear that there is little difference between the unidirectional, orthogonal, moderately oriented, highly oriented and random oriented

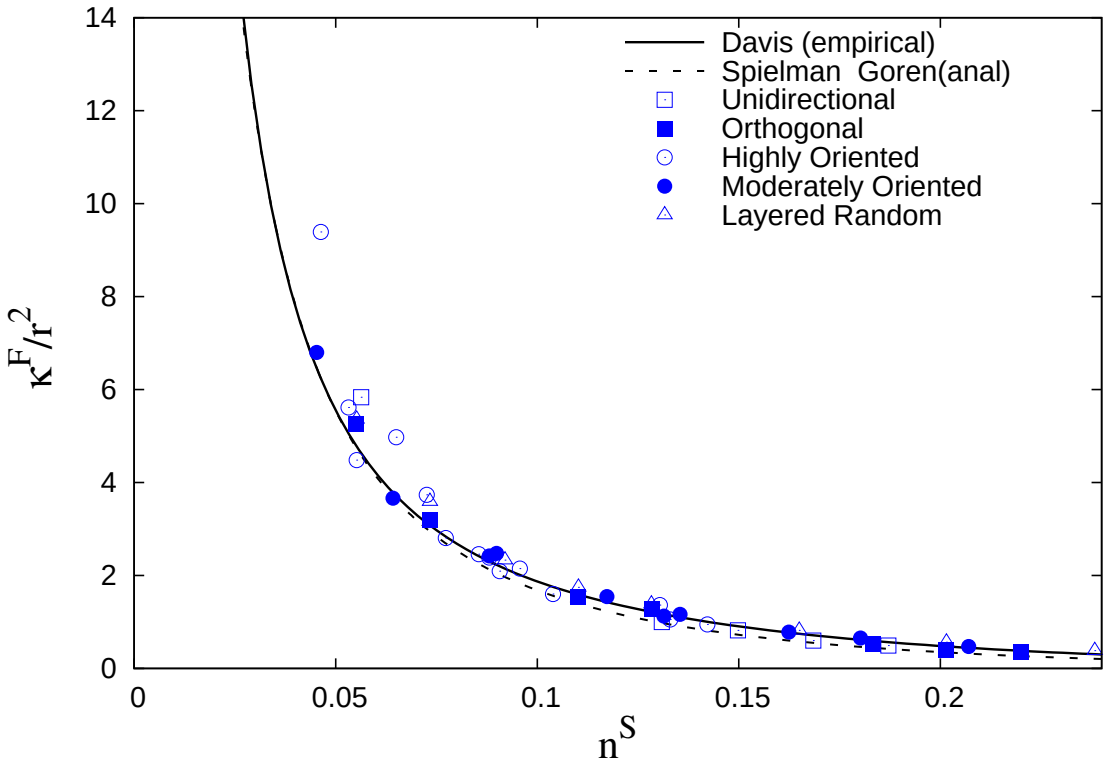

Figure 46: Permeability values from the numerical simulations of Tahir and Tafreshi [69]. The results are compared with the empirical model of Davis [22] and the analytical model of Speilman and Goren [67].

cases of virtual geometry in terms of their permeability to a transverse flow. Tahir and Tafreshi point out that though the permeability is not effected by in-plane orientation of fibers in a layered fibrous media, in the case of highly ordered layered structures the permeability may increase as pointed out by Sobera and Kleijin [66].

It should be noted that Sobera and Kleijn conducted studies on single layered fibrous structures where the cylindrical fibers overlap. In such structures a small amount of disorder can create increased open areas for flow to pass through and thus increase permeability, whereas more ordered geometry cause the flow to break up more and thus reduce the permeability.

It is critical to mention here the work done by Jaganathan et al. [40] in determining the permeability of real non-woven structures, through numerical simulation of flow

(a) Non-Woven

(b) 3D reconstructed Model of Non-Woven

Figure 47: The non-woven fibrous structure and the reconstructed 3D model developed by [40]based on DVI imaging, segmentation, voxel generation and complete 3D reconstruction.

through these geometries. They used a DVI technique to obtain 2D cross-sectional images of the real non-woven fibrous structure. Resolution of images obtained from DVI ranges from 0.48 to 4.48 m/pixel, with a field of view ranging from 0.45 to 4.4 mm. The images are used to reconstruct the 3D geometry based on image segmentation, voxel generation and complete 3D reconstruction. Figure 47 shows a sample non-woven geometry and the reconstructed solid model.

The finite volume method of Patankar [62] implemented in Fluent code is used to carry out flow simulations through these reconstructed solid fibrous geometries. But

taking several samples of non-woven geometries with varying solid volume fraction they were able to shown the behaviour of permeability in real non-woven structures. Their results are discussed in the next section along with the results generated in this work. Jaganathan et al. showed that for the non-woven structures chosen, which had a layered arrangement of fibers, the behaviour of permeability with solid volume fraction matches closely with the model of Speilman and Goren and also with the model of Davis.

5.2.2 Permeability study of Model Layered Orthogonal Fibrous media

The above literature emphasizes the point that in a layered fibrous porous media, the fiber orientation distribution has little effect on the transverse permeability of the media. This finding would allow for representing real non-woven layered fibrous structures, where the fibers curve and bend within their layer, with a more simple geometry constructed through straight fibers that are either in unidirectional or orthogonal arrangement, for the purpose of modeling the permeability. In the following, we evaluate the layered orthogonal arrangement as a possible way of representing a more complex geometry of non-woven structures. Two orthogonal arrangements are considered i.e. the ordered orthogonal arrangement and the skewed orthogonal arrangement.

The geometries are shown in figure 48. Figure 48a shows the ordered orthogonal arrangement of cylinders. g is the gap between the cylinders of diameter d. The solid volume fraction (n^F) is given as $\frac{\pi d}{4(g+d)}$. Thus by changing the cylinder gap g the solid volume fraction can be changed.

The skewed orthogonal arrangement of cylinders is shown in figure 48b. Here the layers are arranged such that they are skewed as shown in the figure. Thought both ordered and skewed arrangements are approximations of real non-woven structure, the skewed arrangement is slightly more closer to the real media.

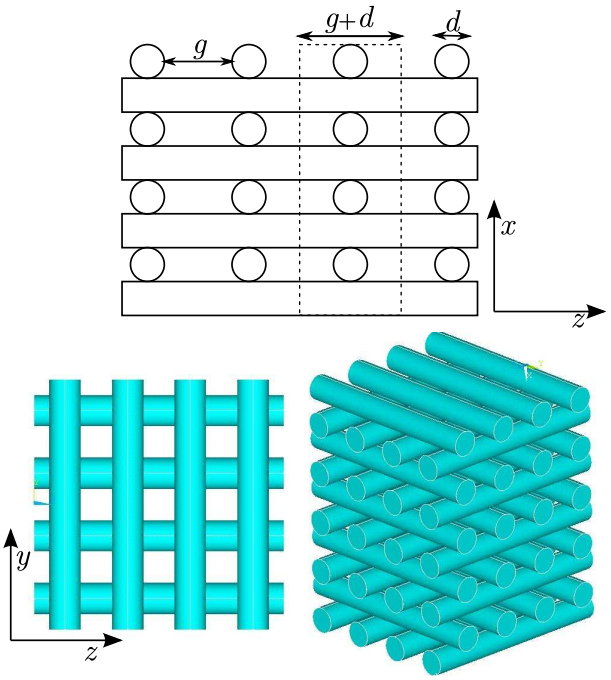

(a) Ordered Orthogonal Arrangement

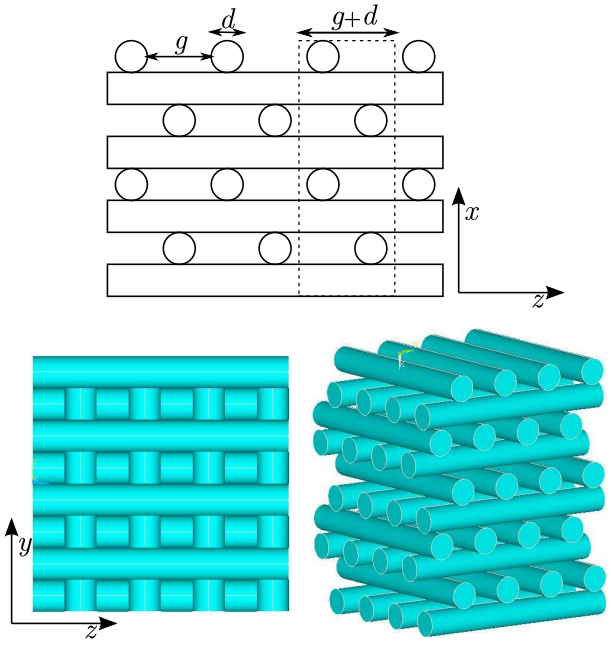

(b) Skewed Orthogonal Arrangement

Figure 48: The two different cylindrical arrangements considered to represent a more complex fibrous geometry like non-wovens, in the aspect of permeability behaviour.

In order to determine the feasibility of using these structures to recover the permeability properties of real felt, it is necessary to determine their permeability behaviour with varying solid volume fraction. In this work, the permeability is calculated using numerical techniques. The lattice-Boltzmann method (LBM) is used to simulate flow through the selected model geometries. The LBM has already been proved to provide accurate results for flow through complex geometries 3.2.

Due to the periodicity in the structure, the geometry necessary to carry out flow simulation can be simplified. The chosen geometry is represented by the dotted line in figure 48.

The 8 cylinder arrangement as shown in figure 35 is used to determine the permeability. Each cylinder has a diameter of 40 lattice units and length depends on the gap g. The fluid domain is chosen so as to provide enough space before and after the geometry to eliminate entrance and outlet to effect the pressure drop calculations. The fluid flows is in the x-direction, the boundary conditions are;

$$\mathbf{v} = V_o\hat{i};\ at\ x = 0; \tag{94}$$

$$\frac{\partial v_x}{\partial x} = \frac{\partial v_y}{\partial x} = \frac{\partial v_z}{\partial x} = 0;\ at\ x = l_c, \tag{95}$$

$$v_{y=0} = v_{y=4R}; \tag{96}$$

$$v_{z=0} = v_{z=4R}; \tag{97}$$

The inlet velocity is varied and the resulting pressure drop is measured. In each case, the simulations are run till a steady state distribution of pressure and velocity values are attained throughout the domain.

Figure 49 shows the behaviour of permeability in skewed orthogonal and ordered orthogonal cylindrical arrangements with varying solid volume fraction. The empirical model of Davis [22] and the analytical model of Speilman and Goren [67] are

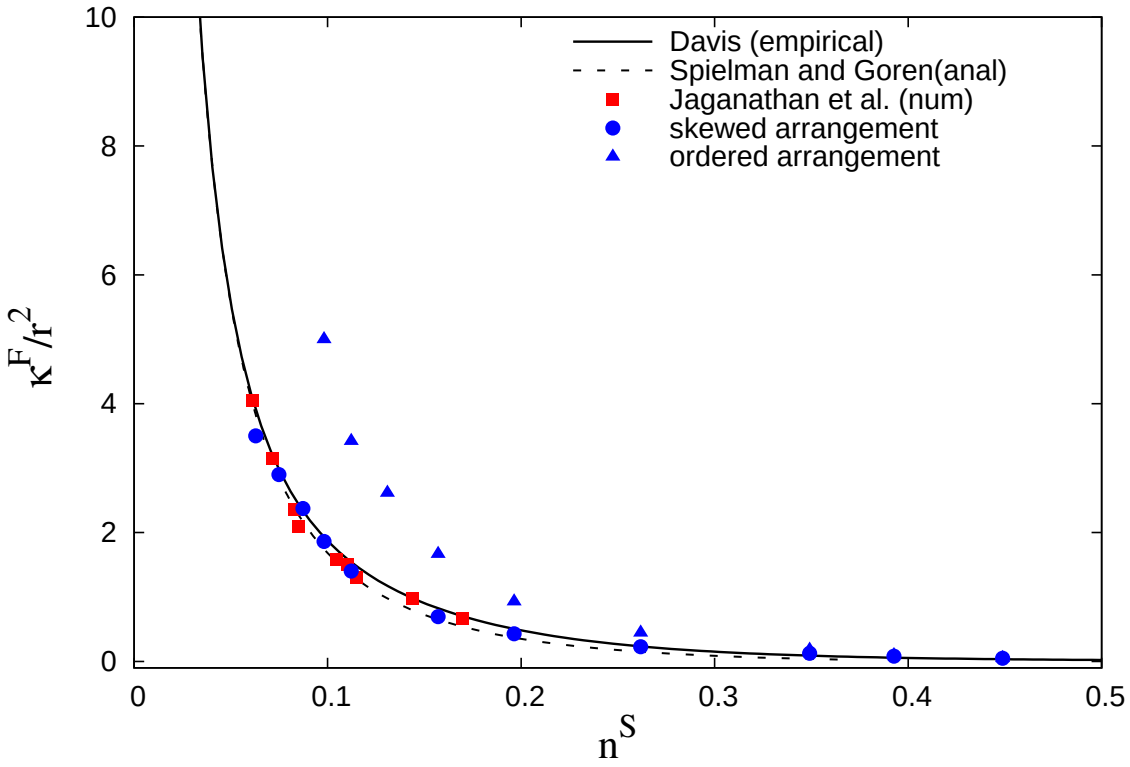

Figure 49: Comparison of permeability of the skewed orthogonal and ordered orthogonal arrangement of cylinders. The empirical model of Davis [22] and the analytical model of Speilman and Goren [67] are provided for reference. Also included in the plot are the numerical simulation results of Jaganathan et al[40] for permeability in real non-woven structures.

provided for reference. Also included in the plot are the numerical simulation results of Jaganathan et al[40] for permeability in real non-woven structures.

The plot shows that the permeability of skewed orthogonal arrangement matches well with the available models and also with real non-woven structures. Comparing this plot with the results of Tahir and Tafreshi figure 46, it can be said that the skewed orthogonal arrangement behaves similar to all the arrangement considered by Tahir and Tafreshi. However the plot shows a different behaviour for the permeability of ordered orthogonal arrangement. It is seen that for $n^S > 0.3$, the permeability behaviour matches with the available models and also with the skewed orthogonal arrangement. As n^S decreases below 0.3, the ordered orthogonal arrangement gives higher permeability values than the models and the skewed arrangement. Further this difference increases for decreasing n^S.

This behaviour of the permeability in ordered orthogonal arrangements lead one to conclude that permeability is not entirely independent of fiber arrangement in layered fibrous media. It appears that permeability is weakly dependent on the surface area normal to the flow direction. However the emphasis here is on the term "weakly". Further investigations need to be performed to completely understand the effect of fiber arrangement in layered fibrous media when the solid volume fraction is low $n^S \approx 0.1$.

5.2.3 Bulk modulus of model layered orthogonal cylindrical arrangements

The above investigations in model layered orthogonally arranged cylindrical strcutures has shown that the skewed orthogonal arrangement behaves close to the real layered fibrous porous media in terms of the relationship between porosity and permeability of the media. Thus it now remains to be seen how the bulk modulus E_b of the skewed orthogonal arrangements behave when compared to real layered fibrous porous media.

There hasn't been much work in developing relations to predict the layer-by-layer bulk modulus of fibrous porous media. Van Wyke [76] developed an analytical expression for the change in solid volume fraction (n^S) due to the applied stress load (T_{zz}). He assumed the fiber deflection to be similar to bending of straigth slender beams and also assumed that the mean contact spacing to be proportional to the reciprocal of material solid volume fraction. The relation between T_{zz} and n^S is given as

$$T_{zz} = C\left((n^S)^3 - (n_o^S)^3\right) \tag{98}$$

where n^S is the solid volume fraction after deformation, n_o^S is the solid volume fraction before deformation and C is a proportionality constanct that depends on the properties of fiber such as the bending rigidity.

Very recently Jaganathan et. al. [41] performed experimental investigations on the morphological changes in nonwoven fibrous materials during compression. Their study consisted of performing compression on real fibrous porous media followed by 3D imaging and analysis. Figure 50 shows the images of fibrous porous media obtained during various compression stages by 3D imaging and subsequent processing. Jaganathan et al. compared the obtained n^S values in the compressed geometries with Van Wyke's model. They found that the variation of n^S with applied stress load T_{zz} matches that of the Van Wyke's model.

In order to determine the behaviour of n^S with applied load T_{zz} in skewed orthogonal arrangements, we compared our results of compression of skewed orthogonal arrangement with Van Wyke's model. The goemetry used for the compression simulations is shown in figure 51.

The boundary condition at the bottom ($z = 0$) is a no-slip, no-displacement condition given as

$$\mathbf{v} = 0; u_z = 0; at\ z = 0; \tag{99}$$

where $\mathbf{v}$ is the fluid velocity vector, $\mathbf{u}$ is solid displacement vector. At the top, an

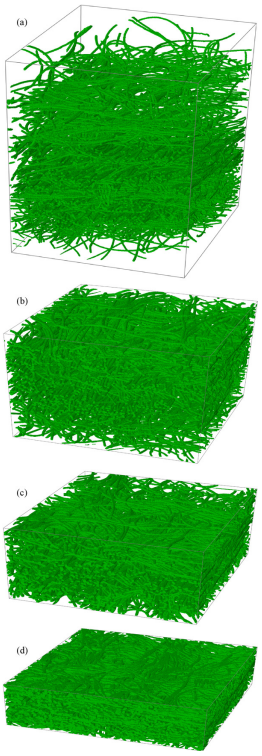

Figure 50: Images of fibrous porous media obtained during various compression stages by 3D imaging and subsequent processing by Jaganathan et. al.

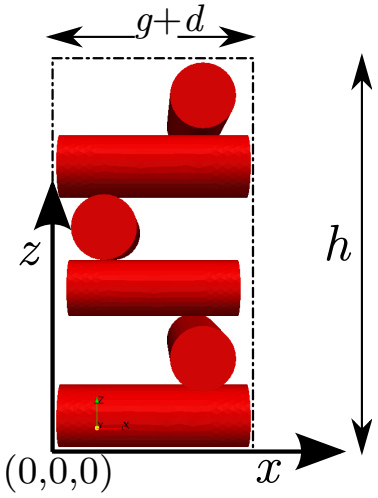

Figure 51: Geometry used to perform compression simulations of skewed orthogonal arrangement of cylinders.

outflow condition is applied on the fluid phase, and a load $f(t)$ is applied on the solid phase; given as,

$$\frac{\partial v_x}{\partial z} = \frac{\partial v_y}{\partial z} = \frac{\partial v_z}{\partial z} = 0; \mathbf{F}(t) = -f(t)\hat{k};\ at\ z = h, \tag{100}$$

where $\mathbf{F}(t)$ is the load vector and h is the height of the column. In this paper we only discuss the response of using a constant load with time. On the four vertical wall, symmetry conditions are applied, given as

$$v_x = 0; u_x = 0; at\ x = 0, g + d; \tag{101}$$

$$v_y = 0; u_y = 0; at\ y = 0, g + d; \tag{102}$$

Figure 52 shows the variation of $(n^S)^3$ with respect to the applied stress load T_{zz}. The simulation data shown in circular data points show a linear behaviour. This agrees well with Van Wyke's model which pridicts that the applied stress load T_{zz} is proportional to the $(n^S)^3$. The plot also shows the results of Jaganathan et. al. and comparison with Van Wyke's model.

Though Van Wyke's model gives a relationship between n^S and T_{zz} it is easy to see that the model provides some guidelines for the variation of bulk modulus E_b in fibrous porous media. This can be seen from the fact that the bulk modulus E_b is a function of T_{zz} and ϵ^* given as $f(T_{zz}, \epsilon^*)$ which can easily be represented as a $f(T_{zz}, n^S)$. Thus validating the compression of skewed orthogonal arrangement with Van Wyke's model confirms that the behaviour of E_b in Van Wyke's model matches that of real fibrous porous media as also confirmed by Jaganathan et. al.

5.2.4 Developing model geometry for real nonwoven felts

Figure 44 shows the solid model of a real nonwoven felt used in paper industry during wet-pressing process. Generally the paper-making felts consists of three distinctive layers of fiber mats. The "base" layer, which forms the base of the felt and gives

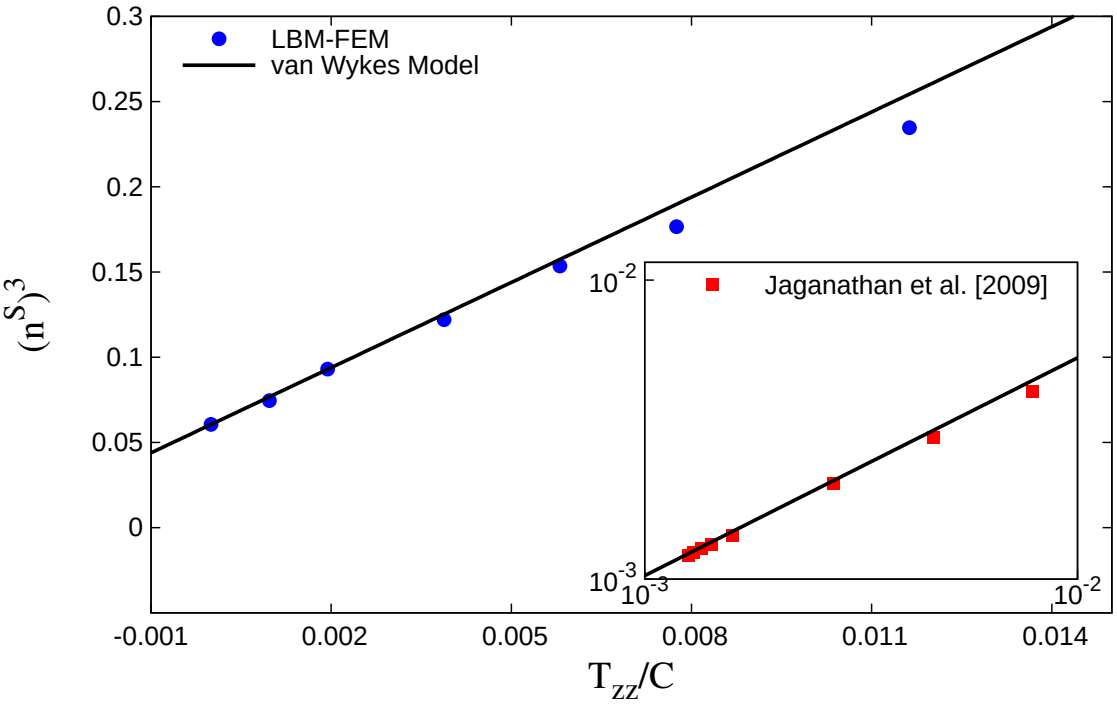

Figure 52: Comparison of variation of n^S and T_{zz} in skewed orthogonal arrangement with Van Wyke's model. Also shown are results provided by Jaganathan et. al. of the variation of n^S with T_{zz} in real fibrous porous media.

it strength and rigidity. The "batt" layer which is layed on top of the base layer and form as an intermediate layer between the base layer and the top layer. Finally, the top layer also called the "protective" layer that consists of very fine fibers and also comprises a tiny part of the total felt thickness. The fiber diameter in each of these layer varies. In order to give strength and rigidity the fibers in base layer have very large diameter. The fibers in the intermediate batt layer are small compared to base layer because they prevent the very fine fibers in the protective layer from penetrating into the base layer. The protective layer comes in contact with the paper during wet-pressing. Thus the protective layer consists of very fine fibers which gives better surface finish to the paper. The thickness of each of these layers depends on the stage in the wet-pressing process where the felt is used.

For the purpose of developing model geometeries of the real nonwoven felts, the geometry as shown in figure 44 can be divided in three regions. Figure shows the three regions that correspond to the base layer, the batt layer and the protective layer. It should be noted that the model geometry is the best approximation of the more complex real felt. The model geometry captures the nonhomogeneity occuring due to the varying fiber diameter however the nonhomogeneity occuring due to the pinning process is not modeled. The pinning process causes fibers in one region to be pushed into a different region at the location where pinning has occured.

For developing the model geometry, information regarding fiber diamter (d_f) and porosity (n_F) in each of the three layers is needed. Obtaining these parameters from X-ray or MRI images is seperate topic of investigation and will not be discussed here. We assumed that this information is available and can be used readily.

As has been show in the previous section the skewed orthogonal arrangement behaves as a real nonwoven fibrous media based on the fact that the n^F-K^F relationship and the n^F-E_b relationship between the two match. Thus we use the skewed orthogonal arrangement of cylinders to represent each of the three layeres that have been

discussed above. In the following we look at how to match these three parameters i.e. n^F, K^F and E_b between the real and the model geometry using the felt geometry shown in figure 44 as an example.

Firstly, we look at the parameters n^F and K^F. As mentioned above it is assumed that variation of n^F along the heigth of the real felt is known. In order to match n^F between the model and real geometries, consider the skewed orthogonal arrangement shown in figure 48b. The fiber diameter d_f and the gap between the fibers g allow for obtaining the right value of porosity n^F as

$$n^f = \frac{\pi d_f^2}{4} \frac{1}{(g+d)d}. \tag{103}$$

It is also known (Spielman & Goren[67], Davis[22], Tahir & Tafreshi [69]) that the permeability K^F of layered fibrous media is only dependent on n^F and the ratio $\frac{d_f^2 \rho^F g}{\mu^F}$. Since n^F is given, the parameters in the ration $\frac{d_f^2 \rho^F g}{\mu^F}$ can be varied to obtain the right K^F. Generally it is convenient to vary μ^F to obtain the right K^F value. From the above two conditions for matching n^F and K^F it is seen that it is not important to choose the exact same value of the fiber diameter as the ral felt geometry. Instead the ratios $\frac{g}{d}$ and $\frac{d_f^2 \rho^F g}{\mu^F}$ should be such that they recover the correct value of n^F and K^F for each layer. Since the fluid and solid properties (μ^F, ρ^F) are going to be constant for the three layeres, this means that in order to obtain the same variation of K^F in the model geometry as the real geometry, the ratio of fiber diameters between two regions should be the same in the model geometry. Thus amoung the independent variables available for developing the model geometry (g, d_f, μ^F and E_b) we have now fixed g, d_f and μ^F.

In regards to the bulk elastic modulus E_b, as mentioned in section 5.2.3 there are not many relations that can predict the variation of E_b based on fiber orientation and fiber diameter. However as shown in section 5.2.3, the skewed orthogonal arrangement provides a good match with the Van Wyke's model, which as also been proved by Jaganathan et. al. [41] to provide a good estimate of the compressibility of layered

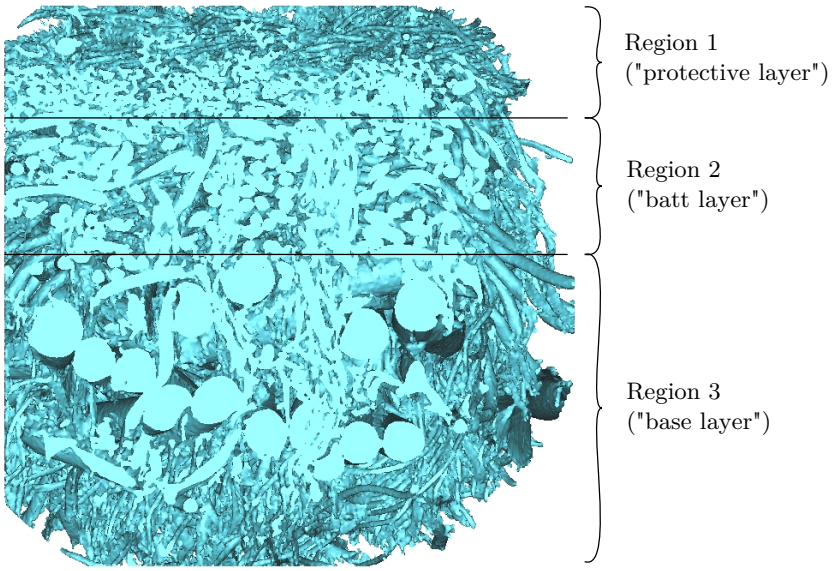

Figure 53: The three regions in a wet-pressing felt. Protective layer consists of very fine fibers at the top of felt for good finishing of paper. The batt layer consist of fiber of intermediate diameter to prevent fine fibers from entering the base layer. The base layer provides strength and rigidity to the felt and consists of fibers with largest diameter.

fibrous porous media. Thus the skewed orthogonal arrangement determined by setting the parameters g, d_f and μ^F based upon matching the parameters n^F and K^F as discussed earlier would be suitable to provide an accurate estimate of the general behaviour of real nonwoven felts during saturate compression.

In order to match the E_b between the real and model geometries, more experimental work needs to be done to obtain better understanding of variation of E_b along the height of the felt geometry.

5.3 Bulk Modulus (E_b) of Orthogonal Cylindrical Arrangement

As seen in subsection 5.2.1, there has been a lot of study in understanding the behaviour of permeability in layered fibrous media. However, there has not been much work done in understanding the behaviour of bulk elastic modulus E_b in such media. In this section, an analytical expression is developed for the bulk elastic modulus of

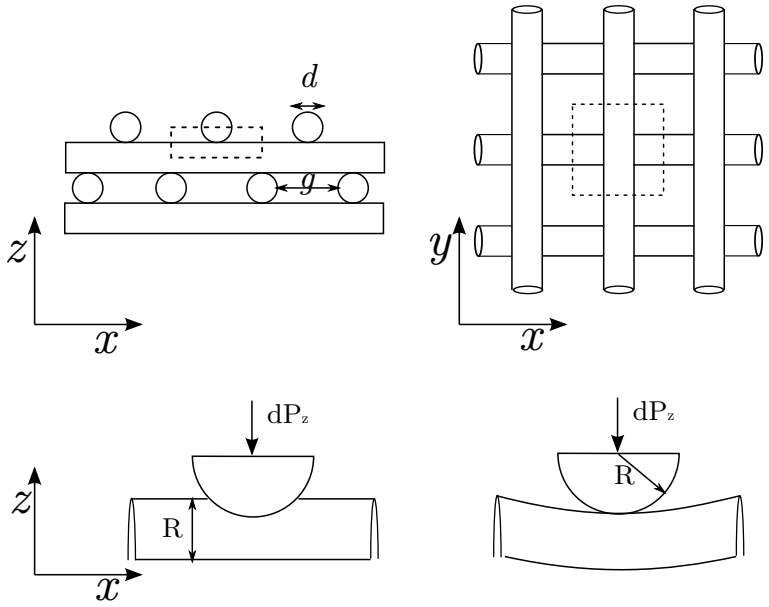

Figure 54: Skewed orthogonal arrangement of cylinder and the two types of deformation occuring when external load is applied.

skewed orthogonal arrangement based on the approximation of small deformations.

5.3.1 Homogeneous skewed orthogonal arrangement

Figure 54 shows a homogeneous orthogonally arrangement of cylinders. Under an external compressive load, the deformation of such arrangements occurs due to two physically distinct phenomenas. The first is due to the "contact" of the fibers and the ensuing deformation near the contact points. The second is due to the "bending" of fibers because of their unsymmetrical nature in the Z-direction.

The bulk modulus of such a cylindrical arrangement can be calculated by considering a unit cell shown in figure 54 as the region within the dotted line. The reason for choosing a unit cell that cuts through the diameter of two cylinder layers is to distinguish between the deformation occurring at various contact points and to choose a domain length which represents the deformations occurring.

In order to calculate the bulk modulus the procedure outlined in subsection 4.2.2, is followed. As mentioned above within the unit cell shown with the dotted lines,

the deformation occurs due to "contact" and "bending". If dP_z is the incremental applied load on the unit cell, then the incremental stress is given as

$$d\sigma_{zz} = \frac{dP_z}{(g+2R)^2}, \tag{104}$$

where R is the radius of the cylinder. The compressive strain $d\varepsilon_{zz}$ is given as

$$d\varepsilon_{zz} = \frac{d\alpha + d\delta}{2R}, \tag{105}$$

where α is the deformation due to fiber-fiber contact and δ is the deformation due to fiber bending. Thus the relationship between instantaneous compressive strain and instantaneous compressive stress is given as

$$d\varepsilon_{zz} = \frac{(g+2R)^2}{2R} C d\sigma_{zz}, \tag{106}$$

where C is the normal compliance given as

$$C = \frac{d\alpha}{dP_z} + \frac{d\delta}{dP_z}. \tag{107}$$

The value of $\frac{d\alpha}{dP_z}$ has already been evaluated in subsection 4.2.2. The effect of bending deformation on the normal compliance is given as

$$\frac{d\delta}{dP_z} = \frac{(g+2R)^3}{192EI}, \tag{108}$$

where E is the Young's Modulus of the material and I is the area moment of inertia given as $\frac{\pi R^4}{4}$. Thus, the instantaneous Bulk Modulus E_b of the cylindrical arrangement shown in figure 54 is given as

$$\frac{1}{E_b} = \frac{(g+2R)^2}{2R}\left[\frac{1}{E^* a} + \frac{(g+2R)^3}{192EI}\right]. \tag{109}$$

5.3.2 Non-homogeneous orthogonal arrangement of cylinders

In a lot of application involving nonwovens, the fibrous porous media may not be homogeneous in the compression direction. The non-homogeneity in the porous media

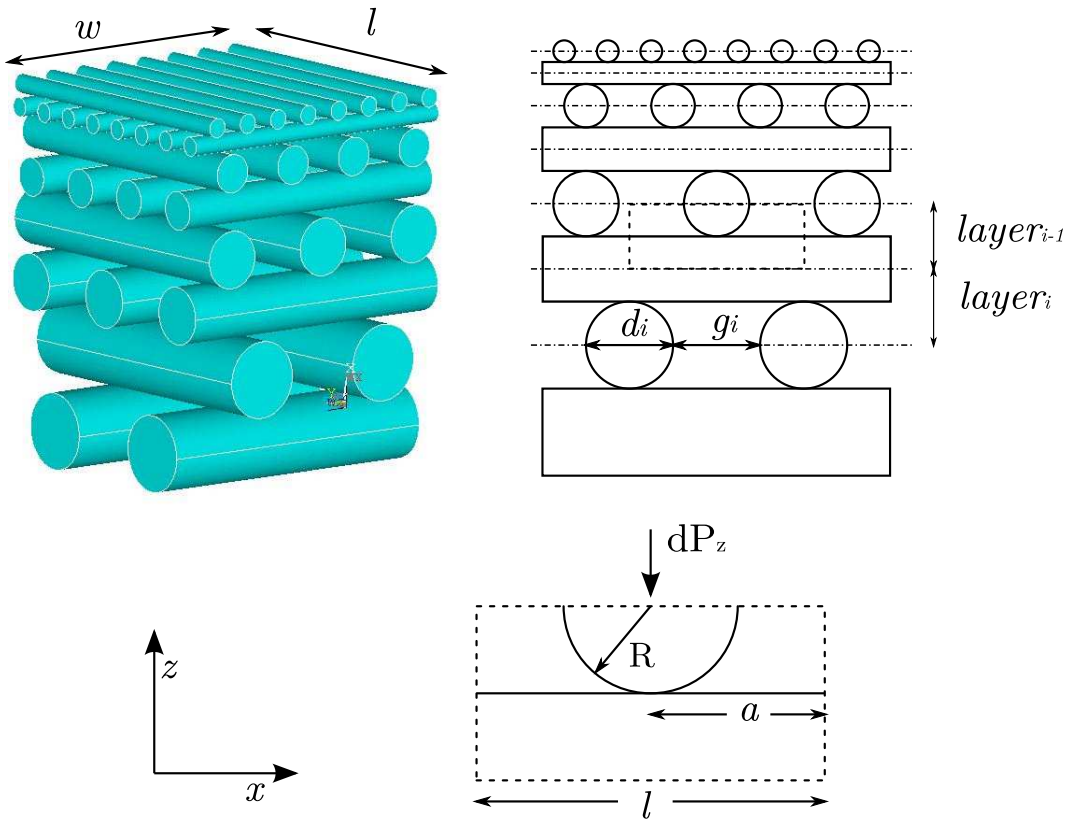

Figure 55: Non-homogeneous fibrous porous media constructed through the use of different diameter cylinders along the height of the porous media.

is induced due to variations in porosity, permeability or bulk modulus. An easy way to control the non-homogeneity of the porous media is to include fibers to various diameters in the construction of the fibrous porous media. Figure 55 shows a simplified representation of a nonhomogeneous fibrous porous media constructed using varying cylinder diameter along the height of the media.

Evaluating the bulk modulus of such an arrangement is a more complex problem. Due to the varying, cylinder diameter and the location of the contact points in each layer, both the incremental contact deformation $d\alpha$ and incremental bending deformation $d\delta$ vary with each layer, for the same incremental load dP_z. Thus the bulk modulus of the arrangement based on small deformation theory varies along the height of the arrangement.

In order to ease in the identification of the source of deformation the geometry

is divided into layers as shown in the figure 55. The bulk modulus is assumed to be constant for each layer and thus the bulk modulus is evaluated for each layers as described in the above section.

For the problem of determining the bulk modulus along the height of a nonhomogeneous orthogonal cylindrical arrangement, the independent parameters are the width w and depth l of the arrangement, the number of layers s in the arrangement, the total applied load P_z, the diameter of the cylinders in each arrangement d_i, the gap between the cylinders in each layer g_i, the initial offset from the x or the y axis of the first cylinders in each layer δl_i.

For each layer, the number of contact points are determined and thus the total deformation due to contact of cylinders. Further for each the possibility of "bending" type of deformation is evaluated based on the the position of contacts in the next layer. If the possibility of "bending" type of deformation exits its values is determined based on the beam theory as described above.

Figure 56 shows the variation of the bulk elastic modulus ration E_b/E for the geometry shown in figure figure 55. On the abscissa, 0 represents the top of the geometry and 40 represents the bottom. It is seen that the bulk modulus has variation from layer-to-layer in the top half of the geometry and remains mostly constant in the bottom half. This because, in the top half the fibers are thin and the spacing between the fibers is such that there is a large contribution from the bending type of deformation to the bulk elastic modulus. In the bottom half as the fiber diameter increases, the bending type of deformation decreases and bulk modulus is only due to deformation occuring as a result of fiber-fiber contact.

5.4 Effect of fiber diameter

The development of an analytical expression for the bulk elastic modulus of the developed model cylindrical arrangements, along with the expressions for predicting

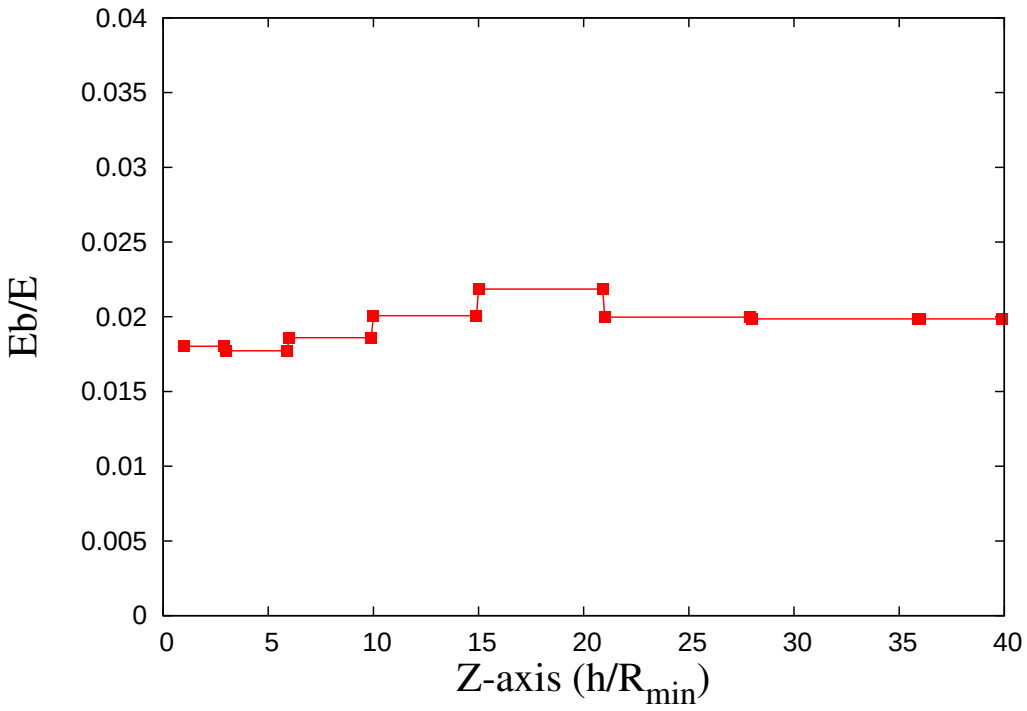

Figure 56: Variation in bulk elastic modulus in compressive direction (along the height)for a sample geometry.

permeability (Spielman & Goren [67], Davis[22]), it is now possible to comment on the deformational behaviour of such arrangements under the influence of external loading. These analytical tools along with the developed numerical tool (LBM-FEM method) can be used to investigate the effect of fiber diameter on the deformational behaviour of orthogonal cylindrical arrangements. For instance to answer questions such as how does the deformational behaviour of two geometries with same porosity but different fiber diameter differ.

In this section, the analytical tools and the numerical tools are used to make predictions and then perform simulations to understand the effect of fiber diameter on the deformation of model layered fibrous porous media.

Table 7: Values of parameters n^S, K^F and E_b for a few skewed orthogonal arrangement of geometries selected.

$d(\times 10^{-4}m)$	$g(\times 10^{-4}m)$	n^S	$K^F(m/s)$	E_b/E
20	20	0.393	0.00014	0.0199
40	40	0.393	0.00058	0.0199
50	50	0.393	0.00089	0.0199
40	50	0.350	0.00088	0.0170
40	60	0.314	0.00127	0.0123
40	80	0.261	0.00228	0.0081

5.4.1 Homogeneous skewed orthogonal arrangements

As a first case we look at the homogeneous skewed orthogonal arrangements to understand the effect of fiber diameter. Table shows the values of the parameters n^S, K^F and E_b for a few homogeneous skewed orthogonal arrangements chosen. Also shown in the table are the value of fiber diamater d and the gap g as shown in figure 55.

The table shows that for homogeneous skewed orthogonal arrangement of cylinders, the value of bulk elastic modulus (E_b) is only dependent on the solid volume fraction (n^S) and does not depend on the fiber diameter. However the permeability K^F does depend on the fiber diameter, which as also been shown in literature where the permeability κ^F is said to be dependent on the diameter as $\kappa^F \approx d^2$.

The effect of fiber diameter on the E_b can also be understood through the analytical expression developed in the previous section. The analytical expression when written in terms of the applied stress T_{zz} is given as

$$\frac{1}{E_b} = (\phi+1)^2 \left[\left(\frac{1}{3(E^*)^2 T_{zz}} \right)^{1/3} + \frac{(\phi+1)^3}{3\pi E} \right], \tag{110}$$

where the parameter $\phi = \frac{g}{d}$ essentially gives the solid volume fraction. Thus it is seen that fiber diameter has no impact on E_b as long as n^F is kept constant. Thus E_b in homogneous skewed orthogonal arrangements is only a function of n^F.

In order to investigate this further we use three different geometries of skewed orthogonal arrangements with different combination of fiber diameter and gap. These goemetries are used to perform compression simulations using the LBM-FEM method.

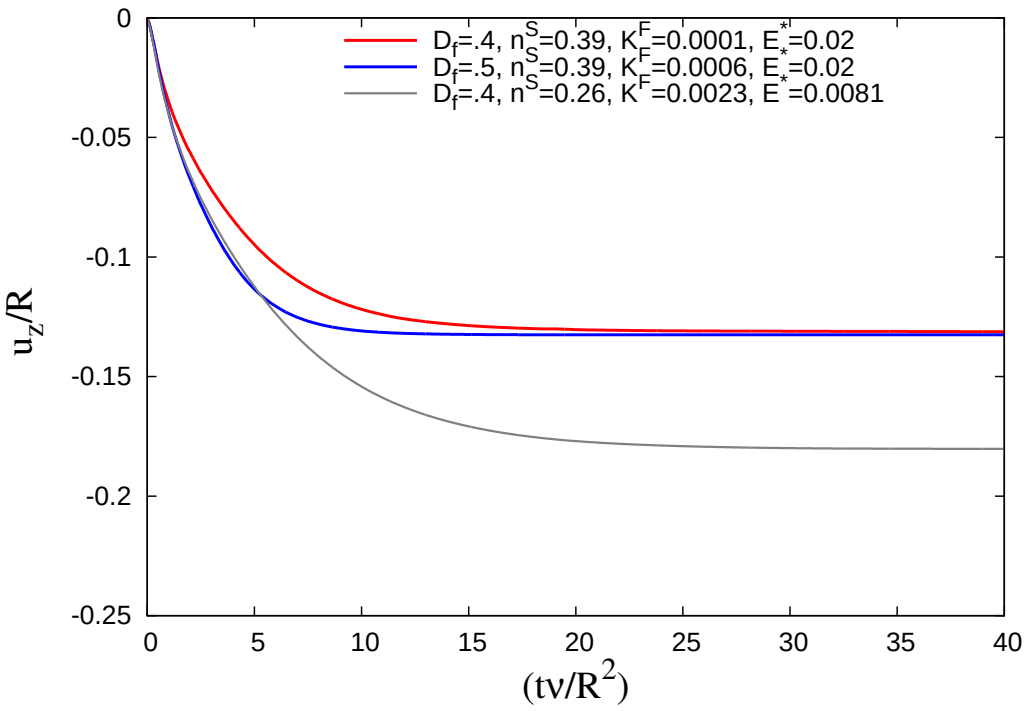

Figure 57: Deformation response of three skewed orthogonal arrangement of cylinders for the same applied compressive load.

Figure 57 shows the deformation response of the three selected geometries. The blue and red curves shows the deformational response of geometries with different fiber diameter but same n^S. The fiber diameter for red curve is smaller than the blue curve. Thus, the permeability of blue curve is higher than the red curve, however their E_b's are the same. The deformational response clearly shows these characteristics i.e. the blue curve deforms faster than the red curve, but the total deformation of the two geometries is the same.

The grey curve shows the deformational behaviour of a geometry that consists of fibers of diameter same as the red curve but with lower n^F. This results in a lower E_b and also a lower K^F. Again these characteristics are clearly seen as the geometry deforms faster and also to a larger extent than the other two geometries.

These numerical simulation results clearly illustrate the facts that E_b effects the extent of deformation and for a constant E_b, K^F determines the rate of deformation.

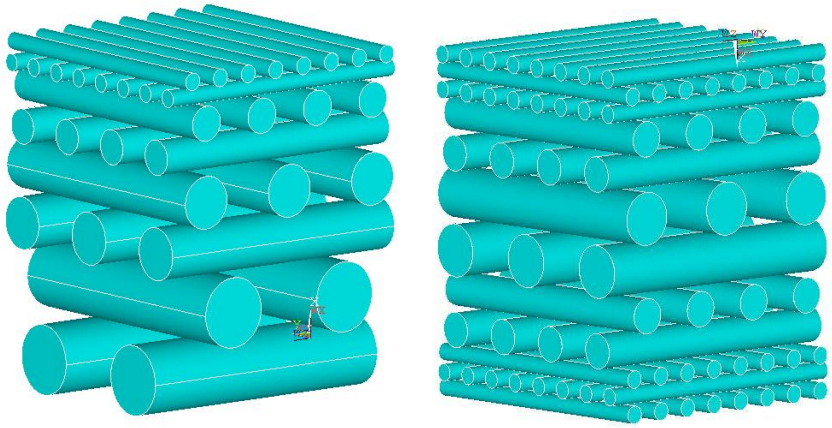

(a) Geometry "nh1" (b) Geometry "nh2"

Figure 58: Two different orthogonal arrangements of cylinders where the cylinder diameter varies along the the height of the structure.

This is another example of unique abilities of the LBM-FEM method in performing micromechanical investigations on saturated deformable porous media.

5.4.2 Nonhomogeneous orthogonal arrangements

Figure 58 shows two different orthogonal arrangement of cylinders with varying cylinder diameter. In these arrangement the porosity of the structure is maintained constant at $\epsilon = 0.39$. In the case of figure 58a, the diameters of the top two layers of cylinders are 20 lattice units followed by 40 lattice units for the next two and 60 lattice units for the next 2 and 80 lattice units for the last two. In figure 58b the first three layers of cylinders have diameters of 20 lattice units, followed by two layers of 40 lattice units diameter cylinders and the next two are 60 lattice units followed by two 40 units and then 3 20 unit diameter cylinders at the end.

Figure 59 shows the variation in the bulk modulus of two different orthogonal cylindrical arrangement with varying cylinder diameter. In "nh1" the cylinder diameter increases from top to bottom, while in "nh2" the cylinder diameter increases from top to the middle and then decreases from middle to the end.

In "nh1" it is seen that there is some variation in the bulk modulus of the top

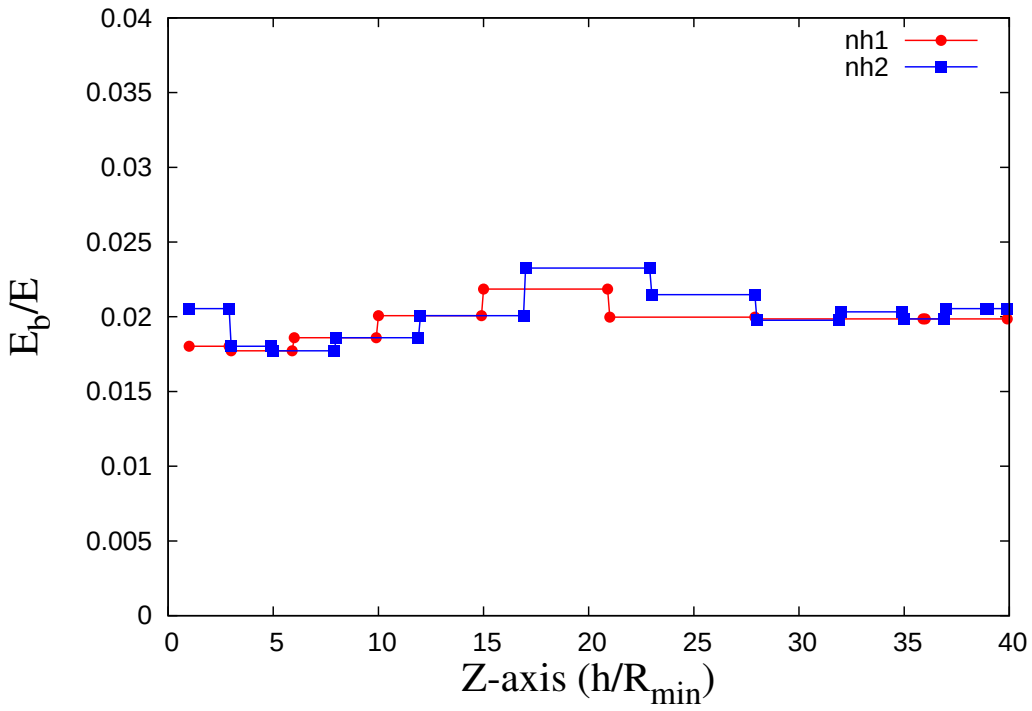

Figure 59: Variation in the bulk modulus in nonhomogeneous ordered orthogonal arrangement of cylinders "nh1" and "nh2".

layers, but the bulk modulus of the lower layers does not vary much. This may be because the fiber diameter of the two layers is half of that of the next two. This large variation allows the fibers on the top to be more skewed thus increasing the "bending" type of deformation in these arrangements. In the later layers due to the relatively small difference in the diameters the there is not much sweetness in the arrangements and thus relatively less bending type of deformation.

The variation in bulk elastic modulus of "nh2" is not much different from that of "nh1". Just as in "nh1" the bulk modulus of "nh2" also varies near the top of the structure. Towards the center and the bottom of the structure the bulk modulus does not change much. Also the plot show that the bulk modulus of "nh2" is slightly higher than "nh1" near the center of the structure.

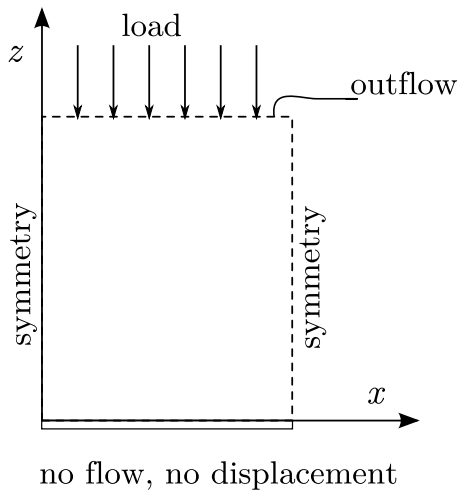

Figure 60: Loading and boundary conditions imposed on the model cylindrical structure for a deformational analysis.

In order to understand the effect of the variation in bulk modulus on the deformational behaviour of the orthogonal structure, direct numerical simulations of instantaneous compression of the saturated cylindrical structure were conducted. The geometry "nh1" and "nh2" discussed in the previous section were used for conducting the deformational analysis.

The goal here was to analyze the effect of variation in the fiber diameter on the deformational response of these model orthogonal layered cylindrical structures. It is seen from the above analysis on the bulk elastic modulus that this property does not change much between the two structure. nh2 showing a slightly higher bulk modulus in the middle than nh1.

Further the two structures have the same behaviour in porosity or solid volume fraction along the structure height. The permeability of the two structures do change drastically along the height. However, due to the fact that the outflow boundary is at the top of the structure, where the two structures have the same cylindrical arrangement, we predict that the effect of permeability of the deformational behaviour of the two structures should be the same.

The loading and boundary conditions imposed on the model nonhomogeneous

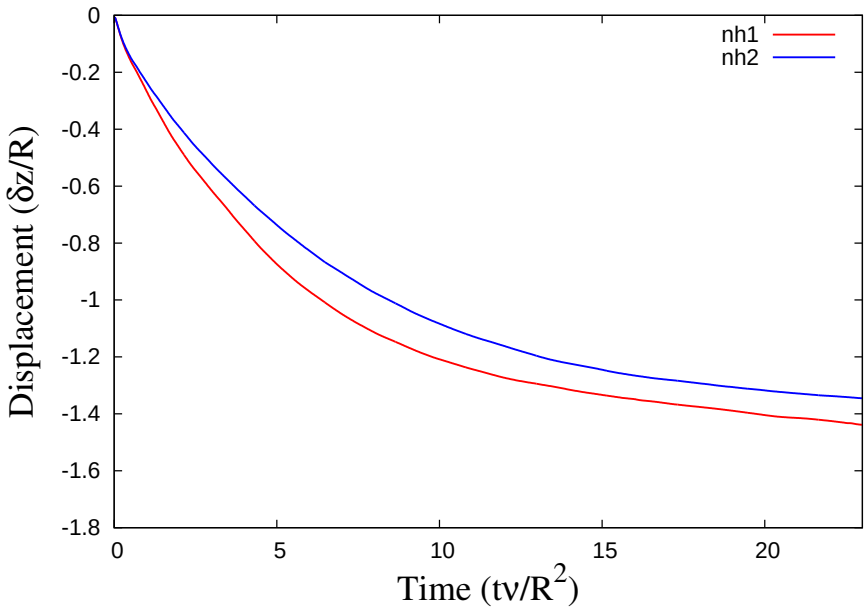

Figure 61: Displacement response of the nonhomogeneous orthogonal cylindrical arrangements of "nh1" and "nh2".

cylindrical structures in orthogonal arrangement are similar to those applied on model porous structures discussed in section chapter 4. Figure 60 shows the schematic of same loading and boundary conditions.

5.4.3 Behaviour of model nonhomogeneous orthogonal cylindrical structures

Figure 61 shows the displacement of the nonhomogeneous orthogonal cylindrical arrangements of "nh1" and "nh2". It is seen that there is not much difference between the displacement response of both the geometries, with a maximum difference of 6%. This result is an indication of the fact that the cylinder diameter itself does not have much effect on the bulk elastic modulus and thus on the deformational behaviour of the fibrous porous media. The layer-to-layer arrangement is a more important factor which can effect the bulk elastic modulus through increase in the "bending" contribution of the fibers.

As predicted the large variation in the permeability of the two arrangements along

the height does not correspond to a similar variation in deformational behaviour, due to the fact that the outflow condition is at the top where the permeability of the both arrangement are same.

CHAPTER VI

CONSTITUTIVE RELATIONS

As described in the previous chapter, there have been numerous studies investigating the effect of porosity on the permeability in rigid porous media. For granular porous media the popular Kozeny-Carmen relation is widely acknowledged as a suitable model [20]. In the case of fibrous porous media the relations provided by [67, 22] and [36] hold true for a wide range of porosity values. From the differences in the permeability-porosity relation for granular media and fibrous media, it is clear that the microstructure of the porous media also has an effects on the permeability apart from the widely acknowledged parameters such as the specific surface area s and tortuosity τ.

In the case of deformable porous media the deformation of the media causes changes in both the microstructure and the porosity. Understanding the effect of deformation on the permeability can lead to better prediction of the permeability-porosity model in such media. This is important, for instance in homogenization based techniques such as the theory of porous media [25] which require information about constitutive relationships such as that between permeability and porosity in order to obtain closure of the problem.

In the following direct numerical simulations based on the hybrid lattice Boltzmann and finite element method have been used to investigate the behaviour of permeability during deformation. Model porous media made of spheres and cylinders in regular arrangements are used. The porous geometry is subjected to compressive loading to simulate deformation. Subsequently the deformed geometry is used to

perform flow simulations using lattice Boltzmann method to determine its permeability. These investigations have given new insights into the behaviour of permeability during the deformation of a porous media.

6.1 Granular Media

The investigations on the effect of deformation on permeability in granular media have been motivated by the need in soil mechanics to understand the properties of soil during deformation. The Kozeny-Carmen relations are still used with small modifications based on the type of soil sample used.

Model porous media made of spheres in a simple cubic arrangement is used as the first case. Due to the symmetric nature of the simple cubic arrangement, the computational domain can be simplified as shown in figure 62. A compressive load is applied to cause deformation of the geometry. In some cases the compressive load varies with time while in the others the compressive load is applied in stages, where in each stage a given load is applied till the geometry reaches a steady state and then more load applied. The boundary conditions applied to the fluid and solid phase are given below.

The boundary condition at the bottom ($z = 0$) is a no-slip, no-displacement condition given as where $\mathbf{v}$ is the fluid velocity vector, $\mathbf{u}$ is solid displacement vector. At the top, an outflow condition is applied on the fluid phase, and a load $f(t)$ is applied on the solid phase; given as,

$$\frac{\partial v_x}{\partial z} = \frac{\partial v_y}{\partial z} = \frac{\partial v_z}{\partial z} = 0; \mathbf{F}(t) = -f(t)\hat{k};\ at\ z = h, \tag{111}$$

where $\mathbf{F}(t)$ is the load vector and h is the height of the column. Each sphere has a diameter of 40 lattice units. The parameter l_{fea} is chosen to be consistent with other simulations performed and is thus set to 4. On the four vertical wall, symmetry conditions are applied, given as

$$v_x = 0; u_x = 0; at\ x = 0, 2R; \tag{112}$$

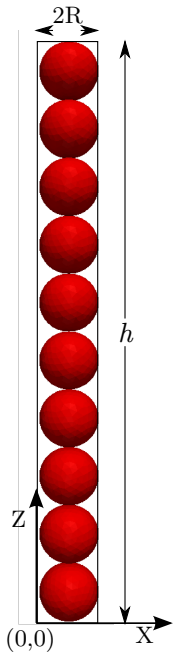

Figure 62: 10 spheres stacked vertically in a column of fluid, representing a simple cubic arrangement. The dotted line represents the simulation domain.

$$v_y = 0; u_y = 0; at\ y = 0, 2R; \tag{113}$$

where $2R$ is the diameter of the sphere and width of the domain in x and y directions.

The initial conditions are given as

$$\mathbf{v}(\mathbf{x}, 0) = \mathbf{0}; \tag{114}$$

$$\mathbf{u}(\mathbf{x}, 0) = \mathbf{0}; \tag{115}$$

where $\mathbf{x}$ is the position vector.

Figure 63 shows the average displacement of the top surface of the spheres in simple cubic arrangement. This displacement behaviour is the result of a stepped loading condition as described above. A given load is applied and the geometry is allowed to reach a steady state represented by the regions where the displacement curve is horizontal and flat. Upon reaching steady state the load is increased and the geometry is again allowed to reach a steady state. At each stage when the geometry

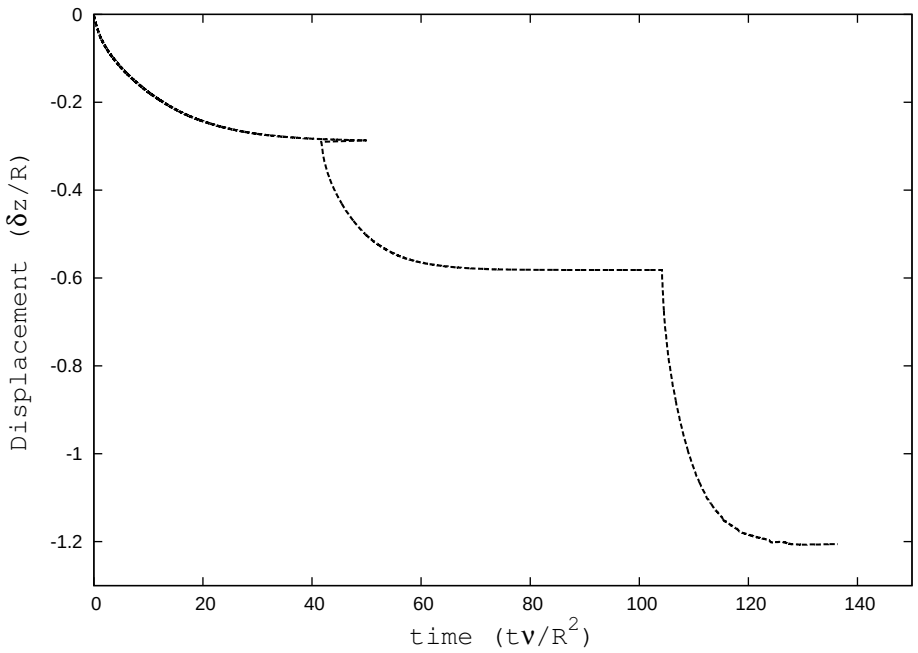

Figure 63: Average displacement of the top surface of spheres in simple cubic arrangement. The behaviour of displacement is the result of application of stepped loading condition.

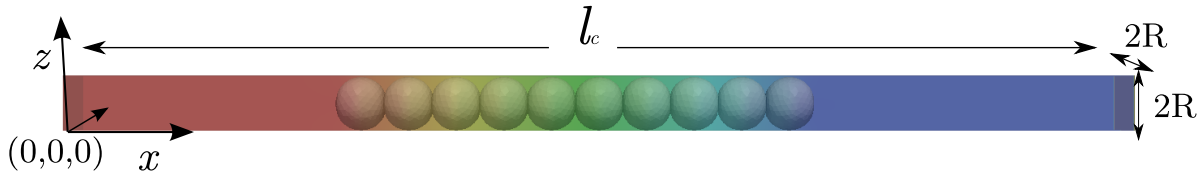

Figure 64: Geometry and domain setup for performing flow calculations to determine permeability.

reaches steady state the information of the geometry is stored for a flow analysis to determine the permeability of the deformed geometry.

In order to determine the permeability of the deformed geometry numerical simulations of flow through the geometry are carried out. The lattice Boltzmann method is used to perform the flow simulations. Figure 64 shows the geometry and domain setup for one of the flow simulations. Each cylinder has a diameter of 40 lattice units and length of 80 lattice units. A fluid domain of 820x40x40 lattice units is used in these calculations. This length of the domain provides enough space before and after

the geometry to eliminate entrance and outlet to effect the pressure drop calculations. The fluid flows in the x-direction, the boundary conditions are;

$$\mathbf{v} = V_o\hat{i};\ at\ x = 0; \tag{116}$$

$$\frac{\partial v_x}{\partial x} = \frac{\partial v_y}{\partial x} = \frac{\partial v_z}{\partial x} = 0;\ at\ x = l_c, \tag{117}$$

$$v_y = 0;\ at\ y = 0, 2R; \tag{118}$$

$$v_z = 0;\ at\ z = 0, 2R; \tag{119}$$

where V_o is the velocity of fluid at inlet, R is the radius of each sphere and l_c is the length of the domain.

Figure 65, shows the variation of permeability with deformation in the case of the spheres in simple cubic arrangement. Permeability is shows with respect to porosity in order to compare existing models that predict the behaviour during deformation. Here the Kozeny-Carmen relation is used to compare with the numerical simulation results. The particular form of the Kozeny-Carmen relation used is given in equation 63. The plot shows very different behaviour of the permeability with porosity during deformation between the numerical simulation results and the Kozeny-Carmen relation. The analytical relation shows a high gradient in the decrease in permeability with change in porosity while the numerical results show an almost linear relation where the permeability still decreases with porosity.

The reason for this difference can be attributed to the fact that the numerical simulations carried out in this research work mainly look in the behaviour of permeability due to the deformation of the solid structure. This is in contrast to the analytical model which approximates the porous media as a tube bundle and change in porosity to correspond to the change in the tube diameter. The analytical model would work well for problems that involve more movement in the geometry and less

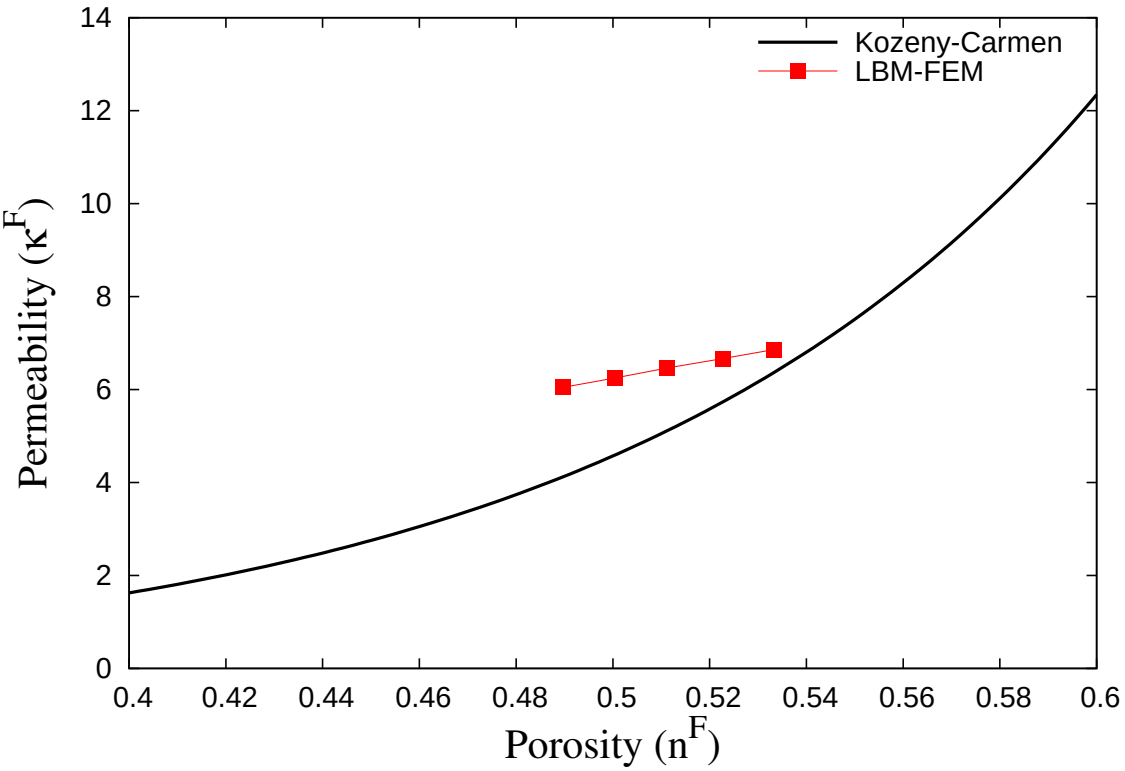

Figure 65: Variation of permeability with porosity during the compression of model porous media made up of spheres. The data is compared to the Kozeny-Carmen relationship.

deformation such as soil. During the compression of saturated soil the water in between the sand particle is extracted thus causing the particles to come closer with negligible deformation of the particles themselves. However under extreme compressive loading there may be considerable deformation of the solid structure. These kind of situations more commonly occur during processes such as wet-pressing, where very high loads are applied on the felt+paper structure to remove water.

6.2 Fibrous Media

In the case of fibrous porous media the need in paper industry has often driven the research. Lindsay and Brady [53, 54] studied the change in the permeability of various pulps during the compression process. Vomhoff [72] also performed similar

studies and found that the permeability increases with decreasing basis weight, the phenomena is called the "Basis weight effect".

More recently Koivu et al. [48] investigated these parameters using experimental and numerical methods. The fibrous materials they used were wet pressing felt, cardboard and newsprint. They compared their results with the analytical results of Hapel [35] and the correlation provided by Brundrett [18]. Hapel's correlation for the non-dimensional intrinsic permeability κ^F is given as

$$\kappa^F = \frac{1}{8n^S}\left(-\ln n^S + \frac{n^S - 1}{n^S + 1}\right), \tag{120}$$

and Brundrett's correlation is given as

$$\kappa^F = k_1 \frac{(n^F)^2}{1 - (n^F)^2}, \tag{121}$$

where k_1 is a constant. They found that Brundrett's correlation matched with the experimental data better than the Hapel's correlation. However no information has been provided about constant k_1, which may have been used as a fitting paramter. They estimate that the maximum total error in their experimental results to be 35%.

In order to investigate the effect of deformation in fibrous porous media, the model fibrous porous media as discussed in section 5.2.2, consisting of skewed orthogonal arrangement of cylinders are used. As discussed in the section 5.2.2, the skewed orthogonal structure is very similar to a real layered fibrous structure, in terms of the behaviour of permeability with porosity. This is the primary reason for choosing this structure to evaluated the effect of permeability with deformation.

The geometry shown in figure represents a periodic structure that can be used to develop a skewed orthogonal arrangement by repeating the structure in x and y direction. The figure also shows the boundary of the domain, on which pseudo-periodic conditions are applied, which are given as

At the bottom ($z = 0$) is a no-slip, no-displacement condition given as

$$\mathbf{v} = 0; u_z = 0; at\ z = 0; \tag{122}$$

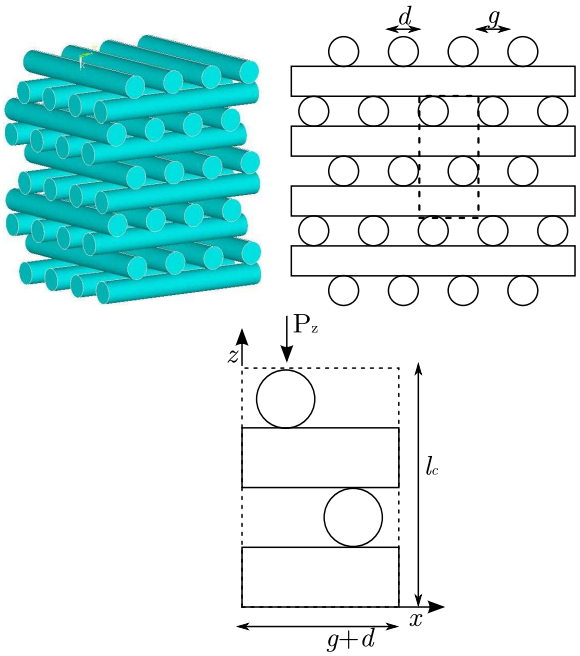

Figure 66: A periodic structure of skewed orthogonal arrangement of cylinders used to in the simulation of compression to understand the behaviour of permeability with compression in fibrous porous media.

where $\mathbf{v}$ is the fluid velocity vector, $\mathbf{u}$ is solid displacement vector. At the top, an outflow condition is applied on the fluid phase, and a load $f(t)$ is applied on the solid phase; given as,

$$\frac{\partial v_x}{\partial z} = \frac{\partial v_y}{\partial z} = \frac{\partial v_z}{\partial z} = 0; \mathbf{F}(t) = -f(t)\hat{k};\ at\ z = h, \tag{123}$$

where $\mathbf{F}(t)$ is the load vector and l_c is the height of the column.

$$v_x = 0; u_x = 0; at\ x = 0, g + d; \tag{124}$$

$$v_y = 0; u_y = 0; at\ y = 0, g + d; \tag{125}$$

Figure 67 shows the original geometry and deformed geometry after the application of a compressive load. The undeformed structure is very porous with a porosity of 0.7382. The completely deformed configuration has a porosity of 0.5367. A number of semi-deformed configurations which lie in between the undeformed and completely deformed configurations were also obtained. These geometries were used in a flow analysis to determine the pressure drop across the geometry in the z-direction.

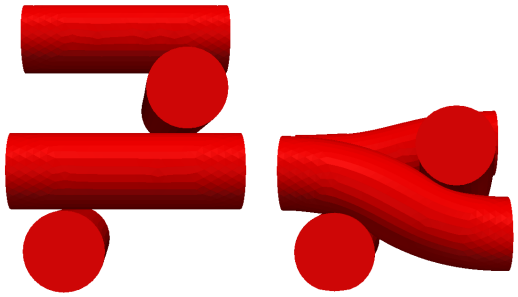

(a) Undeformed (b) Deformed

Figure 67: Undeformed and deformed configuration of a periodic structure representing the skewed orthogonal arrangement of cylinders. These geometries have been subsequently used to determine permeability using numerical flow analysis.

The results of the permeability analysis during compression of a model fibrous porous media area shown in figure 68. The plot shows the analytic model of Hapel [35] along with the empirical model proposed by Davis [22] for comparison. Also seen in the plot are the experimental data given by Koivu et. al [48] for the variation of permeability during compression of a wet pressing felt. Although the experimental data of Koivu et. al is in the low porosity region, it is provided as a reference for comparison.

It is seen that the permeability data from the LBM-FEM simulations of the deformation of the model porous media compares well with the analytical models and the also the experimental data. The minimum porosity achieved during these compression simulations is 0.5367 due to the limitations imposed by the contact model and the linear finite element model on the amount of deformation.

The good match between the numerical simulations and the analytical and experimental data shows that the analytical model do capture all the pertinent physics involved in the deformation of fibrous porous media. Also unlike the case of spheres in a simple cubic arrangement, here the cylinders in a skewed orthogonal arrangement allow for a larger deformation and higher change in porosity than the spheres. Also it is seen from the figure 67 that the deformation causes large changes in the geometric structure and thus large changes in the flow paths.

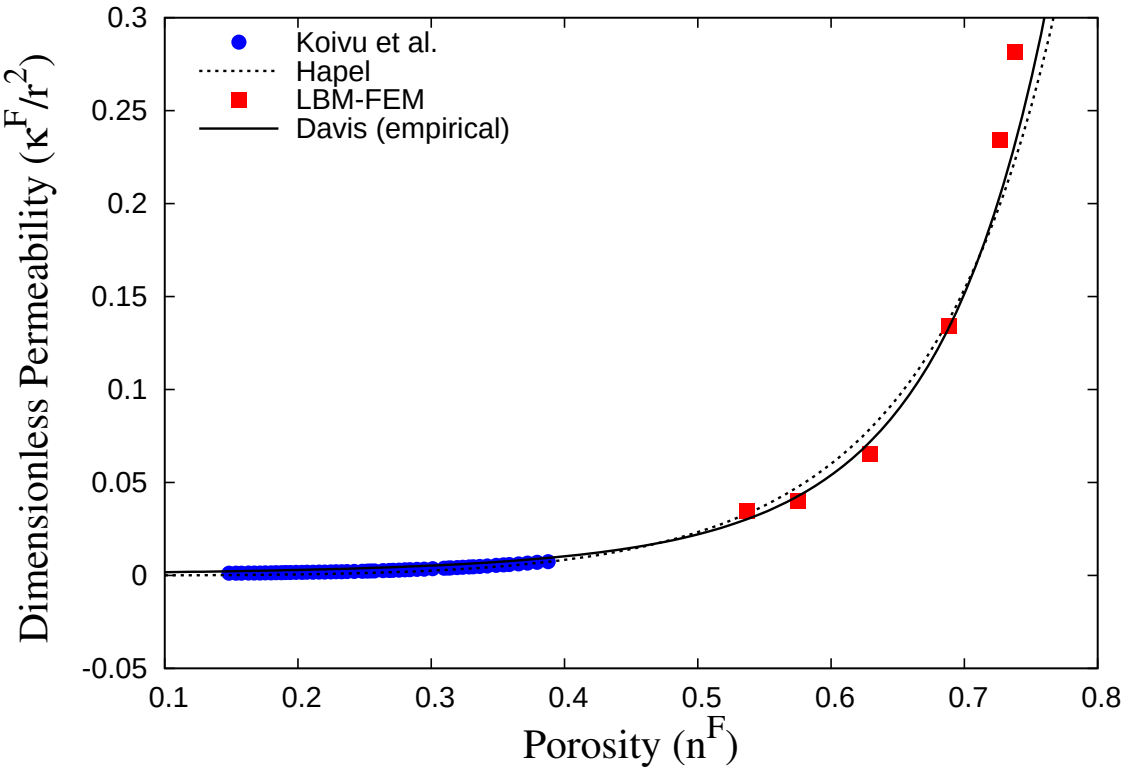

Figure 68: Comparison of experimental data by Koivu et al [48] for the variation of permeability with compression in a wet pressing felt with models by Hapel [35] and Davis [22].

CHAPTER VII

CONCLUSIONS AND FUTURE RECOMMENDATIONS

7.1 Conclusions

The existing numerical techniques to model saturated deformable porous media, such as the Biot's theory or the Theory of Porous Media, are based on homogenization theory. Such macromechanical approaches excludes any consideration of microstructure and thus do not allow investigations into constitutive relations such as the permeability-porosity relations or the bulk Modulus-porosity relations during compression of the media.

To address this need , a robust and scalable numerical method based on a coupled lattice-Boltzmann and finite element method has been developed for direct numerical simulations of saturated deformable porous media under external loading conditions. The lattice Boltzmann method provides efficiency in fluid calculation and in the implementation of no-slip condition on the solid surface through the "simple-bounce-back" scheme. The deformations are approximated as linear elastic in order to reduce the computational demand and solve for displacements in complex geometries. One of the unique features of this numerical method is the use of distributed computing, which allows for simulating fluid-structure interaction in complex geometries with high temporal and spatial resolution in a realistic time frame. A domain-decomposition technique has been used to parallelize the code, using separate ranks for the fluid phase (fluid-ranks) and solid phase (solid-ranks). The method has been bench-marked for scalability and speedup on up to 1024 processors. The results show that reducing the communication within the solid-ranks for the finite element method calculations has a significant effect on the efficiency of the code. Thus it is important to reduce the

finite element edge intersections during partitioning the finite element mesh.

The method has been tested for accuracy and robustness against sample problems, details can be found in Khan and Aidun[47]. Particularly, the contact model implemented in the method was tested against the analytical model presented by Hertz. The results show that the implemented contact model accurately predicts the deformation in the small strain limit. The accuracy increases with incresing mesh resolution. These results show that the LBM-FEM method for direct numerical simulation of saturated deformable porous media will provide accurate results in the small deformation limit and may underpredict the deformation as the load and deformation increases for a given mesh resolution.

Model porous media, approximated using regular arrangements of spheres or cylinders, are used to study the deformation behaviour. It is found that for $Ca, Re, \epsilon^* \ll 1$ the deformational response obtained through the direct numerical simulation of the model porous media using LBM-FEM method matches that with real porous media having the same n^F, K^F and E_b values as the model porous media. Thus it is seen that these parameters can be considered as similarity parameters. These parameters can be used develop model geometries which will represent more complex real geometries and used for a deformational analysis instead of the real geometries. This would lead to tremendous decrease in the meshing and computational time at the same time the exact deformational behaviour can be captured

The effect of mesh resolution is tested using two different mesh resolutions. There was no significant difference between the results with the results varying by only 3%. The reason for such small increase in the accuracy of the results can be attributed to the fact that the deformations were very small in these simulations. As seen in figure 21 for small deformation there is not much difference in the deformation using the implemented contact model. It is important to note here that no open parameters were used to match simulation results to experimental or analytical results, thus it

captures all the pertinent physics accurately. The study also shows that the average bulk elastic modulus calculated based on small strain theory and Hertz contact model provides a good estimate of the elastic property of the model porous media in small strain limit.

The study also validates the accuracy and suitability of the hybrid LBM-FEM method in modeling fluid-structure interaction in complex geometries like porous media. It highlights the advantages of using this method to understand the behaviour of real porous geometries, as there is no need to calculate the bulk modulus, the permeability or the porosity of the geometry. Further, using the method, the study can be extended to the less investigated area of non-homogeneous and anisotropic deformable porous media.

An important contribution of this research work is the development of an analytical expression for predicting the bulk elastic modulus (E_b) of nonhomogeneous orthogonal arrangement of cylinders. The work of Deresiewicz [34] in the area of bulk modulus of simple cubic arrangement has been extended to orthogonal arrangements. Unlike in simple cubic arrangement of spheres, in the case of orthogonal arrangements of cylinders bulk elastic modulus expression consists of contributions from cylinder-to-cylinder contact and also from bending of cylinder between two points of contact. The expression is used to predict the layer-by-layer variation of bulk elastic modulus of different orthogonal arrangements of cylinders in which the cylinder diameter varies from top to bottom. It is found that the diameter of the cylinder does not have a significant impact on the bulk elastic modulus, rather the arrangement of the cylinders has a greater impact on the bulk modulus. This is because this arrangement determines the effect the bending type of deformation has on the total deformation of the structure.

Further an attempt has been made to represent complex fibrous porous media such as felt by a more simplified geometry consisting of regular arrangements of cylinders.

The goal here is to use a geometry that captures the geometrical complexity of the real media (felt) and can accurately represent its deformational characteristics while being easy to construct and needing less computational effort to predict the deformational behaviour. In order to develop a model geometry to represent the complex real porous media, the three parameters, porosity (n^F), permeability (k^F)and bulk modulus (E_b) have to be matched between the model and real porous media. It is found that the permeability and porosity relations in skewed orthogonal arrangement matches closely with the existing literature on real layered fibrous porous media even for very low solid volume fractions. This implies that given the porosity variation and the variation of the fiber diameter, a model fibrous porous media geometry can be constructed that would represent the real media in terms of its behaviour of permeability with porosity. In terms of matching the other remaining parameter i.e the bulk modulus, considerable progress has been made. As mentioned above, it is now possible to predict the bulk modulus of any orthogonal arrangement of cylinders. However due to lack of information on the bulk modulus of fibrous media, particularly information regarding the variation of the bulk modulus with the compression direction, it is difficult to predict if the skewed orthogonal arrangement would completely represent the real layered fibrous porous media.

Finally investigation have been carried out to understand the behaviour of permeability with deformation. The LBM-FEM method has been used to perform compression of model porous geometries and the resulting deformed geometry is used to carry out a flow simulations to determine permeability. Two geometries were used as test cases, the simple-cubic arrangement of spheres and the skewed orthogonal arrangement of cylinders. The permeability of the simple-cubic arrangement of spheres shows small change during the compression process. There is considerable difference in the variation of permeability from the direct simulation results and the popular Kozeny-Carmen relationship. We attribute the reason for this difference to the fact that the

numerical simulations carried out in this research mainly look at the behaviour of permeability due to the deformation of the solid structure. This is in contrast to the analytical model which approximates the porous media as a capillary tube bundle and relates the change in porosity to a change in the tube diameter. The analytical model would work well for problems that involve more movement in the geometry and less deformation such as soil. The permeability variation in skewed orthogonal arrangement shows a large decrease with deformation. It is seen that the variation in permeability matches the existing models of Davis [22] and Hapel [35]. Unlike the spheres in simple-cubic arrangement in the skewed orthogonal arrangement of cylinders it is seen that the there is considerable movement in the geometry apart from pure deformation, which contributes to the large variations in permeability during deformation. This study emphasizes the need to perform further investigations, which may lead to a better understanding of the effect of deformation on the pore structure and related properties of different types of porous media.

Since the method requires a finite element mesh as input, there is no limitation on the geometry that can be analyzed with this technique. Thus the investigations can be extended to other fluid-structure interaction problems involving small deformations. However, in order to avoid singularities and inaccuracies, the FE mesh should be well resolved. For geometries reconstructed through imaging techniques, generating well resolved finite element mesh is not a trivial task. Presently, this limitation prevents the application of LBM-FEM method to real geometries generated through x-ray microtomography.

7.2 Future Recommendations

The primary recommendation of this work is the need for experimental investigations into the deformational behaviour of model porous geometries that have been numerically investigated in this work. The aspects of effect of fiber diameter on

the deformational behaviour that have been investaged using the skewed orthogonal arrangement can easily be investigated using nonwoven fibers of same porosity but different fiber diameter. Experimental work can also give better understanding of the behaviour of bulk elastic modulus in such geometries.

Regarding recommendations in improving the existing numerical method, the contact model implemented to keep solid regions from overlapping is based on an exponentially varying repulsive force model. This model performs extremely well in the small deformation range as seen from the validation of the contact model and the comparison with de Boer et. al. model. Further the model requires the contact parameters to be calculated *a priori* based on the applied loading conditions. For large deformations that occur in very small period of time, the contact model can cause singularities due to the ill-resolution of the gap length. An improved contact model that scales with the applied load and also is stable during rapid changes in gap length is essential in extending the method to large deformations such as those during the compression of felt in wet-pressing process.

Further, the finite element implementation needs to be modified to include second order terms in the strain tensor and also use a large strain model such as the "Mooley-Rivlin" model, in order to model large deformations accurately.

Another recommendation is the implementation of a friction model in the solid phase to simulate the frictional dissipation during contact and sliding of solid surfaces. The existing numerical techniques based on homogenization including the Biots theory and the theory of porous media ignore the dissipation of energy due to friction in the solid phase. The implementation of this model in the LBM-FEM method can lead to significant insights into the effect of friction on the deformation of saturated porous media.

APPENDIX A

PERMEABILITY DEFINITIONS

In literature there are a number of definitions of permeability. In this section, some of the commonly used permeability definitions are related clarification are provided.

A.1 Conventional Permeability

Following the original work of Henry Darcy, mathematical descriptions of liquid flow in porous media are based on Darcys law. This states that the volumetric flow rate Q of liquid through a specimen of porous material is proportional to the hydrostatic pressure difference Δp across the specimen, in-versely proportional to the length L of the specimen, and proportional to the cross sectional area A. Darcys law is expressed simply as $Q = K^F A \Delta p / L$. We call the constant of proportionality defined by Darcys law the Darcy permeability of the material. The quantity Q A has dimensions LT 1 and is the flow rate, flux or Darcy velocity or seepage velocity w^F, so that Darcys law is more commonly written as

$$w^F = K^F \frac{\Delta p}{L}. \tag{126}$$

However it is common to express hydrostatic pressures in terms of the pressure potential $P = p/\rho g$, where ρ is the liquid density. P has dimension of L and is entirely equivalent to the hydrostatic head. We then express Darcys law as

$$w^F = K^F \nabla P. \tag{127}$$

Here K^F is called the conventional of Darcy's permeability coefficient and has dimensions of LT^{-1}. Note that K^F is dependent on both the geometry of the porous media and the properties of the fluid.

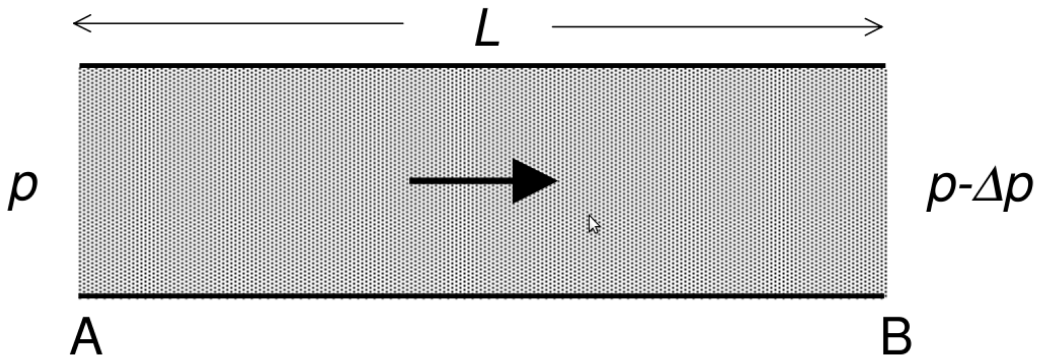

Figure 69: Darcian flow inside a saturated porous media.

A.2 Intrinsic permeability

For permeation flows which are geometrically similar (in practice, newtonian liquids in laminar flow in inert non-swelling media) the permeability K^F varies inversely as the fluid viscosity μ^F. Therefore we can define an intrinsic permeability $\kappa^F = K^F\mu$ such that $w^F = \frac{\kappa^F}{\mu^F}\nabla P$. κ^F is a material property independent of the fluid used to measure it. κ^F has dimensions of L^2.

APPENDIX B

BULK ELASTIC MODULUS / COMPRESSIBILITY MODULUS

Deresiewiee [34] provided an expression for the relationship between stress (σ_{zz}) and strain (ϵ_{zz}) for simple cubic arrangement of spheres when homothetic compressive load σ_o is applied. The expression is given as

$$\epsilon_{zz} = \frac{3R}{E^* a}\sigma_o \left[\left(1 + \frac{\sigma_{zz}}{\sigma_o}\right)^{2/3} + 1\right], \tag{128}$$

where R is the sphere radius, a is the contact radius specified by Hertz's model, E^* is given as $\frac{E}{1-\nu^2}$ (E,ν are Young's modulus and Poisson ratio).

For finite deformations from the quasi-static equilibrium position determined by the load σ_o, equation 128 and equation 64 are the same. Thus we can use the above equation near the equilibrium position to show that the ratio of E_b to E is small depending on the applied load σ_o.

Equation 128 can be expanded for small values of $\frac{\sigma_{zz}}{\sigma_o}$ which results in the following expression for relationship between stress-strain.

$$\epsilon_{ii} = \frac{2R}{E^* a}\sigma_{ii}. \tag{129}$$

This expression provides the same value of the instantaneous bulk modulus as given in equation 64.

REFERENCES

[1] Aidun, C. and Clausen, J., "Lattice-boltzmann method for complex flows," *Annual Review of Fluid Mechanics*, vol. 42, pp. 439–472, 2009.

[2] Aidun, C., Lu, Y., and Ding, E., "Direct analysis of particulate suspensions with inertia using the discrete boltzmann equation," *Journal of Fluid Mechanics*, vol. 373, pp. 287–311, 1998.

[3] Bernsdorf, J., Brenner, G., and Durst, F., "Numerical analysis of the pressure drop in porous media flow with lattice boltzmann (bgk) automata," *Computer Physics Communications*, vol. 129, pp. 247–255, 2000.

[4] Bernsdorf, J., Durst, F., and Schafer, M., "Comparison of celullar automata and finite volume techniques for simulation of incompressible flows in complex geometries," *International Journal of Numerical Methods and Fluids*, vol. 29, pp. 251–264, 1999.

[5] Bernsdorf, J., Zeiser, T., Brenner, G., and Durst, F., "Simulation of channel flow around a square obstacle with lattice boltzmann (bgk) automata," *International Journal of Modern Physics C*, vol. 9, no. 8, pp. 1129–1141, 1998.

[6] Beanovic, D., van Duijn, C. J., and Kaasschieter, E., "Analysis of paper pressing: the saturated one-dimensional case," *Journal of applied mathematics and mechanics*, vol. 86, no. 1, pp. 18–36, 2006.

[7] Beanovic, D., van Duijn, C. J., and Kaasschieter, E., "Analysis of wet pressing of paper: the three-phase model. part i: constant air density," *Transport in Porous Media*, vol. 67, pp. 93–113, 2007.

[8] Beanovic, D., van Duijn, C. J., and Kaasschieter, E., "Analysis of wet pressing of paper: the three-phase model. part ii: Compressible air case," *Transport in Porous Media*, vol. 67, pp. 171–187, 2007.

[9] Biot, M., "General theory of three dimensional consolidation," *Journal of Applied Physics*, vol. 12, pp. 155–164, 1941.

[10] Biot, M., "Theory of deformation of a porous viscoelastic anisotropic solid," *Journal of Applied Physics*, vol. 26, no. 2, pp. 182–185, 1956.

[11] Biot, M., "Thoery of propagation of elastic waves in a fluid-saturated porous solid. i. higher-frequency range," *The Journal of the Acoustic Society of America*, vol. 28, no. 2, pp. 179–191, 1956.

[12] Biot, M., "Thoery of propagation of elastic waves in a fluid-saturated porous solid. i. low-frequency range," *The Journal of the Acoustic Society of America*, vol. 28, no. 2, pp. 168–178, 1956.

[13] Bird, R., Stewart, W., and Lightfoot, E., *Transport Phenomena*. John Wiley and Sons, Inc., 2002. 2nd Edition.

[14] Bluhm, J., "A consistent model for saturated and empty porous media," *Forschungsber. Fachber. Bauwesen*, vol. 74, 1997.

[15] Boer, R. D., "Highlights in the historical development of porous media theory: toward a consistent macroscopic theory," *Applied Mechanics Review*, vol. 49, pp. 201–262, 1996.

[16] Boer, R. D., "Theory of porous media past and present," *Zeitschrift fr angewandte mathematik und mechanik*, vol. 78, no. 7, pp. 441–466, 1998.

[17] Breuer, M., Bernsdorf, J., Zeiser, T., and Durst, F., "Accurate computations of the laminar flow past a square cylinder based on two different methods: lattice-boltzmann and finite-volume," *International Journal of Heat and Fluid Flow*, vol. 21, pp. 186–196, 2000.

[18] Brundrett, E., "Prediction of pressure drop for incompressible flow through screens," *Journal of Fluids Engineering*, vol. 115, no. 1, p. 239, 1993.

[19] Buxton, G., Verberg, R., Jasnow, D., and Balas, A. C., "Newtonian fluid meets an elastic solid: coupling lattice boltzmann and lattice-spring models," *Physical Review E*, vol. 71, p. 56707, 2005.

[20] Cancelliere, A., Chang, C., Foti, E., Rothman, D., and Succi, S., "The permeability of a random medium - comparison of simulation with theory," *Physics of Fluids A - Fluid Dynamics*, vol. 2, no. 12, pp. 2085–2088, 1990.

[21] Clausen, J., Reasor, D., and Aidun, C., "Parallel performance of a lattice-boltzmann/finite element cellular blood flow solver on the ibm bleu gene/p architecture," *Computer Physics Communications*, 2009.

[22] Davis, C., *Air Filteration*. Academic, London, 1973.

[23] de Boer, R. and Bluhm, J., "The influence of compressibility on the stresses of elastic porous solids-semimicroscopic investigations," *International Journal of Solid and Structures*, vol. 36, pp. 4805–4819, 1999.

[24] de Boer, R. and Ehlers, W., "Uplift,friction and capillarity - three fundemental effects for liquid-saturated porous solids," *Internation Journal of Solids and Structures*, vol. 26, no. 1, pp. 43–57, 1990.

[25] de Boer, R., Ehlers, W., and Liu, Z., "One-dimensional transient wave propagation in fluid-saturated incompressible porous media," *Archive of Applied Mechanics*, vol. 63, pp. 59–72, 1993.

[26] Diabels, S. and Ehlers, W., "Dynamic analysis of fully saturated porous medium accounting for material and geometrical nonlinearities," *INTERNATIONAL JOURNAL FOR NUMERICAL METHODS IN ENGINEERING*, vol. 39, pp. 81–97, 1996.

[27] Ding, E. and Aidun, C., "Extension of the lattice-boltzmann method for direct simulation of suspended particles near contact," *Journal of Statistical Physics*, vol. 112, no. 3, pp. 685–708, 2003.

[28] Durst, F., Hass, R., and Interthal, W., "The nature of flows through porous media," *Journal of Non-Newtonian Fluid Mechanics*, vol. 22, pp. 169–189, 1987.

[29] E., D., E., T., and H., R., "On the accuracy of the hertz model to describe the normal contact of soft elastic spheres," *Granular Matter*, vol. 10, pp. 209–221, 2008.

[30] Ehlers, W., "On thermodynamics of elasto-plastic media," *Archives of Mechanics*, vol. 41, no. 1, pp. 73–93, 1989.

[31] Ehlers, W. and Eipper, G., "Finite elastic deformations in liquid-saturated and empty porous solids," *Transport in Porous Media*, vol. 34, pp. 179–191, 1999.

[32] Ehlers, W. and Markert, B., "On the viscoelastic behavior of fluid saturated porous material," *Granular Matter*, vol. 2, pp. 153–161, 2003.

[33] Ehlers, W. and Volk, W., "On theoritical and numerical methods in the theory of porous media based on polar and non-polar elasto-plastic solid materials," *International Journal of Solid and Structures*, vol. 35, pp. 4597–4617, 1998.

[34] H., D., "Stressstrain relations for a simple model of granular medium," *Journal of Applied Mechanics*, vol. 25, pp. 402–406, 1958.

[35] Hapel, J., "Viscous flow relative to arrays of cylinders," *AIChE Journal*, vol. 5, pp. 174–177, 1959.

[36] Higdon, J. and Ford, G., "Permeability of three-dimensional models of fibrous porous media," *Journal of Fluid Mechanics*, vol. 308, pp. 341–361, 1996.

[37] Hu, Y., Zhu, Y., and Cheng, C., "Dqm for dynamic response of fluid-saturated visco-elastic porous media," *Internation Journal of Solids and Structures*, vol. 46, pp. 1667–1675, 2009.

[38] Huyghes, J., Janssen, C., and Lanir, Y., *Experimental measurement of electrical conductivity and electro-osmotic permeability of ionised porous media*. Springer, 2002. Porous Media Theory Experiments and Numerical Applications. W. Ehlers and J Bluhm, editors.

[39] Jackson, G. and James, D., "The permeability of fibrous porous media," *The Canadian Journal of Chemical Engineering*, vol. 64, p. 364, 1986.

[40] Jaganathan, S., Tafreshi, H. V., and Pourdeyhimi, B., "A realistic approach for modeling permeability of fibrous media: 3-d imaging coupled with cfd simulation," *Chemical Engineering Science*, vol. 63, pp. 244–252, 2008.

[41] Jaganathan, S., Tafreshi, H. V., Shim, E., and Pourdeyhimi, B., "A study on compression-induced morphological changes of nonwoven fibrous materials," *Colloids and Surfaces A: Physicochem. Eng. Aspects*, vol. 337, pp. 173–179, 2009.

[42] Karypis, G. and Kumar, V., "Multilevel k-way partitioning scheme for irregular graphs," *Journal of parallel and distributed computing.*, vol. 48, p. 10, 1998.

[43] Kataja, M., Hiltunen, K., and Timonen, J., "Flow of water and air in a compressible porous medium:a model of wet pressing of paper.," *J. Phys. D: Appl. Phys*, vol. 25, pp. 1053–1063, 1992.

[44] Kerekes, R. and McDonald, J., "A decreasing permeability model of wet pressing: Application," *TAPPI Journal*, pp. 142–149, 1991.

[45] Kerekes, R. and McDonald, J., "A decreasing permeability model of wet pressing: Theory," *TAPPI Journal*, pp. 150–156, 1991.

[46] Kerekes, R. and McDonald, J., "A decreasing permeability model of wet pressing with rewetting," *TAPPI Journal*, vol. 78, no. 11, pp. 107–111, 1991.

[47] Khan, I. and Aidun, C., "Direct numerical simulation of saturated deformable porous media using a parallel hybrid lattice-boltzmann finite element method," *International Journal of Numerical Methods in Engineering*, vol. in review, 2010.

[48] Koivu, V., Mattila, K., and Kataja, M., "A method for measuring darcian flow permeability of thin compressed fibre mats," *Nordic Pulp and Paper Research Journal*, vol. 24, no. 4, pp. 395–402, 2009.

[49] Koponen, A., Kandhai, D., Hellen, E., Alava, M., Hoekstra, A., Kataja, M., Niskanen, K., Sloot, P., and Timonen, J., "Permeability of three-dimensional random fiber webs," *Physical Review Letters*, vol. 80, no. 4, pp. 716–719, 1998.

[50] Kwon, H.-D., "Efficient parallel implementations of finite element methods based on the conjugate gradient method," *Applied Mathematics and Computation*, vol. 145, pp. 869–880, 2003.

[51] Ladd, A., "Numerical simulations of particulate suspensions via a discretized boltzmann equation. part 1. theoritical foundation," *Journal of Fluid Mechanics*, vol. 271, pp. 285–309, 1994.

[52] Li, Y. and Park, C., "A predictive model for the removal of colloidal particles in fibrous filter media.," *Chemical Engineering Sciences*, vol. 54, pp. 633–644, 1999.

[53] Lindsay, J. and Brady, P., "Studies of anisotropic permeability with applications to water removal in fibrous webs, part1. experimental methods, sheet anisotropy and relationship to freeness," *TAPPI Journal*, vol. 76, no. 9, pp. 119–127, 1993.

[54] Lindsay, J. and Brady, P., "Studies of anisotropic permeability with applications to water removal in fibrous webs, part1. relationship between water removal and permeability and additional factors affecting permeability," *TAPPI Journal*, vol. 76, no. 11, pp. 167–174, 1993.

[55] Liu, C.-H., Leung, D. Y. C., and Woo, C.-M., "Development of a scalable finite element solution to the navierstokes equations," *Computational Mechanics*, vol. 32, pp. 185–198, 2003.

[56] MacMeccan, R., Clausen, J., Neitzel, G., and Aidun, C., "Simulating deformable particle suspensions using a coupled lattice-boltzmann and finite-element method," *Journal of Fluid Mechanics*, vol. 618, pp. 13–39, 2009.

[57] Maze, B., Tafreshi, H., Wang, Q., and Pourdeyhimi, B., "Unsteady state simulation of nanoparticle aerosol filteration via nanofiber electrospun filters at reduced pressures," *Journal of Aerosol Science*, vol. 38, pp. 550–571, 2007.

[58] Miyamura, A., Iwasaki, S., and Ishii, T., "Experimental wall correction factors of single solid spheres in triangular and square cylinders, and parallel plates," *Internationl Journal of Multiphase Flow*, vol. 7, pp. 41–46, 1981.

[59] Moller, T. and Trombore, B., "Fast, minimum storage ray-traingle intersection," *Journal of Graphics Tools*, vol. 2, pp. 21–28, 1997.

[60] Nilsson, P. and Larsson, K., "Paper web performance in a press nip," *Pulp Paper Mag. Canada*, vol. 69, pp. 66–73, 1964.

[61] Noble, D., Georgiadis, G., and Buckius, R., "Comparison of accuracy and performance for lattice boltzmann and finite difference simulations of steady viscous flow," *Internation Journal of Numerical Methods in Fluids*, vol. 23, pp. 1–18, 1996.

[62] Patankar, S., "Numerical heat transfer and fluid flow," 1980.

[63] Roux, J. and Vincent, J., "A proposed model in the analysis of wet pressing," *TAPPI Journal.*, pp. 189–196, 1991.

[64] S, B., Gropp, W. D., McInnes, L. C., and Smith, B. F., *Efficient management of parallelism in object oriented numerical software libraries.* Birkhauser Press, 1997. In Modern Software Tools in Scientific Computing E. Arge, A. M. Bruaset, and H. P. Langtangen, editors.

[65] Saad, Y., *Iterative Methods for Sparse Linear Systems*. SIAM, 2003. 2nd Edition.

[66] Sobera, M. P. and Kleijn, C. R., "Hydraulic permeability of ordered and disordered single-layer arrays of cylinders," *Physical Review E*, vol. 74, no. 036301, 2006.

[67] Spielman, L. and Goren, S., "Model for predicting pressure drop and filtration efficiency in fibrous media," *Environmental Science and Technology*, vol. 2, pp. 279–287, 1968.

[68] Sui, Y., Chew, Y., Roy, P., and Low, H., "A hybrid method to study flow-induced deformation of three-dimensional capsules," *Journal of Computational Physics*, vol. 227, pp. 6351–6371, 2008.

[69] Tahir, M. A. and Tafreshi, H. V., "Influence of fiber orientation on the transverse permeability of fibrous media," *Physics of Fluids*, vol. 21, no. 083604, 2009.

[70] Timoshenko, S. and Goodier, J., *Theory of Elasticty*. McGraw-Hill Book Co., 1970. 3rd Edition.

[71] Tomadakis, M. and Robertson, J., "Viscous permeability of random fiber structures: Comparison of electrical and diffusional estimates with experimental and analytical results," *Journal of Composite Materials*, vol. 39, pp. 163–188, 2005.

[72] Vomhoff, H., Martinez, D., and Norman, B., "The transverse steady-state permeability of a fibre web compressed between rough permeable surfaces," *Journal of Pulp and Paper Science*, vol. 26, pp. 428–436, 2000.

[73] Wahlstrom, P., "A long term study of water removal and moisture distribution on a newsprint machine press section," *Pulp Paper Magazine Canada*, vol. 61, pp. T379–401, 1960.

[74] Wang, C., "Inhomogeneities in second-grade fluid bodies and isotropic solid bodies," *Arch. Mech.*, vol. 25, p. 765, 1073.

[75] Wang, Q., Maze, B., Tafreshi, H., and Pourdeyhimi, B., "A case study of simulating submicron aerosol filtration via lightweight spun-bondedfilter media," *Chemical Engineering Science*, vol. 61, pp. 4871–4883, 2006.

[76] Wyke, C. V., "Note on the compressibility of wool," *Journal of the Textile Institute*, vol. 37, pp. T285–T292, 1946.

[77] Zobel, S., Maze, B., Tafreshi, H. V., Wang, Q., and Pourdeyhimi, B., "Simulating permeability of 3-d calendered fibrous structures," *Chemical Engineering Science*, vol. 62, pp. 6285–6296, 2007.